Chapter 10

EXERGY ANALYSIS OF RENEWABLE ENERGY SYSTEMS

Exergy analyses are performed in this chapter of several renewable energy systems including solar photovoltaic systems, solar ponds, wind turbines and geothermal district heating systems and power plants. These and other renewable energy systems are likely to play increasingly important roles in societies in the future.

10.1. Exergy analysis of solar photovoltaic systems

Solar photovoltaic (PV) technology converts sunlight directly into electrical energy. Direct current electricity is produced, which can be used in that form, converted to alternating current or stored for later use. Solar PV systems operate in an environmentally benign manner, have no moving components, and have no parts that wear out if the device is correctly protected from the environment. By operating on sunlight, PV devices are usable and acceptable to almost all inhabitants of our planet. PV systems can be sized over a wide range, so their electrical power output can be engineered for virtually any application, from low-power consumer uses like wristwatches, calculators and battery chargers to significantly energy-intensive applications such as generating power at central electric utility stations. PV systems are modular, so various incremental power capacity additions are easily accommodated, unlike for fossil or nuclear fuel plants, which require multi-megawatt plants to be economically feasible.

The solar PV cell is one of the most significant and rapidly developing renewable-energy technologies, and its potential future uses are notable. By using solar radiation, a clean energy source, PV systems are relatively benign environmentally. During the last decade, PV applications have increased in many countries and are observed throughout the residential, commercial, institutional and industrial sectors. The clean, renewable and in some instances economic features of PV systems have attracted attention from political and business decision makers and individuals. Advances in PV technology have also driven the trend to increased usage.

A PV cell is a type of photochemical energy conversion device. Others include photoelectric devices and biological photosynthesis. Such systems operate by collecting a fraction of the radiation within some range of wavelengths. In PV devices, photon energies greater than the cutoff (or band-gap) energy are dissipated as heat, while photons with wavelengths longer than the cutoff wavelength are not used.

The energy conversion factor of a solar PV system sometimes is described as the efficiency, but this usage can lead to difficulties. The efficiency of a solar PV cell can be considered as the ratio of the electricity generated to the total, or global, solar irradiation. In this definition only the electricity generated by a solar PV cell is considered. Other properties of PV systems, which may affect efficiency, such as ambient temperature, cell temperature and chemical components of the solar cell, are not directly taken into account.

The higher performance, lower cost and better reliability demonstrated by today's PV systems are leading many potential users to consider the value of these systems for particular applications. Together, these applications will likely lead industry to build larger and more cost-effective production facilities, leading to lower PV costs. Public demand for environmentally benign sources of electricity will almost certainly hasten adoption of PV. The rate of adoption will be greatly affected by the economic viability of PV with respect to competing options. Many analysts and researchers believe that it is no longer a question of if, but when and in what quantity, PV systems will gain adoption. Since direct solar radiation is intermittent at most locations, fossil fuel-based electricity generation often must supplement PV systems. Many studies have addressed this need.

This section describes solar PV systems and their components and discusses the use of exergy analysis to assess and improve solar PV systems. Exergy methods provide a physical basis for understanding, refining and predicting the

variations in solar PV behavior. This section also provides and compares energy- and exergy-based solar PV efficiency definitions.

10.1.1. PV performance and efficiencies

Three PV system efficiencies can be considered: power conversion efficiency, energy efficiency and exergy efficiency. Energy (η) and exergy (ψ) efficiencies for PV systems can be evaluated based on the following definitions:

$$\eta = \text{energy in products/total energy input}$$

$$\psi = \text{exergy in products/total exergy input}$$

For solar PV cells, efficiency measures the ability to convert radiative energy to electrical energy. The electrical power output is the product of the output voltage and the current out of the PV device, taken from the current–voltage curve (I–V curve). This conversion efficiency is not a constant, even under constant solar irradiation. However, there is a maximum power output point, where the voltage value is V_m, which is slightly less than the open-circuit voltage V_{oc}, and the current value is I_m, which is slightly less than the short-circuit current I_{sc} (Fig. 10.1). In this figure, E_{GH} represents the highest energy level of the electron attainable at maximum solar irradiation conditions. It is recognized that there should be an active relational curve from I_{sc} to V_{oc} and, with this relation, E_{GH} becomes equivalent to $\int_{V=0}^{V_{oc}} I(V)\mathrm{d}V$. In addition E_L represents the low-energy content of the electron, which is the more practical energy; this energy is shown as the rectangular area in Fig. 10.1, so $E_L = I_m V_m$. The maximum power point is restricted by a 'fill factor' FF, which is the maximum power conversion efficiency of the PV device and is expressible as

$$FF = \frac{V_m I_m}{V_{oc} I_{sc}} \tag{10.1}$$

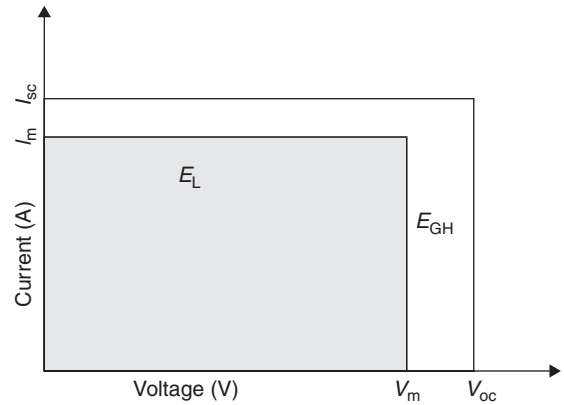

Fig. 10.1. Illustration of a general current–voltage (I–V) curve.

10.1.2. Physical exergy

The enthalpy of a PV cell with respect to the reference environment, ΔH, can be expressed as

$$\Delta H = C_p(T_{cell} - T_{amb}) \tag{10.2}$$

where C_p denotes the heat capacity, T_{amb} the ambient temperature and T_{cell} the cell temperature. The total entropy of the system relative to ambient conditions, ΔS, can be written as

$$\Delta S = \Delta S_{system} + \Delta S_{surround} \tag{10.3}$$

or

$$\Delta S = C_p \ln\left(\frac{T_{cell}}{T_{amb}}\right) - \frac{Q_{loss}}{T_{cell}} \tag{10.4}$$

where

$$Q_{loss} = C_p(T_{cell} - T_{amb}) \tag{10.5}$$

Here, Q_{loss} represents heat losses from the PV cell. With Eqs. (10.2) through (10.5), the physical exergy output for a PV cell system can be expressed as

$$Ex = E_{GH} + C_p(T_{cell} - T_{amb}) + T_{amb}\left(C_p \ln\frac{T_{cell}}{T_{amb}} - \frac{Q_{loss}}{T_{cell}}\right) \tag{10.6}$$

The first term on the right side of this equation (E_{GH}) is the generated electricity at the highest energy content of the electron. The second and third terms are the enthalpy and entropy contributions, respectively.

10.1.3. Chemical exergy

The process of PV energy conversion (Fig. 10.2) can in general be divided into two steps:

1. Electronic excitation of the absorbing component of the converter by light absorption with concomitant electronic charge creation.
2. Separation of the electronic charges.

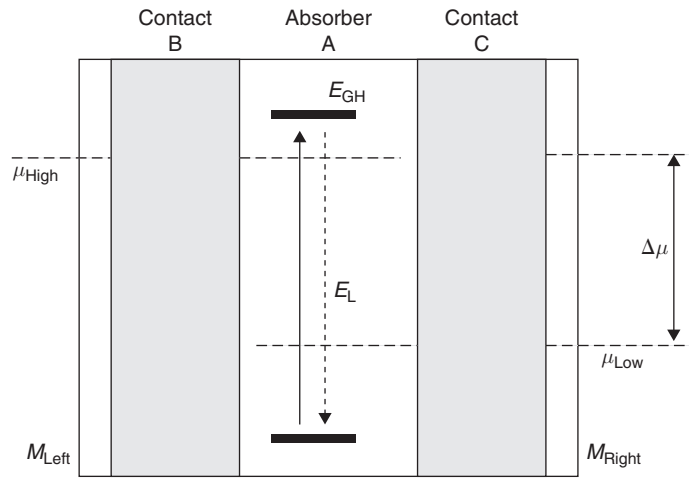

Fig. 10.2. An idealized photovoltaic converter (adapted from Bisquert et al. (2004)).

The excitation can be an electron–hole pair in a semiconductor, an electronic excitation of a molecule, or the production of excitations. In terms of the two level systems shown in Fig. 10.2, electronic excitation in the absorber promotes the system into the highest energy content with the associated electronic energy level H, simultaneously creating an electron-deficient low-energy content with associated energy level L. The electrons in these two states are separated. The departure of the populations of the states from their thermal equilibrium values implies a difference in their chemical potentials (partial-free energies) (Bisquert et al., 2004), as can be seen in Fig. 10.2. That is,

$$\Delta\mu = \mu_H - \mu_L \tag{10.7}$$

From the point of view of thermodynamics, the separation of Fermi levels arises as a result of the absorber being at a lower ambient temperature T_{amb} than the radiation 'pump' temperature T_p (i.e., the temperature of the sun). A Carnot cycle

argument or statistical analysis gives the following upper limit chemical potential for the open-circuit voltage (Landsberg and Markvart, 1998; Bisquert et al., 2004):

$$\Delta\mu = \left(1 - \frac{T_{\text{cell}}}{T_{\text{p}}}\right)(E_{\text{GH}} - E_{\text{L}}) \tag{10.8}$$

where E_{GH} is the generated electricity at the highest-energy content of the electron and E_{L} is the available energy content of the electron (as the practical case).

Note that there is no current flow at the open-circuit voltage and that there is no voltage difference at the short-circuit current. Maximum power can be predicted to occur between these limits (Fig. 10.2). The power relations between voltage and electron charge are

$$E = qV \tag{10.9}$$

and

$$I = \frac{q}{t} \tag{10.10}$$

where V denotes circuit voltage, q electron charge, I circuit current and t time duration. The open-circuit voltage V_{oc} and short-circuit current I_{sc} represent the energy level without voltage or current, respectively.

To simplify the analysis, we take the curve for E_{GH} in Fig. 10.1 to be rectangular. Based on the Carnot cycle analogy, Eq. (10.8) then becomes

$$\Delta\mu = \left(1 - \frac{T_{\text{cell}}}{T_{\text{p}}}\right)[V_{\text{oc}}I_{\text{sc}} - V_{\text{m}}I_{\text{m}}] \tag{10.11}$$

This expression is used to determine the chemical exergy, following the approach presented in Fig. 10.1. As noted earlier, the efficiencies cannot be evaluated easily for some components at open-circuit voltage and short-circuit current, which are the conditions at which maximum power can be generated in a PV cell system. But from a thermodynamic perspective, the unconsidered remaining components should be extracted from the overall I–V curve. As a result, the total exergy of the PV solar cell can be formulated as

$$Ex = Ex_{\text{physical}} - (q_{\text{sc}}V_{\text{oc}} - q_{\text{L}}V_{\text{L}})\frac{T_{\text{cell}}}{T_{\text{p}}} \tag{10.12}$$

where Ex_{physical}, q_{L} and V_{L} represent respectively the physical exergy shown in Eq. (10.6) with the excited electron charge at the low-energy content, the electron charge and the voltage.

We now define the solar cell power conversion efficiency η_{pce} as a function of E_{L} and S_{T} as follows:

$$\eta_{\text{pce}} = \frac{E_{\text{L}}}{S_{\text{T}}} = \frac{V_{\text{m}}I_{\text{m}}}{S_{\text{T}}} \tag{10.13}$$

where S_{T} represents hourly measured total solar irradiation.

The solar power conversion efficiency can also be defined in terms of the fill factor FF, based on Eq. (10.1), as follows:

$$\eta_{\text{pce}} = \frac{FF \times V_{\text{oc}}I_{\text{sc}}}{S_{\text{T}}} \tag{10.14}$$

The second main energy source is the solar irradiance incident on PV cells. Evaluation of the exergy efficiency of PV cells requires, therefore, the exergy of the total solar irradiation. PV cells are affected by direct and indirect components of solar irradiation, the magnitude of which depend on atmospheric effects. The exergy of solar irradiance, Ex_{solar}, can be evaluated approximately as (Bejan, 1998; Santarelli and Macagno, 2004):

$$Ex_{\text{solar}} = S_{\text{T}}\left(1 - \frac{T_{\text{amb}}}{T_{\text{sun}}}\right) \tag{10.15}$$

As a result of these formulations, the exergy efficiency ψ can be expressed as

$$\psi = \frac{Ex}{Ex_{\text{solar}}} \tag{10.16}$$

After substituting Eqs. (10.12) and (10.15) into Eq. (10.16) we obtain the following expression for exergy efficiency:

$$\psi = \frac{Ex_{\text{physical}} - (q_{\text{sc}} V_{\text{oc}} - q_{\text{L}} V_{\text{L}}) \dfrac{T_{\text{cell}}}{T_{\text{p}}}}{S_{\text{T}} \left(1 - \dfrac{T_{\text{amb}}}{T_{\text{sun}}}\right)} \tag{10.17}$$

The energy efficiency η depends on the generated electricity of the PV cells E_{gen} and the total energy input based on the total solar irradiation S_{T}. That is,

$$\eta = \frac{E_{\text{GH}}}{S_{\text{T}}} \tag{10.18}$$

The exergy efficiency usually gives a finer understanding of performance than the energy efficiency, and stresses that both external losses and internal irreversibilities need to be addressed to improve efficiency. In many cases, internal irreversibilities are more significant and more difficult to address than external losses.

One reason why today's commercial solar PV cells are costly is that they are inefficient. The main losses in a PV cell during electricity generation are attributable to such factors as thermalization, junction contact and recombination. These internal losses are considered in the chemical exergy part of the section. By considering the balance of energy and the heat flux absorbed and emitted by the PV cell, one can evaluate the losses due to irreversible operation of the converter. For the present analysis of PV systems, thermal exergy losses are the main external exergy losses.

10.1.4. Illustrative example

The exergy efficiency of a PV cell is evaluated based on data from a short-term test on a rack-mounted PV cell in Golden, Colorado, which is located at 105.23°W longitude and 39.71°N latitude. The test was performed from 11:00 a.m. to 5:00 p.m. on June 28, 2001 and the data measured include total solar irradiation, maximum generated power by the system, voltage, open-circuit voltage, current, short-circuit current, cell temperature and ambient temperature. The system includes two modules in series per string, and the total array nominal power rating for six strings is 631.5W (Barker and Norton, 2003).

It can be seen that I–V curve parameters vary significantly with module temperature (Fig. 10.3). This is especially true for the current parameters I_{sc} and I_{m}, which exhibit strong linear variations with module temperature. The maximum power voltage V_{m} exhibits an inverse linear relation with module temperature. In addition, a second-degree polynomial relation is observed between open-circuit voltage and module temperature. This variation is not too significant. The curves in Fig. 10.3 can be used for parameter estimation.

Efficiencies are presented in Fig. 10.4, where it is seen that energy efficiencies of the system vary between 7% and 12%, while the exergy efficiencies of the system, which account for all inputs, irreversibilities and thermal emissions, vary from 2% to 8%. Power conversion efficiencies for this system, which depend on fill factors, are observed to be higher than the values for energy and exergy efficiencies.

Values of 'fill factors' are determined for the system and observed to be similar to values of exergy efficiency.

10.1.5. Closure

PV cells allow use of solar energy by converting sunlight directly to electricity with high efficiency. PV systems can provide nearly permanent power at low operating and maintenance costs in an environmentally benign manner. The assessment of PV cells described here illustrates the differences between PV cell energy and exergy efficiencies. Exergy analysis should be used for PV cell evaluation and improvement to allow for more realistic planning.

10.2. Exergy analysis of solar ponds

Solar radiation is abundantly available on all parts of the earth and in many regards is one of the best alternatives to non-renewable energy sources. One way to collect and store solar energy is through the use of solar ponds which

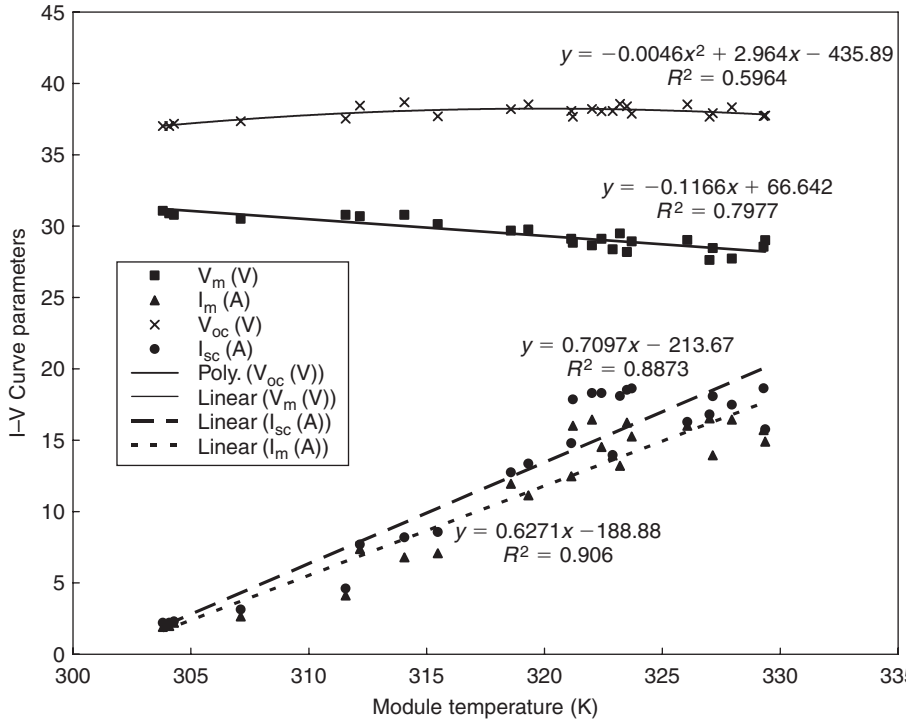

Fig. 10.3. Variation of several current–voltage (I–V) curve parameters with module temperature. Shown are data points as well as best fit curves (along with the R^2 values from the curve fitting routine).

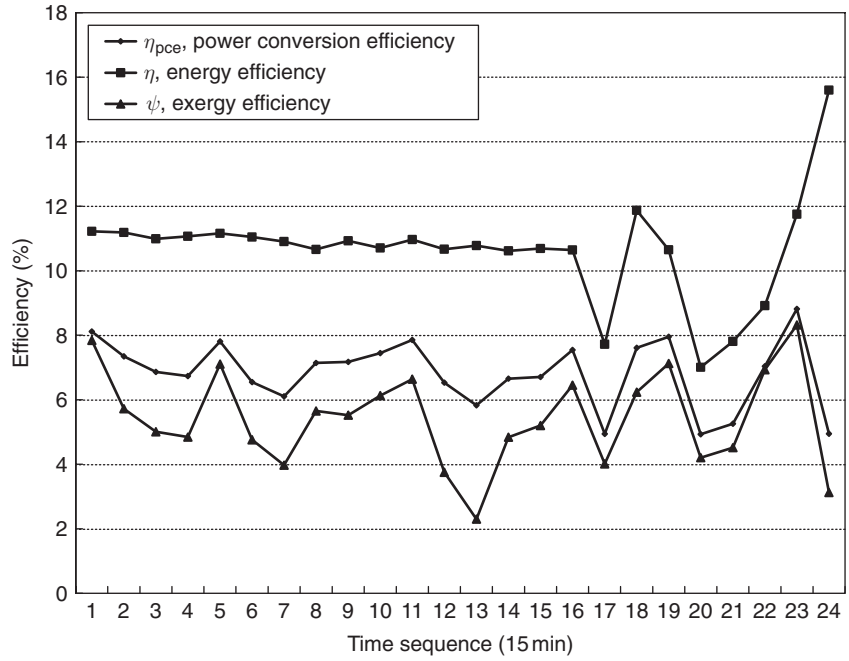

Fig. 10.4. Variation with time of energy and exergy efficiencies and power conversion efficiency.

can be used to supply thermal energy for various applications, such as process and space heating, water desalination, refrigeration, drying and power generation. Thermal energy storage has always been an important technique for energy storage. Solar ponds appear in some applications to have significant potential. The performance of a solar pond depends on its thermal energy storage capacity and its construction and maintenance costs (Dincer and Rosen, 2002; Jaefarzadeh, 2004). Performance also depends on thermophysical properties of the pond and storage fluid, and the surroundings conditions (Karakilcik, et al., 2006a, b). Solar ponds have recently received increasing attention in some applications. Numerous experimental and theoretical studies have been undertaken.

This section has two main parts. First, overall temperature distributions in a solar pond situated at Cukurova University in Adana, Turkey (35°18′ E longitude, 36° 59′ N latitude) are measured to determine heat losses, and energy efficiencies of the zones according to the rate of incident solar radiation, absorption and transmission of the zone are examined. The data allow pond performance to be obtained experimentally for three representative months (January, May and August). Significant factors affecting performance, such as wall shading, incident solar radiation, insulation and the thicknesses of zones, are also investigated. Second, an exergy analysis of solar ponds is performed in this section and contrasted with the energy analysis. Little experimental and theoretical research has been reported on the exergetic performance of solar ponds so this section builds primarily on recent research by the authors.

10.2.1. Solar ponds

A salinity gradient solar pond is an integral device for collecting and storing solar energy. By virtue of having built-in TES, it can be used irrespective of time and season. In an ordinary pond or lake, when the sun's rays heat the water this heated water, being lighter, rises to the surface and loses its heat to the atmosphere. The net result is that the pond water remains at nearly atmospheric temperature. Solar pond technology inhibits this phenomenon by dissolving salt into the bottom layer of this pond, making it too heavy to rise to the surface, even when hot. The salt concentration increases with depth, thereby forming a salinity gradient. The sunlight which reaches the bottom of the pond is trapped there. The useful thermal energy is then withdrawn from the solar pond in the form of hot brine. The prerequisites for establishing solar ponds are: a large tract of land (it could be barren), abundant sunshine and inexpensively available salt (e.g. NaCl) or bittern.

Salt-gradient solar ponds may be economically attractive in climates with little snow and in areas where land is readily available. In addition, sensible cooling storage can be added to existing facilities by creating a small pond or lake on site. In some installations this can be done as part of property landscaping. Cooling takes place by surface evaporation and the rate of cooling can be increased with a water spray or fountain. Ponds can be used as an outside TES system or as a means of rejecting surplus heat from refrigeration or process equipment.

Being large, deep bodies of water, solar ponds are usually sized to provide community heating. Solar ponds differ in several ways from natural ponds. Solar ponds are filled with clear water to ensure maximum penetration of sunlight. The bottom is darkened to absorb more solar radiation. Salt is added to make the water more dense at the bottom and to inhibit natural convection. The cooler water on top acts as insulation and prevents evaporation. Salt water can be heated to high temperatures, even above the boiling point of fresh water.

Figure 10.5 shows a cross section of a typical salinity gradient solar pond which has three regions. The top region is called the surface zone, or upper convective zone (UCZ). The middle region is called the gradient zone, or non-convective zone (NCZ), or insulation zone (IZ). The lower region is called the heat storage zone (HSZ) or lower convective

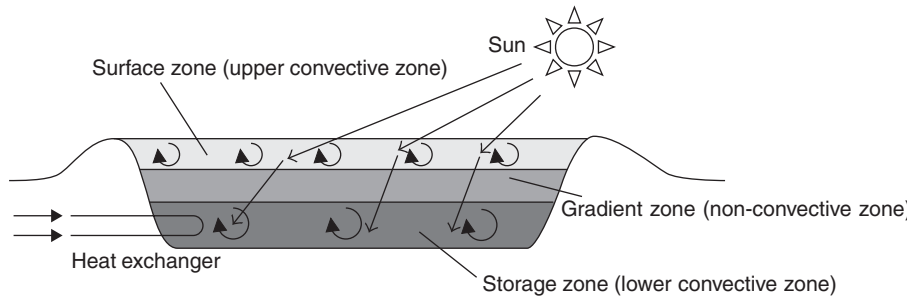

Fig. 10.5. Cross-section of a typical salinity-gradient solar pond.

zone (LCZ). The lower zone is a homogeneous, concentrated salt solution that can be either convecting or temperature stratified. Above it the non-convective gradient zone constitutes a thermally insulating layer that contains a salinity gradient. This means that the water closer to the surface is always less concentrated than the water below it. The surface zone is a homogeneous layer of low-salinity brine or fresh water. If the salinity gradient is large enough, there is no convection in the gradient zone even when heat is absorbed in the lower zone, because the hotter, saltier water at the bottom of the gradient remains denser than the colder, less salty water above it. Because water is transparent to visible light but opaque to infrared radiation, the energy in the form of sunlight that reaches the lower zone and is absorbed there can escape only via conduction. The thermal conductivity of water is moderately low and, if the gradient zone has substantial thickness, heat escapes upward from the lower zone slowly. This makes the solar pond both a thermal collector and a long-term storage device.

Further details on the three zones of solar ponds follow:

1. The UCZ is the fresh water layer at the top of the pond. This zone is fed with fresh water of a density near to the density of fresh water in the upper part to maintain the cleanliness of the pond and replenish lost water due to evaporation.
2. The NCZ or IZ lies between the LCZ and the UCZ. This zone is composed of salty water layers whose brine density gradually increases toward the LCZ. The NCZ is the key to the working of a solar pond. It allows an extensive amount of solar radiation to penetrate into the storage zone while inhibiting the propagation of long-wave solar radiation from escaping because water is opaque to infrared radiation.
3. The LCZ or HSZ is composed of salty water with the highest density. A considerable part of the solar energy is absorbed and stored in this region. The LCZ has the highest temperature, so the strongest thermal interactions occur between this zone and the adjacent insulated bottom-wall (IBW) and insulated side-walls (ISW).

Solar ponds were pioneered in Israel in the early 1960s, and are simple in principle and operation. They are long-lived and require little maintenance. Heat collection and storage are accomplished in the same unit, as in passive solar structures, and the pumps and piping used to maintain the salt gradient are relatively simple. The ponds need cleaning, like a swimming pool, to keep the water transparent to light. A major advantage of solar ponds is the independence of the system. No backup is needed because the pond's high heat capacity and enormous thermal mass can usually buffer a drop in solar supply that would force a single-dwelling unit to resort to backup heat.

10.2.2. Experimental data for a solar pond

For illustration, an experimental solar pond is considered with surface area dimensions of 2 m by 2 m and a depth of 1.5 m, as shown in Fig. 10.6. The solar pond was built at Cukurova University in Adana, Turkey. The salt-water solution is prepared by dissolving the NaCl reagent into fresh water. The thicknesses of the UCZ, NCZ and HSZ are 0.1 m, 0.6 m and 0.8 m, respectively. The range of salt gradient in the inner zones is such that the density is 1000–1045 kg/m^3 in the UCZ, and 1045–1170 kg/m^3 in the NCZ, 1170–1200 kg/m^3 in HSZ. Temperature variations are measured at the inner and outer zones of the pond. The bottom and the side-walls of the pond are plated with iron-sheets of 5 mm thickness, and contain glass wool of 50 mm thickness as an insulating layer. The solar pond is situated on a steel base 0.5 m above the ground and insulated with 20 mm thick wood slats positioned on the steel base. The inner and outer sides of the pond are covered with anti-corrosion paint. Figure 10.7 illustrates the inner zones of the solar pond.

Figure 10.8 illustrates solar radiation entering the pond, and the shading area by the south side-wall in the inner zones of the solar pond and the measurement points. The inner zones consist of 30 saline water layers of various densities. Each layer thickness is 5 cm. Temperature sensors in the zones measure the temperature distributions of the layers. Sixteen temperature distributions are located in some inner zone layers and in the insulated walls of the pond. The temperature distribution profiles are obtained using a data acquisition system (Karakilcik, 1998). To measure the temperature distributions of various regions, several temperature sensors are applied, at heights from the bottom of the pond of 0.05, 0.30, 0.55, 0.70, 0.80, 1.05, 1.35 and 1.50 m, and, from the bottom of the pond downward into the insulated bottom, at 15 and 45 mm, and for heights from the bottom of the side wall of 0, 0.35, 0.65, 0.75, 1.00 and 1.35 m.

The inner and wall temperatures of the pond are measured on an hourly basis throughout a day. The temperatures at the inner zones and ISW of the pond are measured by sensors with a range of $-65°C$ to $+155°C$, and with a measurement accuracy of $\pm 0.1°C$ for the temperature range of 0°C to 120°C. The sensors consist of 1N4148 semiconductor devices with coaxial cables lengths between 17 and 20 m. Solar energy data are obtained using a pyranometer, and hourly and daily average air temperatures are obtained from a local meteorological station. Further information on

Fig. 10.6. Experimental solar pond (Karakilcik et al., 2006a).

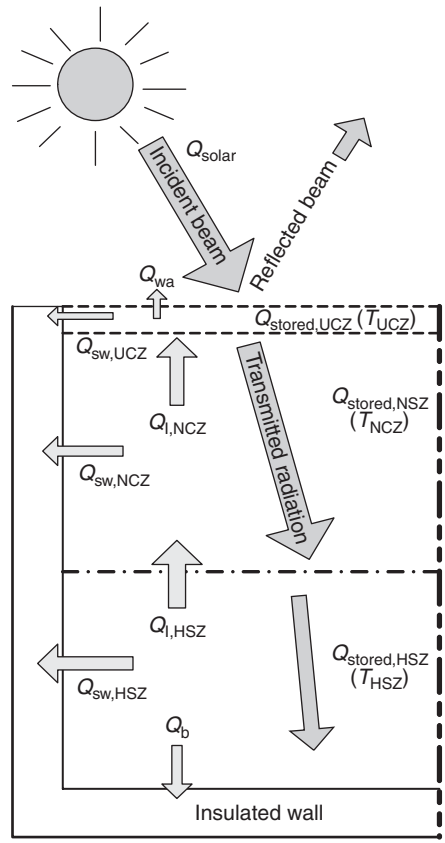

Fig. 10.7. Half-cut view of an insulated solar pond.

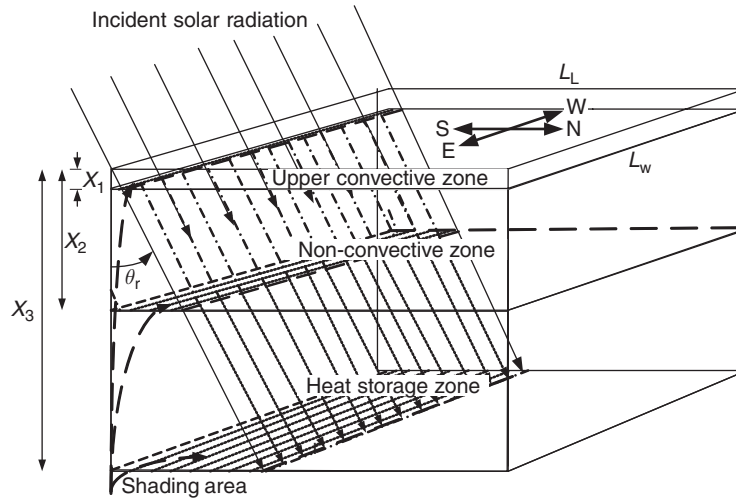

Fig. 10.8. Schematic of the insulated solar pond.

the experimental system, measurements and thermophysical properties of the utilized materials and fluids are available elsewhere (Karakilcik, 1998; Karakilcik et al., 2006a, b).

10.2.3. Energy analysis

As shown in Fig. 10.8, the UCZ, NCZ and HSZ thicknesses of the salt gradient solar pond are X_1, $X_2 - X_1$ and $X_3 - X_2$, respectively.

The working solution in the UCZ has uniform and low salinity (like seawater), while the working solution in the LCZ is stratified due to its high salinity and different density. In the NCZ, both concentration and temperature increase linearly with increasing pond depth. Part of the solar radiation incident on the solar pond is absorbed, part is reflected at the surface and the remaining part is transmitted, as illustrated in Figs. 10.9 through 10.11. In Figs. 10.9 and 10.10, most of the incident ray is transmitted through the layers and part of the transmitted ray which reaches the HSZ (Fig. 10.11) is converted to heat and stored there. The absorption by the salty water solutions changes with concentration of the solution.

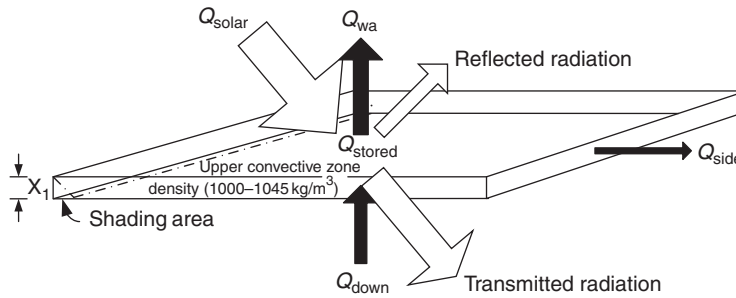

Fig. 10.9. UCZ of the solar pond.

Analysis of an experimental solar pond is generally complicated due to the differences of inner and outer conditions (e.g., pond dimensions, salty-water solutions, insulation, zone thicknesses, shading area of the layers, transmission and absorption characteristics for the layers). Here, we consider the following key parameters: zone thicknesses, temperatures in the layers, shading on the layers by the side walls, incident solar radiation absorbed by the layers, incident radiation reaching on the surface, heat losses through the ISW and thermal conductivity of the solution.

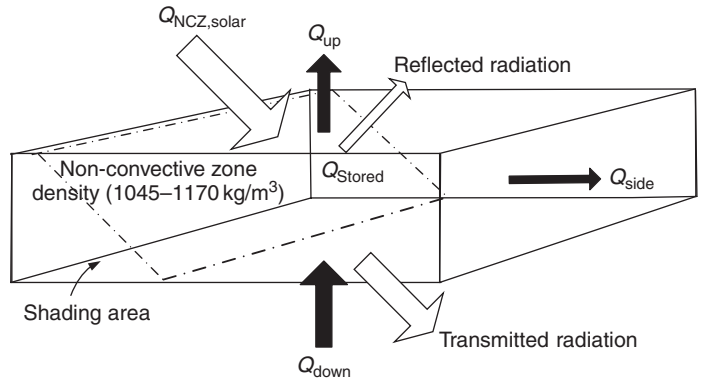

Fig. 10.10. NCZ of the solar pond.

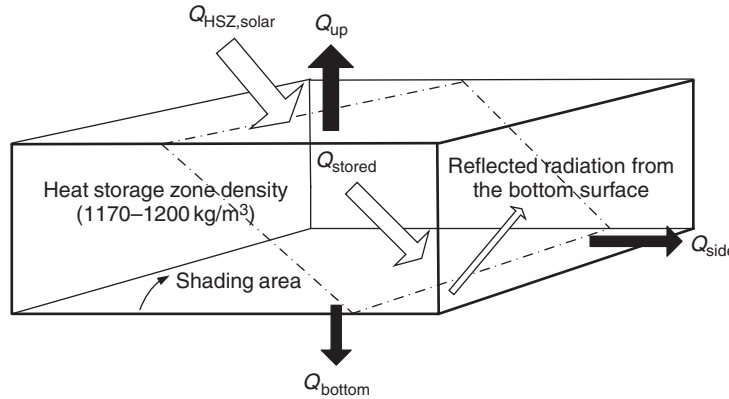

Fig. 10.11. HSZ of the solar pond.

To understand the thermal performance of a solar pond, the rates of absorption of the incident solar radiation by zone and the temperature distributions of its regions need to be determined. To realize this, the pond is treated as having three zones which are separated into 30 layer inner zones. The temperature variations of some layers depend on incident solar radiation on the horizontal surface, rates of absorption by the layers, local climate conditions, pond structure, time and insulation.

Energy efficiency for UCZ

In Fig. 10.9, energy flows for the UCZ of the pond are illustrated. Part of the incident solar radiation is reflected from the UCZ surface to air and lost. Part of the incident solar radiation is transmitted from the UCZ to the NCZ and the rest of the incident solar radiation is absorbed in the zone, heating it.

The thermal (energy) efficiency for the UCZ can generally be expressed as

$$\eta = \frac{Q_{net}}{Q_{in}} \tag{10.19}$$

Here, Q_{net} is the net heat addition to the pond and equals Q_{stored}, where

$$Q_{stored} = Q_{in} - Q_{out} = (Q_{solar} + Q_{down}) - (Q_{side} + Q_{wa}) \tag{10.20}$$

Here, Q_{stored} is the net heat stored in the UCZ, Q_{solar} is amount of the net incident solar radiation absorbed by the UCZ, Q_{down} is the total heat transmitted to the zone from the zone immediately below, Q_{side} is the total heat loss to the side walls of the pond, and Q_{wa} is the total heat lost to the surroundings from the upper layer.

Substituting Eq. (10.20) into Eq. (10.19) for the UCZ yields the following expression for the energy efficiency:

$$\eta_{\mathrm{UCZ}} = 1 - \frac{\{Q_{\mathrm{side}} + Q_{\mathrm{wa}}\}}{Q_{\mathrm{solar}} + Q_{\mathrm{down}}}$$

and

$$\eta_{\mathrm{UCZ}} = 1 - \frac{\{A_{01}R_{\mathrm{ps}}[T_{\mathrm{ucz}} - T_{\mathrm{side}}] + U_{\mathrm{wa}}A[T_{\mathrm{ucz}} - T_{\mathrm{amb}}]\}}{\left\{\beta EA_{(\mathrm{UCZ,I})}[1 - (1 - F)\mathrm{h}(X_1 - \delta)] + \dfrac{kA}{X_1}[T_{\mathrm{down}} - T_{\mathrm{ucz}}]\right\}} \tag{10.21}$$

where T_{amb} is the ambient air temperature, the value of which is taken to be that for the time of year, X_1 is the thickness of the UCZ; A_{01} is the surface area of the painted metal sheet on the side wall (and taken as $8 \times 0.05 = 0.4\,\mathrm{m}^2$ here); δ is the thickness of the layer in the UCZ which absorbs incident long-wave solar radiation; E is the total solar radiation incident on the pond surface, A is the upper surface area of the pond; and k is the thermal conductivity of the layers in the UCZ. The term R_{ps} is the thermal resistance of the painted metal sheet surrounding the first layer and can be written as $R_{\mathrm{ps}} = \frac{k_{\mathrm{p}}k_{\mathrm{s}}}{S_{\mathrm{p}}k_{\mathrm{s}} + S_{\mathrm{s}}k_{\mathrm{p}}}$.

Here k_{p} and k_{s} are thermal conductivities of the paint and iron-sheet, and S_{p} and S_{s} are the corresponding thicknesses. Also, β is the fraction of the incident solar radiation that enters the pond, and is expressed as follows (Hawlader, 1980):

$$\beta = 1 - 0.6\left[\frac{\sin(\theta_{\mathrm{i}} - \theta_{\mathrm{r}})}{\sin(\theta_{\mathrm{i}} + \theta_{\mathrm{r}})}\right]^2 - 0.4\left[\frac{\tan(\theta_{\mathrm{i}} - \theta_{\mathrm{r}})}{\tan(\theta_{\mathrm{i}} + \theta_{\mathrm{r}})}\right]^2$$

with θ_{i} and θ_{r} as the angles of incident and reflected solar radiation.

The ratio of the solar energy reaching the bottom of layer I to the total solar radiation incident on to the surface of the pond is given by Bryant and Colbeck (1977) as

$$h_{\mathrm{I}} = 0.727 - 0.056\,\ln\left[\frac{(X_1 - \delta)}{\cos\,\theta_{\mathrm{r}}}\right] \tag{10.22}$$

Here, A_{UCZ} is the net upper surface area of the UCZ (i.e., the effective area that receives incident solar radiation) and is defined as

$$A_{\mathrm{UCZ}} = L_{\mathrm{W}}[L_{\mathrm{L}} - (\delta + (I - 1)\Delta x)\tan\,\theta_{\mathrm{r}}] \tag{10.23}$$

where θ_{r} is the angle of the reflected incidence, Δx is the thickness of each layer in the UCZ and taken as 0.005 m in the calculations, and L_{W} and L_{L} are the width and length of the pond, respectively.

Energy efficiency for NCZ

In Fig. 10.10, energy flows for the NCZ of the pond are illustrated. The solar radiation incident on the surface of the NCZ, which is the part of the incident solar radiation on the surface of the pond, is transmitted from the UCZ. Little of the incident solar radiation on the NCZ is reflected from the NCZ to the UCZ. The reflected part of the incident solar radiation increases the UCZ efficiency. Part of the incident solar radiation is transmitted to the HSZ while part of the incident solar radiation is absorbed by the NCZ.

In Fig. 10.10, part of the incident solar radiation is absorbed by and transmitted into the NCZ, and part of the absorbed radiation is stored in the zone. So, the NCZ is heated and the zone's temperature increases. Thus, a temperature gradient occurs in this zone. Heating increases the NCZ efficiency, which can be calculated straightforwardly with Eq. (10.19).

Following Eq. (10.20), we can write an energy balance for the NCZ as

$$Q_{\mathrm{net}} = Q_{\mathrm{NCZ,solar}} + Q_{\mathrm{down}} - Q_{\mathrm{up}} - Q_{\mathrm{side}} \tag{10.24}$$

where $Q_{\mathrm{NCZ,solar}}$is amount of the solar radiation entering the NCZ which is transmitted from the UCZ after attenuation of incident solar radiation in the UCZ, and Q_{up} is the heat loss from the NCZ to the above zone.

We can then write the energy efficiency for the NCZ as:

$$\eta_{\mathrm{NCZ}} = 1 - \frac{\{Q_{\mathrm{side}} + Q_{\mathrm{up}}\}}{Q_{\mathrm{NCZ,solar}} + Q_{\mathrm{down}}}$$

or

$$\eta_{\mathrm{NCZ}} = 1 - \frac{\left\{\dfrac{kA}{\Delta X}[T_{\mathrm{UCZ}} - T_{\mathrm{NCZ}}] + A_{01}R_{\mathrm{ps}}[T_{\mathrm{NCZ}} - T_{\mathrm{side}}]\right\}}{\left\{\beta EA_{(\mathrm{NCZ})}[(1-F)[h(X_1-\delta) - h(X_1-\delta+\Delta x)]] + \dfrac{kA}{\Delta X}[T_{\mathrm{down}} - T_{\mathrm{NCZ}}]\right\}} \tag{10.25}$$

where F is the fraction of incident solar radiation absorbed by the pond's upper layer, and $\Delta X_{\mathrm{NCZ}} = (X_2 - X_1)$ is the thickness of the UCZ. Also, $A_{01,\mathrm{NCZ}}$ is the surface area of the painted metal sheet on the side walls surrounding of NCZ (taken as $8 \times 0.60 = 4.8\ \mathrm{m}^2$).

We define A_{NCZ} as the net upper surface area of the NCZ that receives the incident solar radiation as

$$A_{\mathrm{NCZ}} = L_{\mathrm{W}}[L_{\mathrm{L}} - (X_1 + (I-1)\Delta x)\tan\theta_{\mathrm{r}}] \tag{10.26}$$

Here, I varies from 2 to 14.

Energy efficiency for HSZ

Part of the solar radiation incident on the solar pond is transmitted through the UCZ and NCZ, after attenuation, to the HSZ. In Fig. 10.11, part of the transmitted solar radiation from the NCZ to the HSZ is reflected from the bottom and the majority of the solar radiation is absorbed in the HSZ. So, the HSZ temperature is increased and a temperature gradient develops in the zone.

An energy balance for the HSZ of the solar pond can be written as

$$Q_{\mathrm{net}} = Q_{\mathrm{HSZ,solar}} - Q_{\mathrm{bottom}} - Q_{\mathrm{up}} - Q_{\mathrm{side}} \tag{10.27}$$

where Q_{bottom} is the total heat loss to the bottom wall from the HSZ.

The energy efficiency for the HSZ of the solar pond then becomes

$$\eta_{\mathrm{HSZ}} = 1 - \frac{(Q_{\mathrm{bottom}} + Q_{\mathrm{up}} + Q_{\mathrm{side}})}{Q_{\mathrm{HSZ,solar}}}$$

or

$$\eta_{\mathrm{HSZ}} = 1 - \frac{\left\{AR_{\mathrm{ps}}[T_{\mathrm{down}} - T_{\mathrm{HSZ}}] + \dfrac{Ak}{\Delta X_{\mathrm{HSZ}}}[T_{\mathrm{HSZ}} - T_{\mathrm{up}}] + A_{01}R_{\mathrm{ps}}[T_{\mathrm{HSZ}} - T_{\mathrm{side}}]\right\}}{\{\beta EA_{(\mathrm{HCZ},I)}[(1-F)(h(X_3-\delta))]\}} \tag{10.28}$$

where $\Delta X_{\mathrm{HSZ}} = (X_3 - X_2)$ is the thickness of the HSZ of the pond. Also, $A_{01,\mathrm{HSZ}}$ is the surface area of the painted metal sheet on the side walls surrounding the HSZ (taken as $8 \times 0.80 = 6.4\ \mathrm{m}^2$). Note that the net surface area of the HSZ is equal to the net surface area at the bottom of the NCZ, i.e., $A_{\mathrm{HSZ},I} = \mathrm{A}_{\mathrm{NCZ},I}$; and I varies from 15 to 30.

Results of energy analysis

Energy flows in the inner zones of the pond are illustrated in Figs. 10.9 through 10.11. The performance of the solar pond depends on not only the thermal energy flows (e.g., heat losses and heat gains in the zones), but also the incident solar radiation flows (accounting for reflection, transmission and absorption). Also, shading decreases the performance of the zones.

In Fig. 10.9, it is seen that part of the incident solar radiation is reflected on the surface, some is absorbed by the layer and part (often most) is transmitted through the UCZ to the NCZ. The average sunny area of the UCZ is determined to be $3.93\ \mathrm{m}^2$, and the average shading area $0.07\ \mathrm{m}^2$. The net average solar radiation incident on the sunny area of the UCZ is calculated for January, May and August as 439.42, 2076.88 and 2042.00 MJ, respectively.

The greatest part of the incident solar radiation in Fig. 10.10 is transmitted to the NCZ from the UCZ. Part of the incident solar radiation is absorbed by the NCZ layers. The incident solar radiation transmitted from the NCZ to the HSZ is significant and little incident solar radiation is reflected from the NCZ to the UCZ. The average sunny area for the NCZ is found to be $3.13\ \mathrm{m}^2$, and the average shading area $0.87\ \mathrm{m}^2$. The net average solar radiation on the sunny area of the NCZ is calculated for January, May and August as 351.54, 1661.50 and 1634.05 MJ, respectively.

A significant part of the incident radiation in Fig. 10.11 reaches the HSZ from the NCZ. This transmitted solar radiation from the NCZ is absorbed in the HSZ, while little of the incident solar radiation is reflected from the HSZ to the upper zones. The average sunny area for the HSZ is found to be 2.63 m^2, and the average shading area 1.37 m^2. The net average solar radiation incident on the sunny area of the HSZ is calculated for January, May and August as 193.34, 913.83 and 898.73 MJ, respectively.

The stability of the salt density distribution in a solar pond is significant (Fig. 10.12). The primary reason for differences during different months is likely the higher temperature in summer. This change is mainly attributable to the thermophysical property of the salty water, heat losses from the pond to the air, and the absorption and reflection of incident solar radiation on the surface. The reason for the fluctuations in the saline density in the upper convective and NCZ is the increase in saline density of these zones due to the evaporation of water at the upper region. These changes can be reduced by continuously adding fresh water to the top of the pond. When not using one of the salt gradient protection systems for cleaning purposes in a month, significant changes occurred in the non-convective and upper convective regions. The averaged experimental density variations of salty water vs. height from the pond bottom for 12 months (see Fig. 10.12) show little differences between the density distributions in January, April and July, due to the temperature changes and evaporation of salty water from the pond. As expected, increasing temperature decreases the density more in the summer months.

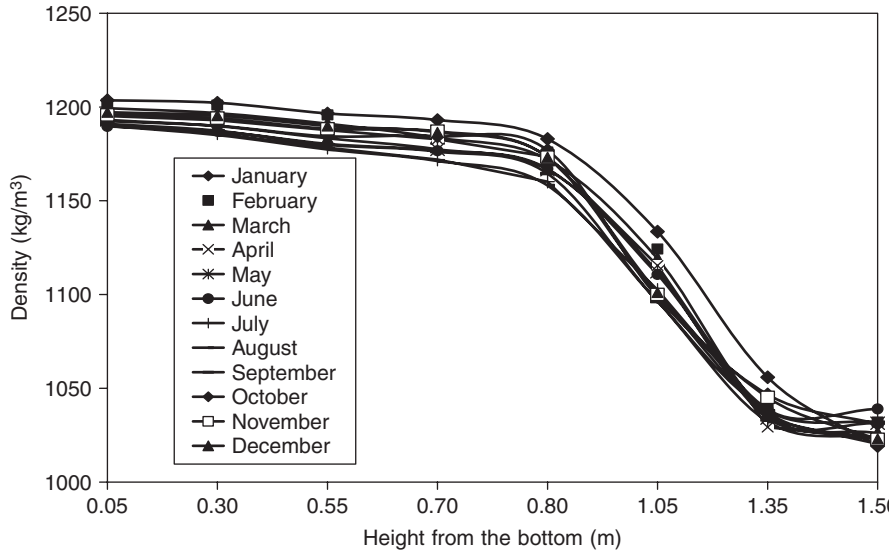

Fig. 10.12. Variation with height of salt density in the inner zones of the solar pond.

Heat losses by heat transfer from the pond during a day are determined by calculating the temperature differences for daily profiles of related months. To determine the heat losses from the inside of the solar pond, experimental temperature distribution profiles for the inner zones are obtained (see Fig. 10.13). Experimental temperature distributions are shown in Fig. 10.14 for different heights in the pond. The zone temperatures are measured throughout the months and averaged to find the monthly average temperatures at the respective points. It is clear that the zone temperatures vary with month of year, depending on the environment temperature and incoming solar radiation. The temperatures of the zones generally increase with incident solar energy per unit area of surface. Heat losses occur for each zone, with the largest in the storage zone, affecting its performance directly and significantly. To improve performance and increase efficiency, losses need to be reduced. The temperature distributions in Fig. 10.13 indicate that the temperature of the UCZ is a maximum of 35.0°C in August, a minimum of 10.4°C in January and 27.9°C in May. Similarly, the temperature of the NCZ is observed to be a maximum of 44.8°C in August, a minimum of 13.9°C in January and 37.9°C in May, while the temperature of the HSZ is observed to be a maximum of 55.2°C in August, a minimum of 16.9°C in January and 41.1°C in May. The net energy stored in the zones is calculated using property data in Table 10.1.

The energy stored in the UCZ is seen in Fig. 10.15 for January, May and August to be 3.99, 59.49 and 92.90 MJ, respectively. Similarly, the energy stored in the NCZ is seen in Fig. 10.16 for January, May and August to be 311.16,

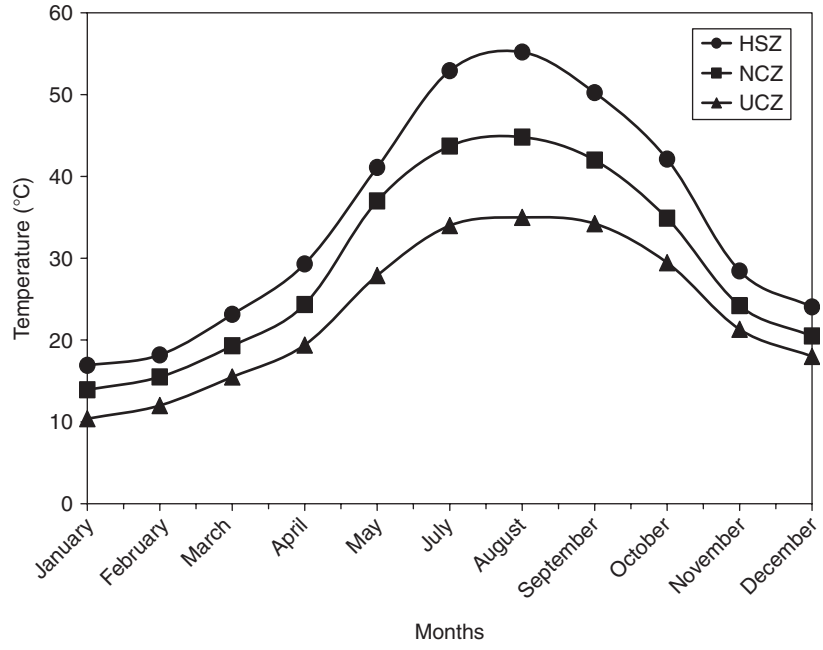

Fig. 10.13. Monthly average temperatures for the inner zones of the pond.

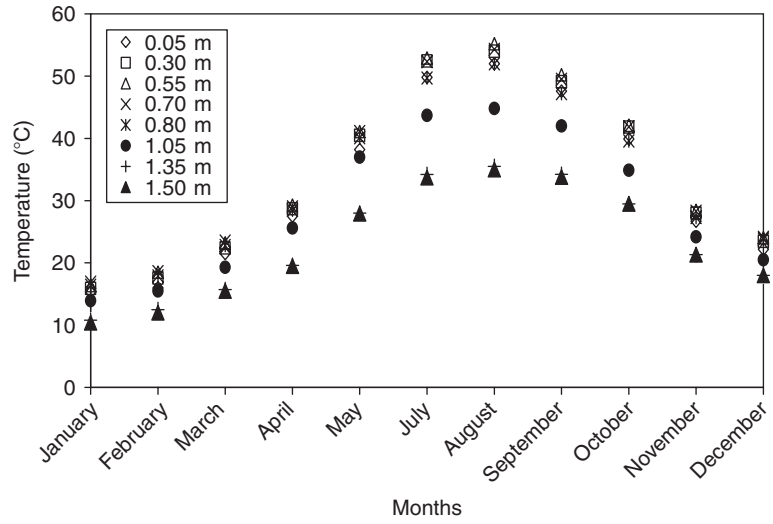

Fig. 10.14. Experimental zone temperature distributions in the inner zones of the solar pond.

Table 10.1. Thermophysical properties of water and other materials.

	Water	Saline water	Painted wall	Insulation	Air
Density (kg/m^3)	998	1185	7849	200	1.16
Thermal conductivity (J/m^1 K^1 h^1)	2160	–	21,200	143	94.68
Specific heat (J/kg^1 K^1)	4182	–	460	670	1007

Source: (Karakilcik, 1998; Dincer and Rosen, 2002).

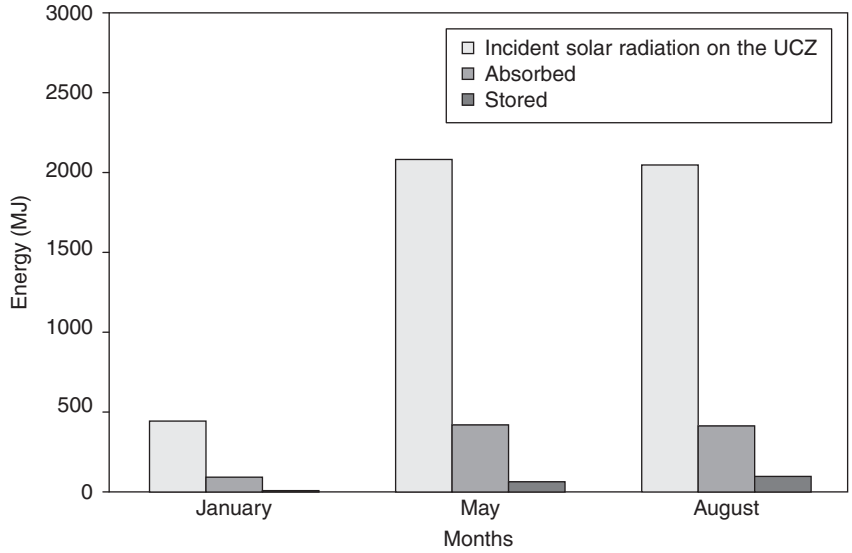

Fig. 10.15. Incident solar radiation on the UCZ that is absorbed and stored in the upper convective zone of the pond.

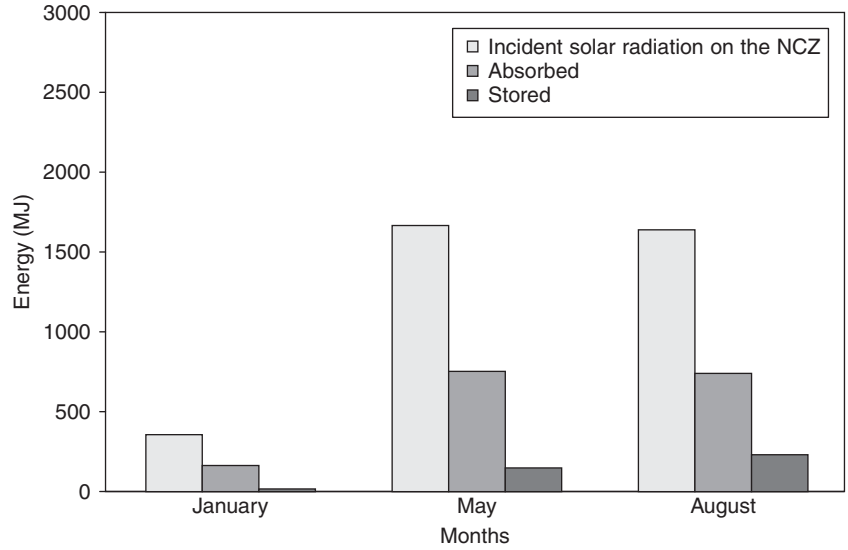

Fig. 10.16. Incident solar radiation on the UCZ that is absorbed and stored in the NCZ of the pond.

143.03 and 225.43 MJ, respectively, while the energy stored in the HSZ is seen in Fig. 10.17 for January, May and August to be 18.70, 160.31 and 252.65 MJ, respectively.

The UCZ efficiencies are seen in Fig. 10.18 to be 0.90%, 2.86% and 4.54% for January, May and August, respectively. This zone has little effect on the performance of the pond in January, and more impact in May and August. The efficiency of the UCZ is low because of the shading area rather than heat losses. The NCZ efficiencies are seen to be 3.17%, 8.60% and 13.79% for January, May and August, respectively. Shading decreases the performance of the NCZ. Shading area also has an important effect on the performance of the HSZ, for which the zone efficiencies are seen to be 9.67%, 17.54% and 28.11% for January, May and August, respectively.

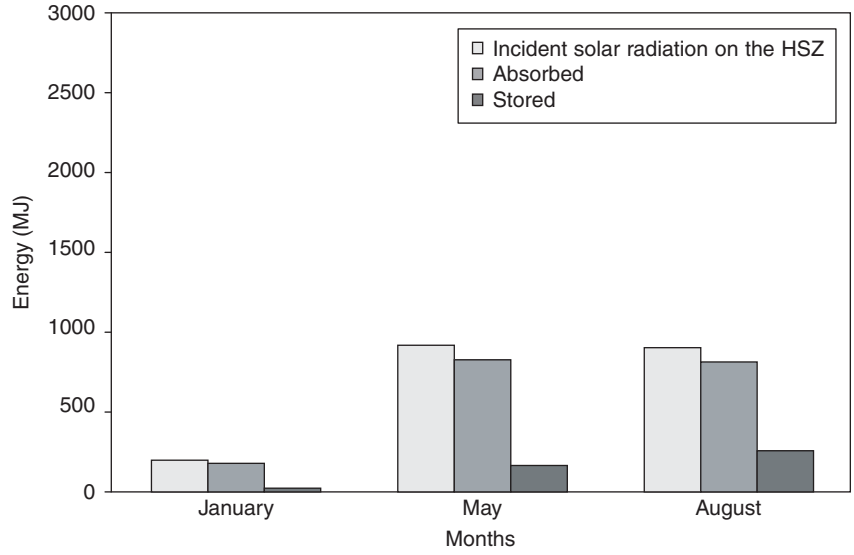

Fig. 10.17. Incident solar radiation on the UCZ that is absorbed and stored in the HSZ of the pond.

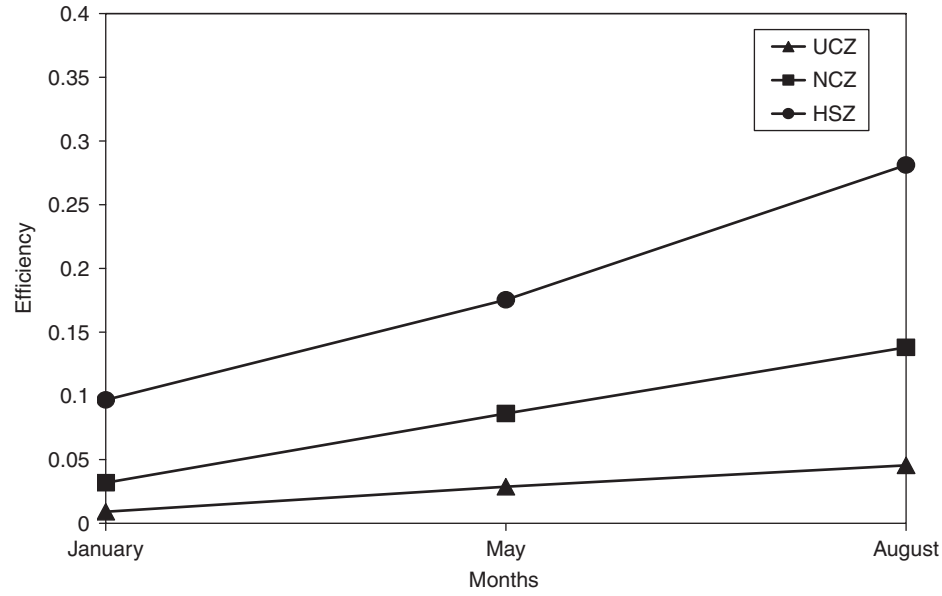

Fig. 10.18. Efficiencies of the inner zones of the pond for different months.

A significant amount of incident solar radiation is absorbed by the HSZ in August and little of the incident solar radiation is reflected from the bottom wall of the pond. Decreasing shading area from the top to the bottom of the pond allows less solar radiation to pass through and decreases the thermal potential of the pond and hence its performance. The performance of the thermal energy storage depends on the total radiation reaching the pond's zones. The performance of the heat storage zone can be usefully determined in part using energy efficiencies. But in a solar pond, the stored energy is very low compared to incident solar radiation on the surface of the zones, so the efficiencies are also very low. The efficiencies are low in part due to the low thermal conductivity of the pond filled with salty water. The efficiencies are dependent on the temperatures of the salty water and ambient air. The temperature differences of the zones between

January, May and August alter the inner zone temperatures, the diffusion of salt molecules up from the bottom and heat losses. This analysis illustrates the effect on pond efficiency of shading by the side wall and absorption, transmission and the thicknesses of the zones.

The experimental energy efficiency profiles for the UCZ, NCZ and HSZ of the pond, for different months, are given in Fig. 10.18. The maximum energy efficiencies of the inner zones are seen to occur in August, and the minimum efficiencies in January. Although the greatest amount of solar radiation is incident on the UCZ, the lowest efficiencies are found for this zone. This is because of the zone's small thickness and its large heat losses to air from its upper surface.

The temperature distribution profiles for the inner zones usually differ, causing the zone efficiencies to differ also. Despite the decrease in solar radiation intensity when it reaches the surface of the NCZ, that zone incurs lower heat losses and thus has a higher efficiency than the UCZ. The temperature distributions thus have an important effect on the performance of the pond.

The energy efficiency of the pond is negatively affected by the energy losses due to heat transfer from the UCZ to air. A low fraction of the incident solar radiation is stored in the pond and the UCZ efficiency is negligible especially compared to that of the NCZ. The NCZ efficiency consequently has a greater effect on the performance of the pond. Most of the energy is stored in the HSZ.

The inner regions of the pond thus store more energy in August than in January due to the considerable temperature differences between the zones. Heat storage, heat losses, shading areas and solar radiation absorption should be carefully considered when determining the thermal performance of solar ponds as their effects can be significant.

10.2.4. Exergy analysis

Exergy analysis permits many of the shortcomings of energy analysis of solar pond systems to be overcome, and thus appears to have great potential as a tool for design, analysis, evaluation and performance improvement. Figure 10.19 shows the energy and exergy flows for each of the zones in the pond. An exergy analysis of each zone is presented here.

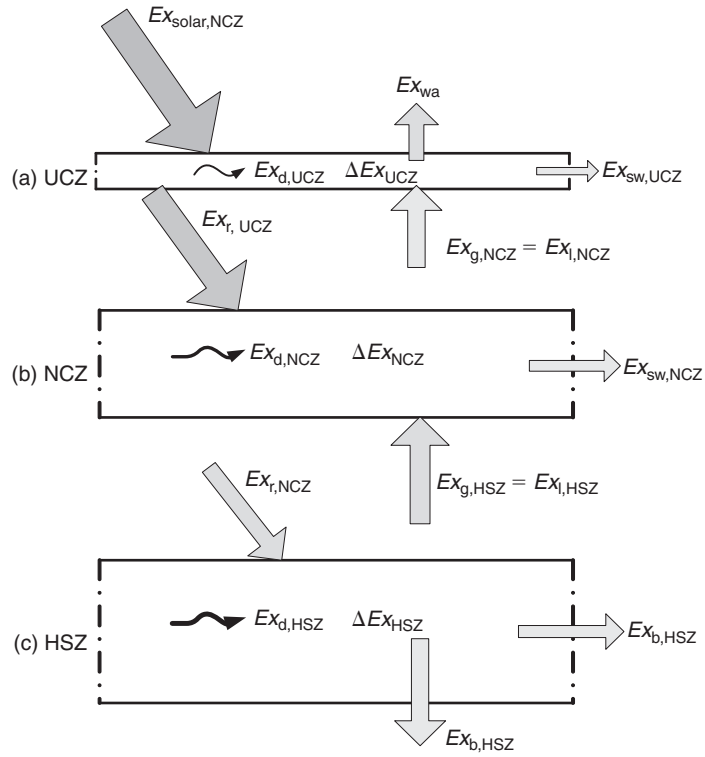

Fig. 10.19. Energy and exergy flows in the inner zones of the solar pond.

Exergy analysis for UCZ

Exergy flows in the UCZ are illustrated in Fig. 10.19a. We can write an exergy balance for the UCZ as

$$Ex_{\text{solar}} + Ex_{\text{g,NCZ}} = Ex_{\text{r,UCZ}} + Ex_{\text{d,UCZ}} + Ex_{\text{a}} + Ex_{\text{sw,UCZ}} \tag{10.29}$$

where Ex_{solar} is the exergy of the solar radiation reaching the UCZ surface, $Ex_{\text{g,NCZ}}$ is the exergy gained from the NCZ, $Ex_{\text{r,UCZ}}$ is the recovered exergy of the UCZ for the NCZ, $Ex_{\text{d,UCZ}}$ is the exergy destruction in the UCZ, $Ex_{\text{a,UCZ}}$ is the exergy loss from the UCZ to the ambient air and $Ex_{\text{sw,UCZ}}$ is the exergy loss through the side walls. Here $Ex_{\text{r,UCZ}}$ can be written according to Eq. (10.29) as

$$Ex_{\text{r,UCZ}} = Ex_{\text{ti}} - Ex_{\text{tl}} = (Ex_{\text{solar}} + Ex_{\text{g,NCZ}}) - (Ex_{\text{d,UCZ}} + Ex_{\text{a}} + Ex_{\text{sw,UCZ}}) \tag{10.30}$$

where Ex_{tl} is the total exergy losses, including exergy destruction, and Ex_{ti} is the total exergy input to the UCZ. The exergy of the solar radiation can be expressed, by modifying the expression of Petala (2003), as follows:

$$Ex_{\text{solar}} = E_{\text{net}} \left[1 - \frac{4T_0}{3T} + \frac{1}{3} \left(\frac{T_0}{T} \right)^4 \right] A_{\text{UCZ}} \tag{10.31}$$

The exergy gained from the NCZ can be expressed as

$$Ex_{\text{g,NCZ}} = m_{\text{NCZ}} C_{\text{p,NCZ}} \left[\left(T_{\text{m,NCZ}} - T_{\text{UCZ}} \right) - T_0 \left(\ln \frac{T_{\text{m,NCZ}}}{T_{\text{UCZ}}} \right) \right] \tag{10.32}$$

where E_{net} is the net incident solar radiation reaching the UCZ surface; A_{UCZ} is the net surface area of the UCZ and T is the sun's surface temperature, taken to be 6000 K (Petela, 2003); $m_{\text{NCZ}} = \rho_{\text{NCZ}} V_{\text{NCZ}}$ is the mass of salty water in the NCZ; ρ_{NCZ} is the averaged density (as seen in Table 10.2) and V_{NCZ} is the volume of the salty water in the NCZ ($V_{\text{NCZ}} = 2.4\,\text{m}^3$).

The exergy destruction in the UCZ can be written as

$$Ex_{\text{d,UCZ}} = T_0 \Delta S_{\text{net}} \tag{10.33}$$

where ΔS_{net} is the net entropy change of the UCZ, which is $\Delta S_{\text{net}} = \Delta S_{\text{sys}} + \Delta S_{\text{surr}}$. After substituting each of the entropy change terms, Eq. (10.33) becomes

$$Ex_{\text{d,UCZ}} = T_0 \left[m_{\text{UCZ}} C_{\text{p,UCZ}} \ln \frac{T_{\text{UCZ}}}{T_0} - \left(\frac{Q_{\text{wa}}}{T_{\text{UCZ}}} + \frac{Q_{\text{sw,UCZ}}}{T_0} \right) + \left(\frac{Q_{\text{g,NCZ}}}{T_{\text{NCZ}}} + \frac{Q_{\text{sw,UCZ}}}{T_0} \right) \right] \tag{10.34}$$

In addition, we can write the exergy losses to the ambient air and through the side walls as follows:

$$Ex_{\text{a,UCZ}} = m_{\text{UCZ}} C_{\text{p,UCZ}} \left[(T_{\text{UCZ}} - T_{\text{a}}) - T_0 \left(\ln \frac{T_{\text{UCZ}}}{T_{\text{a}}} \right) \right] \tag{10.35}$$

and

$$Ex_{\text{sw,UCZ}} = m_{\text{UCZ}} C_{\text{p,sw}} \left[\left(T_{\text{UCZ}} - T_{\text{sw,UCZ}} \right) - T_0 \left(\ln \frac{T_{\text{UCZ}}}{T_{\text{sw,UCZ}}} \right) \right] \tag{10.36}$$

where $m_{\text{UCZ}} = \rho_{\text{UCZ}} V_{\text{UCZ}}$ is the mass of salty water in the UCZ; ρ_{UCZ} is the averaged density and V_{UCZ} is the volume of the salty water in the UCZ ($V_{\text{UCZ}} = 0.4\,\text{m}^3$); $C_{\text{p,UCZ}}$ and $C_{\text{p,sw}}$ are the respective specific heats of the UCZ and insulating material; T_{a} and T_0 are the ambient temperature and the reference environment temperature, respectively and T_{UCZ}, $T_{\text{sw,UCZ}}$ and $T_{\text{m,NCZ}}$ denote the average temperatures of the UCZ, the side wall and the NCZ, respectively.

We can now define the exergy efficiency for the UCZ as the ratio of the exergy recovered from the UCZ to the total exergy input to the UCZ:

$$\psi_{\text{UCZ}} = \frac{Ex_{\text{r, UCZ}}}{Ex_{\text{ti}}} = 1 - \frac{Ex_{\text{d, UCZ}} + Ex_{\text{a}} + Ex_{\text{sw, UCZ}}}{Ex_{\text{solar}} + Ex_{\text{g, NCZ}}} \tag{10.37}$$

Table 10.2. Average monthly reference-environment temperatures and exergy contents of each zone.

	January	February	March	April	May	July	August	September	October	November	December
Reference temperature (°C)	10.0	11.0	14.2	17.6	22.0	28.0	28.0	26.0	21.0	16.0	11.0
Exergy input (UCZ) (MJ)	417.40	644.32	1160.85	1700.20	1976.24	2167.89	1982.47	1740.41	1299.94	782.72	506.14
Exergy recovered (MJ)	329.42	510.50	920.75	1347.54	1552.53	1681.57	1524.70	1344.78	1004.95	614.02	393.03
Exergy input (NCZ) (MJ)	335.05	516.70	930.67	1363.33	1588.13	1747.54	1601.34	1404.25	1048.74	629.23	407.89
Exergy recovered (MJ)	187.77	290.90	524.82	768.09	884.94	958.49	869.08	766.52	572.82	349.99	224.03
Exergy input (HCZ) (MJ)	187.77	290.98	524.82	768.09	884.94	958.50	869.08	766.52	572.82	349.99	224.03
Exergy stored (MJ)	17.12	27.19	53.15	89.27	140.79	204.40	218.00	181.39	133.28	57.03	27.92

Exergy analysis for NCZ

Fig. 10.19b shows the exergy flows in the NCZ. An exergy balance can be written as

$$Ex_{r,UCZ} + Ex_{g,HSZ} = Ex_{r,NCZ} + Ex_{d,NCZ} + Ex_{l,NCZ} + Ex_{sw,NCZ} \tag{10.38}$$

where $Ex_{r,UCZ}$ is the exergy recovered from the UCZ; $Ex_{g,HSZ}$ is the exergy gained from the HSZ, $Ex_{r,NCZ}$is the recovered exergy of the NCZ for the HSZ, $Ex_{d,NCZ}$is the exergy destruction in the NCZ, $Ex_{l,NCZ}$ is the exergy loss from the NCZ to the UCZ (which is equivalent to $Ex_{g,NCZ}$) and $Ex_{sw,NCZ}$ is the exergy loss through the side walls.

Here $Ex_{r,NCZ}$ can be expressed using Eq. (10.38) as

$$Ex_{r,NCZ} = Ex_{ti,NCZ} - Ex_{tl,NCZ} = (Ex_{r,UCZ} + Ex_{g,HSZ}) - \left(Ex_{d,NCZ} + Ex_{l,NCZ} + Ex_{sw,NCZ}\right) \tag{10.39}$$

where

$$Ex_{g,HSZ} = m_{HSZ} C_{p,HSZ} \left[(T_{HSZ} - T_{NCZ}) - T_0 \left(\ln \frac{T_{HSZ}}{T_{NCZ}} \right) \right] \tag{10.40}$$

Here, $m_{HSZ} = \rho_{HSZ} V_{HSZ}$ is the mass of salty water in the HSZ; ρ_{HSZ} is the average density and V_{HSZ} is the volume of salty water in the HSZ ($V_{HSZ} = 3.2\,m^3$).

The exergy destruction in the NCZ can then be written as

$$Ex_{d,NCZ} = T_0(\Delta S_{net,NCZ}) \tag{10.41}$$

where $\Delta S_{net,NCZ}$ is the net entropy change of the NCZ, which is $\Delta S_{net,NCZ} = \Delta S_{sys} + \Delta S_{surr}$.

The exergy losses, including the exergy destruction in the NCZ, can be derived as follows:

$$Ex_{d,NCZ} = T_0 \left[m_{NCZ} C_{p,NCZ} \ln \frac{T_{m,NCZ}}{T_0} - \left(\frac{Q_{g,NCZ}}{T_{m,NCZ}} + \frac{Q_{sw,NCZ}}{T_0} \right) + \left(\frac{Q_{g,HSZ}}{T_{m,NCZ}} + \frac{Q_{sw,NCZ}}{T_0} \right) \right] \tag{10.42}$$

$$Ex_{l,NCZ} = m_{NCZ} C_{p,NCZ} \left[\left(T_{m,NCZ} - T_{UCZ} \right) - T_0 \left(\ln \frac{T_{m,NCZ}}{T_{UCZ}} \right) \right] \tag{10.43}$$

$$Ex_{sw,NCZ} = m_{NCZ} C_{p,sw} \left[\left(T_{m,NCZ} - T_{sw,NCZ} \right) - T_0 \left(\ln \frac{T_{m,NCZ}}{T_{sw,NCZ}} \right) \right] \tag{10.44}$$

where $C_{p,NCZ}$is the specific heat of the NCZ and T_{HSZ} is the temperature of the HSZ.

We can now define the exergy efficiency for the NCZ as the ratio of the exergy recovered from the NCZ to the total exergy input to the NCZ:

$$\psi_{NCZ} = \frac{Ex_{r,NCZ}}{Ex_{ti}} = 1 - \frac{Ex_{d,NCZ} + Ex_{l,NCZ} + Ex_{sw,NCZ}}{Ex_{r,UCZ} + Ex_{g,HSZ}} \tag{10.45}$$

Exergy analysis HSZ

The exergy flows in the HSZ are shown in Fig. 10.19c and a zone exergy balance can be written as

$$Ex_{r,NCZ} - (Ex_{d,HSZ} + Ex_{l,HSZ} + Ex_{sw,HSZ} + Ex_{b,HSZ}) = \Delta Ex_{st} \tag{10.46}$$

where $Ex_{r,NCZ}$ is the recovered exergy from the NCZ for the HSZ, $Ex_{d,HSZ}$ is the exergy destruction in the HSZ, $Ex_{l,HSZ}$ is the exergy loss from the HSZ to the NCZ, $Ex_{sw,HSZ}$ is the exergy loss through the side walls. $Ex_{b,HSZ}$ is the exergy loss through the bottom wall and ΔEx_{st} is the exergy stored in the HSZ.

Here $Ex_{d,HSZ}$ is the exergy destruction in the HSZ which can be written as

$$Ex_{d,HSZ} = T_0(\Delta S_{net,HSZ}) \tag{10.47}$$

where $\Delta S_{net,HSZ}$ is the net entropy change of the HSZ and expressible as $\Delta S_{net,HSZ} = \Delta S_{sys} + \Delta S_{surr}$.

The exergy losses, including exergy destruction within the NCZ, can be written as follows:

$$Ex_{\mathrm{d,HSZ}} = T_0\left[m_{\mathrm{HSZ}}C_{\mathrm{p,HSZ}}\ln\frac{T_{\mathrm{HSZ}}}{T_0} - \left(\frac{Q_{\mathrm{g,HSZ}}}{T_{\mathrm{HSZ}}} + \frac{Q_{\mathrm{sw,HSZ}}}{T_0}\right) + \left(\frac{Q_{\mathrm{b}}}{T_0}\right)\right] \tag{10.48}$$

$$Ex_{\mathrm{l,HSZ}} = m_{\mathrm{HSZ}}C_{\mathrm{p,HSZ}}\left[\left(T_{\mathrm{HSZ}} - T_{\mathrm{m,NCZ}}\right) - T_0\left(\ln\frac{T_{\mathrm{HSZ}}}{T_{\mathrm{m,NCZ}}}\right)\right] \tag{10.49}$$

where $C_{\mathrm{p,HSZ}}$ is the specific heat of the salty water in the HSZ. For the side wall,

$$Ex_{\mathrm{sw,HSZ}} = m_{\mathrm{HSZ}}C_{\mathrm{p,sw}}\left[\left(T_{\mathrm{HSZ}} - T_{\mathrm{sw,HSZ}}\right) - T_0\left(\ln\frac{T_{\mathrm{HSZ}}}{T_{\mathrm{sw,HSZ}}}\right)\right] \tag{10.50}$$

Note that $Ex_{\mathrm{b,HSZ}} = Ex_{\mathrm{sw,HSZ}}$ due to the fact that both the side wall and the bottom layer have the same insulating materials and are surrounded by ambient air.

The exergy efficiency for the HSZ is expressible as the ratio of the exergy stored in the HSZ to the total exergy input to the HSZ which is essentially the exergy recovered from the NCZ:

$$\psi_{\mathrm{HSZ}} = \frac{\Delta Ex_{\mathrm{st}}}{Ex_{\mathrm{r,NCZ}}} = 1 - \frac{\{Ex_{\mathrm{d,HSZ}} + Ex_{\mathrm{l,HSZ}} + Ex_{\mathrm{sw,HSZ}} + Ex_{\mathrm{b,HSZ}}\}}{Ex_{\mathrm{r,NCZ}}} \tag{10.51}$$

Results of exergy analysis

Energy and exergy efficiencies are compared for the UCZ, NCZ and HSZ in the solar pond, illustrating how exergy is important for determining true magnitudes of the losses in each zone.

Figure 10.20 shows both averaged energy and exergy content variations of the pond three zones vs. month of year. The exergy content distributions in the zones are the calculated monthly average temperatures as listed in Table 10.2. The exergy contents are less than the corresponding energy contents. Although energy is conserved, some exergy is destroyed in each zone in addition to the exergy losses to the surrounding air. As seen in Fig. 10.20, the lowest-exergy contents occur in January and the highest in July. The temperature of the surroundings plays a key role since the energy and exergy losses are rejected to the ambient air. The distribution of the energy and exergy contents by month follows the solar irradiation profile closely.

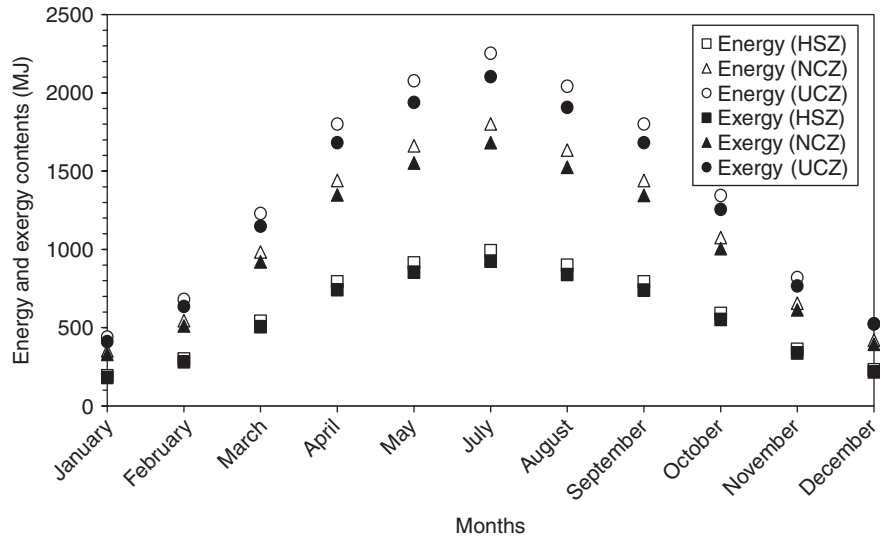

Fig. 10.20. Energy and exergy content distributions of the solar pond zones.

Figure 10.21 shows the variations of exergy input, exergy recovered and exergy destruction and losses for the UCZ over the year, except for June when measurements were not taken due to maintenance on the data acquisition system. The exergy inputs are equal to the sum of the exergy recovered and the exergy destruction and losses. For simplicity, no exergy accumulation is assumed to occur in this zone (calculations show it is less than 1%). The exergy input is highest in July when incoming solar irradiation is greatest, and the other exergy terms appear to be proportional to the input. The exergy recovered in this zone is transferred to the NCZ. The maximum and minimum exergy recovered are 1681.57 MJ in July and 392.42 MJ in January, respectively. The distribution by month is somewhat similar to the distribution in Fig. 10.20.

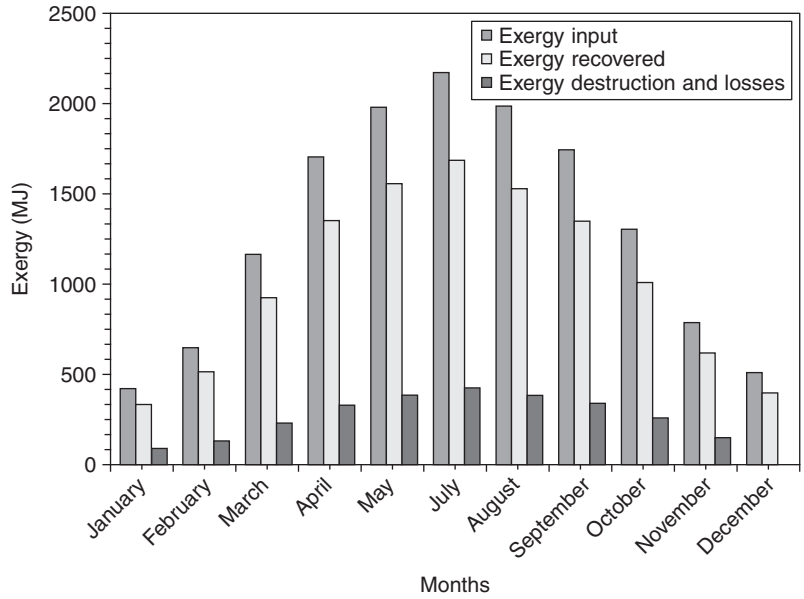

Fig. 10.21. Exergy distributions in the UCZ of the solar pond.

Figure 10.22 shows the variations of exergy input, exergy recovered and exergy destruction and losses for the NCZ over the year. Again, the exergy inputs are equal to the sum of the exergy recovered and exergy destruction and losses. No exergy accumulation is assumed. Also, the exergy is highest in July when solar irradiation is greatest and the other exergy terms are proportional to exergy input. The exergy recovered in this zone is transferred to the HSZ. The maximum and minimum exergy recovered are 958.48 MJ in July and 187.77 MJ in January, respectively. The exergy input to and recovered from this zone are listed in Table 10.2.

Figure 10.23 exhibits the distributions of exergy input, exergy stored and exergy destruction and losses for the HSZ over the year. In this zone, exergy is stored instead of recovered. This storage capability allows solar ponds to undertake daily and/or seasonal storage. The exergy input is equal to the sum of the exergy recovered and the exergy destruction and losses. The exergy stored is much smaller than the exergy input and exergy destruction and losses in the HSZ, and reaches a maximum in July of 743.10 MJ and a minimum in January of 169.68 MJ. The exergy values for each month are listed in Table 10.2.

Figure 10.24 compares the energy and exergy efficiencies for the zones over the year. As seen in the figure, the differences between energy and exergy efficiencies are small during the cooler months, and largest from May to October. As expected, the HSZ efficiencies are higher than the corresponding UCZ and NCZ efficiencies. Consequently, the inner zones of the pond store more exergy in July than in January due to the considerable temperature differences between the zones. The exergy destruction and losses significantly affect the performance of the pond and should be minimized to increase system efficiency.

10.2.5. Closure

Energy and exergy analyses have been carried out for an insulated salt gradient solar pond and its UCZ, NCZ and HSZ. Pond performance is affected strongly by the temperature of the LCZ and the temperature profile with pond

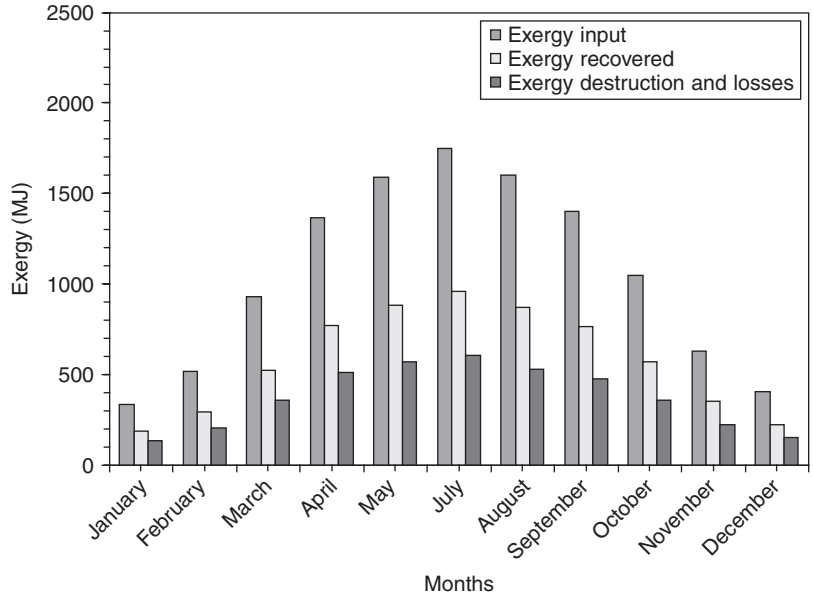

Fig. 10.22. Exergy distributions in the NCZ of the solar pond.

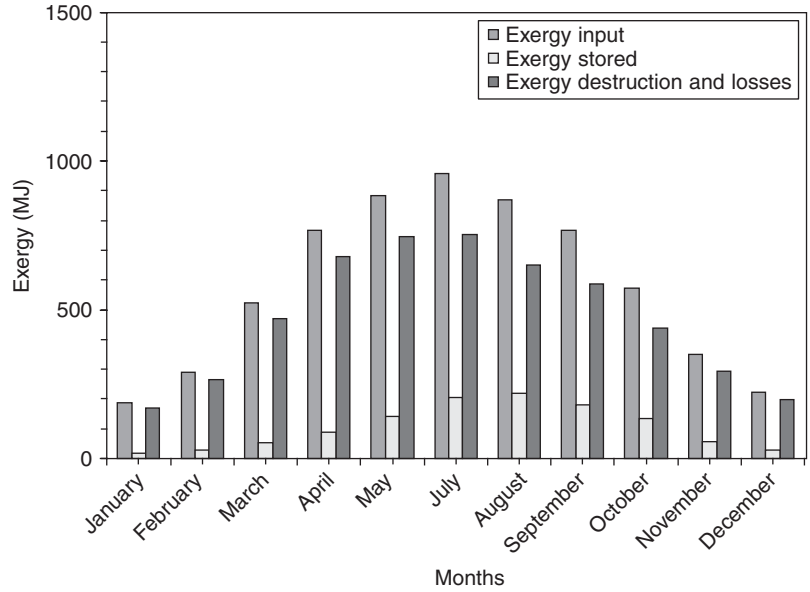

Fig. 10.23. Exergy distributions in the HSZ of the solar pond.

depth. The sunny area and the temperature of the LCZ are sensitive to wall shading. Due to the presence of insulation, heat losses from the sides and bottom of the pond are negligibly small. To increase the efficiency for the storage zone of the pond, heat losses from upper zone, bottom and side walls, reflection, and shading areas in the NCZ and HSZ should be decreased. The temperature of each layer of the inner zones depends on the incident radiation, zone thicknesses, shading areas of the zones and overall heat losses. So, to increase pond performance, the zone thicknesses should be modified to achieve higher efficiency and stability of the pond. Through careful design parameter modifications, pond performance can be maintained even if the incoming solar radiation reaching the zones is increased.

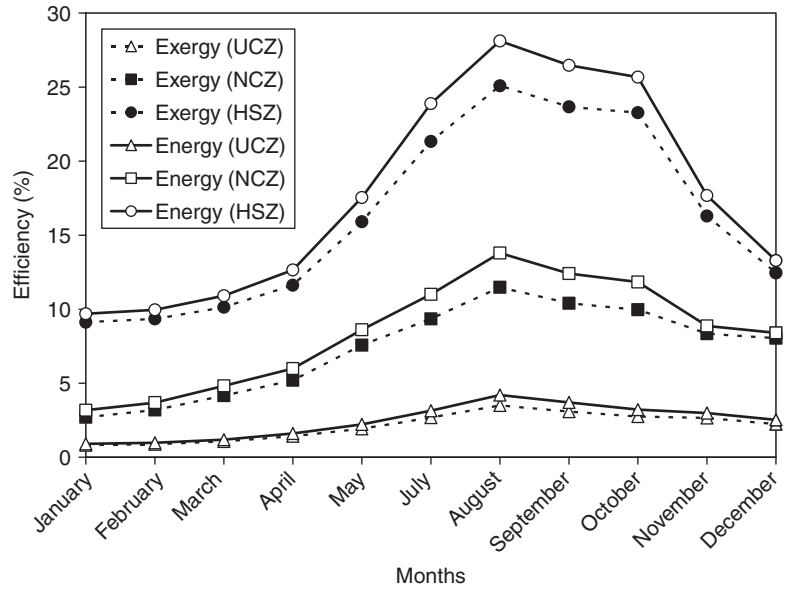

Fig. 10.24. Variation of energy and exergy efficiencies of the solar pond zones.

Exergy efficiencies are lower than the energy efficiencies for each zone of the pond due to the small magnitudes of exergy destructions in the zones and losses to the surroundings. It is important to determine the true magnitudes of these destructions and losses and minimize these for performance improvement of the pond.

Experimental data are used to determine the efficiencies for each layer of the zones for a real insulated solar pond. Several parameters for the UCZ and NCZ having influences on the thermal performance are discussed. It is shown that the introduction of the UCZ and NCZ provides many conveniences in calculating the storage efficiency in the heat storage zone, and in determining the relations with heat loads and a best operating state. Therefore, the energy and exergy efficiencies of the inner zones of a solar pond are important parameters in practical applications.

10.3. Exergy analysis of wind energy systems

Wind power is a form of renewable energy in that it is replenished daily by the sun. Warm air rises as portions of the earth are heated by the sun, and other air rushes in to fill the low-pressure areas, creating wind power. The characteristics of wind affect the design of systems to exploit its power. Wind is slowed dramatically by friction as it flows over the ground and vegetation, often causing it not to be very windy at ground level. Wind can be accelerated by major land forms, leading some regions to be very windy while other areas remain relatively calm. When wind power is converted to electricity, it can be transported over long distances and thus can serve the needs of urban centers where large populations live.

Wind energy is among the world's most significant and rapidly developing renewable energy sources. Recent technological developments, concerns over fossil fuel demands and the corresponding environmental effects and the continuous increase in the consumption of conventional energy resources have reduced relative wind energy costs to economically acceptable levels in many locations. Wind energy farms, which have been installed and operated in some instances for more than 25 years, consequently, are being considered as an alternative energy source in many jurisdictions.

In practice wind power is converted to electricity by a wind turbine. In typical, modern, large-scale wind turbines, the kinetic energy of wind (the energy of moving air molecules) is converted to rotational motion by a rotor, on which is mounted a device to 'capture' the wind. This device is often a three-bladed assembly at the front of the wind turbine, but can also come in other geometries and types. The rotor turns a shaft which transfers the motion into the nacelle (the large housing at the top of a wind turbine tower). Inside the nacelle, the slowly rotating shaft enters a gearbox that greatly increases the rotational shaft speed. The output shaft rotating at a high-speed is connected to a generator that converts the rotational motion to electricity at a medium voltage (a few hundred volts). The electricity flows along heavy electric cables inside the tower to a transformer, which increases the voltage of the electric power to a level more suitable for distribution

(a few thousand volts). Transformation is carried out because higher voltage electricity flows with less resistance through electric lines, generating less heat and fewer power losses. The distribution-voltage power flows through underground cables or other lines to a collection point where the power may be combined with that from other turbines. In many cases, the electricity is distributed for use to nearby farms, residences and towns. Otherwise, the distribution-voltage power is sent to a substation where its voltage is increased dramatically to transmission-voltage levels (a few hundred thousand volts) and transported through transmission lines many kilometers to distant cities and factories.

Most new and renewable energy sources, such as wind, solar, hydraulic and wave energy, are related to meteorological variables. If the meteorological characteristics of these renewable energy sources are not well known and understood, there can be important gaps in knowledge related to energy investments.

This section presents a thermodynamic analysis of wind energy using energy and exergy. The analysis provides a physical basis for understanding, refining and predicting the variations in wind energy calculations. A wind energy efficiency definition based on exergy analysis is provided.

This section contains several parts. First, wind energy and its components are discussed. Second, exergy analysis is applied to wind, and the exergy is formulated of wind energy and its components. Third, energy and exergy efficiencies are compared and shown to depend on the area considered. Last, a spatio-temporal mapping approach to wind exergy analysis is provided.

10.3.1. Wind energy systems

As a meteorological variable, wind energy refers to the energy content of wind. In electricity generation wind plays the same role as water does for hydraulic generation. Wind variables are important in such applications. Wind velocity deviation and changeability depend on time and location. Understanding such characteristics is the subject of wind velocity modeling. Determining the atmospheric boundary layer and modeling is a special consideration in wind power research. Much research has been carried out on these subjects. For instance, Petersen et al. (1998) considered wind power meteorology and sought relationships between meteorology and wind power. During the preparation of the Denmark Wind Atlas detailed research was performed on wind energy as a meteorological energy source (Petersen et al., 1981).

Meteorological variables such as temperature, pressure and moisture play important roles in the occurrence of wind. Generally, in wind engineering, moisture changeability is negligible and air is assumed to be dry. Wind as a meteorological variable can be described as a motion of air masses on a large scale with potential and kinetic energies. Pressure forces lead to kinetic energy (Freris, 1981; 1990). In wind engineering applications horizontal winds are important because they cover great areas.

The dynamic behavior of the atmosphere generates spatio-temporal variations in such parameters as pressure, temperature, density and moisture. These parameters can be described by expressions based on continuity principles, the first law of thermodynamics, Newton's law and the state law of gases. Mass, energy and momentum conservation equations for air in three dimensions yield balance equations for the atmosphere. Wind occurs due to different cooling and heating phenomena within the lower atmosphere and over the earth's surface. Meteorological systems move from one place to another by generating different wind velocities.

With the growing significance of environmental problems, clean energy generation has become increasingly important. Wind energy is clean, but it usually does not persist continually for long periods of time at a given location. Fossil fuels often must supplement wind energy systems. Many scientific studies have addressed this challenge with wind energy (e.g., Justus, 1978; Cherry, 1980; Troen and Petersen, 1989; Sahin, 2002).

During the last decade, wind energy applications have developed and been extended to industrial use in some European countries including Germany, Denmark and Spain. Successes in wind energy generation have encouraged other countries to consider wind energy as a component of their electricity generation systems. The clean, renewable and in some instances economic features of wind energy have drawn attention from political and business circles and individuals. Development in wind turbine technology has also led to increased usage. Wind turbine rotor efficiency increased from 35% to 40% during the early 1980s, and to 48% by the mid-1990s. Moreover, the technical availability of such systems has increased to 98% (Salle et al., 1990; Gipe, 1995; Karnøe and Jørgensen, 1995; Neij, 1999). Today, total operational wind power capacity worldwide has reached approximately 46,000 MW.

Koroneos et al. (2003) applied exergy analysis to renewable energy sources including wind power. This perhaps represents the first paper in the literature about wind turbine exergy analysis. But in this paper only the electricity generation of wind turbines is taken into account and the exergy efficiency of wind turbines for wind speeds above 9 m/s is treated as zero. Koroneos et al. only considered the exergy of the wind turbine, depending on electricity generation with no entropy generation analysis. In an extended version of this study, Jia et al. (2004) carried out an exergy analysis of wind energy

and considered wind power for air compression systems operating over specified pressure differences, and estimated the system exergy efficiency. As mentioned before, Jia et al. wanted to estimate exergy components and to show pressure differences, and realized this situation by considering two different systems, a wind turbine and an air compressor, as a united system.

Dincer and Rosen (2005) investigated thermodynamic aspects of renewables for sustainable development. They explain relations between exergy and sustainable development. Wind speed thermodynamic characteristics are given by Goff et al. (1999), with the intent of using the cooling capacity of wind as a renewable energy source (i.e., using the wind chill effect for a heat pump system).

Although turbine technology for wind energy is advancing rapidly, there is a need to assess accurately the behavior of wind scientifically. Some of the thermodynamic characteristics of wind energy are not yet clearly understood. The capacity factor of a wind turbine sometimes is described as the efficiency of a wind energy turbine. But there are difficulties associated with this definition. The efficiency of a wind turbine can be considered as the ratio of the electricity generated to the wind potential within the area swept by the wind turbine. In this definition only the kinetic energy component of wind is considered. Other components and properties of wind, such as temperature differences and pressure effects, are neglected.

10.3.2. Energy and exergy analyses of wind energy aspects

People sense whether air is warm or cool based not only on air temperature, but also on wind speed and humidity. During cold weather, faster wind makes the air feel colder because it removes heat from our bodies faster. Wind chill is a measure of this effect, and is the hypothetical air temperature in calm conditions (air speed $V = 0$) that would cause the same heat flux from the skin as occurs for the actual air speed and temperature. The heat transfer for an air flow over a surface is slightly modified in some versions of the wind chill expression (Stull, 2000).

The present wind chill expression is based on the approaches of Osczevski (2000) and Zecher (1999), and was presented at the Joint Action Group for Temperature Indices (JAG/TI) meeting held in Toronto (2001). The JAG/TI expression makes use of advances in science, technology and computer modeling to provide a more accurate, understandable and useful formula for calculating the dangers from winter winds and freezing temperatures. In addition, clinical trials have been conducted and the results have been used to verify and improve the accuracy of the expression, which is given as

$$T_{\text{windch}} = 35.74 + 0.6215T_{\text{air}} - 35.75(V^{0.16}) + 0.4274T_{\text{air}}(V^{0.16}) \tag{10.52}$$

where the wind chill temperature T_{windch} is in °F and wind speed V is in mph.

Another wind speed factor is wind pressure. When the wind approaches an obstacle, the air flows around it. However, one of the streamlines that hits the obstacle decelerates from the upstream velocity of v_s to a final velocity of zero (or to some lower velocity). The pressure (dynamic pressure) at this stagnation point is higher than the free stream pressure (static pressure) well away from the obstacle. The dynamic pressure can be calculated from Bernoulli's equation. For flow at constant altitude, the only two terms that change in Bernoulli's equation are kinetic energy and pressure.

As explained earlier, for evaluating entropy generation we need system inlet and outlet temperature and pressure differences. Here our approach is to use the windchill effect to be able to determine the changes in heat capacities of wind. The Bernoulli equation is employed for calculating entropy generation.

Energy analysis

Wind energy E is the kinetic energy of a flow of air of mass m at a speed V. The mass m is difficult to measure and can be expressed in terms of volume V through its density $\rho = m/V$. The volume can be expressed as $V = AL$ where A is the cross-sectional area perpendicular to the flow and L is the horizontal distance. Physically, $L = Vt$ and wind energy can be expressed as

$$E = \frac{1}{2}\rho AtV^3 \tag{10.53}$$

Betz (1946) applied simple momentum theory to the windmill established by Froude (1889) for a ship propeller. In that work, the retardation of wind passing through a windmill occurs in two stages: before and after its passage through the windmill rotor. Provided that a mass m is air passing through the rotor per unit time, the rate of momentum change is $m(V_1 - V_2)$ which is equal to the resulting thrust. Here, V_1 and V_2 represent upwind and downwind speeds at a considerable distance from the rotor. The power absorbed P can be expressed as

$$P = m(V_1 - V_2)\overline{V} \tag{10.54}$$

On the other hand, the rate of kinetic energy change in wind can be expressed as

$$E_{\mathrm{k}} = \frac{1}{2} m(V_1^2 - V_2^2) \tag{10.55}$$

The expressions in Eqs. (10.54) and (10.55) should be equal, so the retardation of the wind, $V_1 - \overline{V}$, before the rotor is equal to the retardation, $\overline{V} - V_2$, behind it, assuming that the direction of wind velocity through the rotor is axial and that the velocity is uniform over the area A. Finally, the power extracted by the rotor is

$$P = \rho A \overline{V}(V_1 - V_2)\overline{V} \tag{10.56}$$

Furthermore,

$$P = \rho A \overline{V}^2 (V_1 - V_2) = \rho A \left(\frac{V_1 + V_2}{2} \right)^2 (V_1 - V_2) \tag{10.57}$$

and

$$P = \rho \frac{A V_1^3}{4} [(1 + \alpha)(1 - \alpha^2)] \quad \text{where} \quad \alpha = \frac{V_2}{V_1} \tag{10.58}$$

Differentiation shows that the power P is a maximum when $\alpha = \frac{1}{3}$, i.e., when the final wind velocity V_2 is equal to one-third of the upwind velocity V_1. Hence, the maximum power that can be extracted is $\rho A V_1^3 \frac{8}{27}$, as compared with $\frac{\rho A V_1^3}{2}$ in the wind originally, i.e., an ideal windmill could extract 16/27 (or 0.593) of the power in the wind (Golding, 1955).

Exergy analysis

As pointed out earlier, energy and exergy balances for a flow of matter through a system can be expressed as

$$\sum_{\mathrm{in}} (h + ke + pe)_{\mathrm{in}} m_{\mathrm{in}} - \sum_{\mathrm{ex}} (h + ke + pe)_{\mathrm{ex}} m_{\mathrm{ex}} + \sum_{\mathrm{r}} Q_{\mathrm{r}} - W = 0 \tag{10.59}$$

$$\sum_{\mathrm{in}} ex_{\mathrm{in}} m_{\mathrm{in}} - \sum_{\mathrm{ex}} ex_{\mathrm{ex}} m_{\mathrm{ex}} + \sum_{\mathrm{r}} Ex^{Q} - Ex^{W} - I = 0 \tag{10.60}$$

where m_{in} and m_{ex} denote mass input across port 'in' and mass exiting across port 'ex', respectively; Q_{r} denotes the amount of heat transfer into the system across region r on the system boundary; Ex^{Q} is the exergy transfer associated with Q_{r}; W is the work (including shaft work, electricity, etc.) transferred out of the system; Ex^{W} is the exergy transfer associated with W; I is the system exergy consumption; and *h, ke, pe*, and *ex* denote specific values of enthalpy, kinetic energy, potential energy and exergy, respectively. For a wind energy system, the kinetic energy and pressure terms are of particular significance.

For a flow of matter at temperature T, pressure P, chemical composition μ_{j} of species j, mass m, specific enthalpy h, specific entropy s, and mass fraction x_{j} of species j, the specific exergy can be expressed as:

$$ex = [ke + pe + (h - h_0) - T_0(s - s_0)] + \left[\sum_{\mathrm{j}} (\mu_{\mathrm{j}0} - \mu_{\mathrm{j}00}) x_{\mathrm{j}} \right] \tag{10.61}$$

where T_0, P_0 and $\mu_{\mathrm{j}00}$ are intensive properties of the reference environment. The physical component (first term in square brackets on the right side of the above equation) is the maximum available work from a flow as it is brought to the environmental state. The chemical component (second term in square brackets) is the maximum available work extracted from the flow as it is brought from the environmental state to the dead state. For a wind turbine, kinetic energy is dominant and there is no potential energy change or chemical component. The exergy associated with work is

$$Ex^{W} = W \tag{10.62}$$

The exergy of wind energy can be estimated with the work exergy expression, because there are no heat and chemical components.

Energy and exergy efficiencies

The energy (η) and exergy (ψ) efficiencies for the principal types of processes considered in this section are based on the ratio of product to total input. Here, exergy efficiencies can often be written as a function of the corresponding energy efficiencies. The efficiencies for electricity generation in a wind energy system involve two important steps:

1. *Electricity generation from shaft work*: The efficiencies for electricity generation from the shaft work produced in a wind energy system are both equal to the ratio of the electrical energy generated to the shaft work input.
2. *Shaft work production from the kinetic energy of wind*: The efficiencies for shaft work production from the kinetic energy of a wind-driven system are both equal to the ratio of the shaft work produced to the change in kinetic energy Δke in a stream of matter m_s.

The input and output variables for the system are described in Fig. 10.25. Output wind speed is estimated using the continuity equation. The total electricity generated is related to the decrease in wind potential. Subtracting the generated power from the total potential gives the wind turbine back-side wind potential (Fig. 10.25):

$$V_2 = \sqrt[3]{\frac{2(E_{\text{potential}} - E_{\text{generated}})}{\rho A t}} \tag{10.63}$$

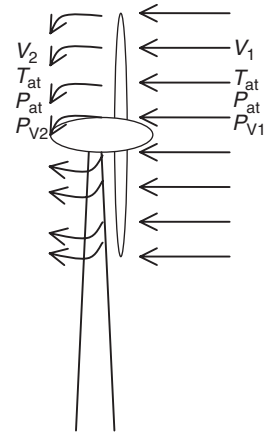

Fig. 10.25. Wind turbine and representative wind energy input and output variables.

In addition, the total kinetic energy difference gives the generated electricity which can be written as

$$\Delta KE = E_{\text{generated}} \tag{10.64}$$

Air mass flow with time depends on density and wind speed, and can be shown as

$$\dot{m} = \rho A V \tag{10.65}$$

The exergy of a matter flow is defined as the maximum work that can be acquired when the air flows from state (T_2, P_2) to the ambient state (T_1, P_1). The enthalpy change ΔH from state 1 and state 2 can be expressed as

$$\Delta H = \dot{m} C_p (T_2 - T_1) \tag{10.66}$$

where $\dot{m}$ is mass flow rate of air, which depends on time, T_1 is the wind chill temperature at the input to the wind turbine; and T_2 is the wind chill temperature at the exit of the wind turbine. The total entropy of the system and entropy difference can be written as

$$\Delta S = \Delta S_{\text{system}} + \Delta S_{\text{surround}} \tag{10.67}$$

$$\Delta S = \dot{m} T_{at} \left(C_p \ln\left(\frac{T_2}{T_1}\right) - R \ln\left(\frac{P_2}{P_1}\right) - \frac{Q_{loss}}{T_{at}} \right) \tag{10.68}$$

where

$$P_i = P_{at} \pm \frac{\rho}{2} V^2 \tag{10.69}$$

and

$$Q_{loss} = \dot{m} C_p (T_{at} - T_{average}) \tag{10.70}$$

Here, ΔS is the specific entropy change, T_{at} is the atmospheric temperature, P_2 is the pressure at the exit of the wind turbine for a wind speed V_2 and P_1 is the pressure at the inlet of the wind turbine for a wind speed V_1, Q_{loss} represents heat losses from the wind turbine and $T_{average}$ is the mean value of input and output wind chill temperatures. Thus, the total exergy for wind energy can be expressed using the above equations as

$$Ex = E_{generated} + \dot{m} C_p (T_2 - T_1) + \dot{m} T_{at} \left(C_p \ln\left(\frac{T_2}{T_1}\right) - R \ln\left(\frac{P_2}{P_1}\right) - \frac{Q_{loss}}{T_{at}} \right) \tag{10.71}$$

The first term on the right side of this equation is the generated electricity. The second and third parts are enthalpy and entropy contributions, respectively.

10.3.3. Case study

The wind energy resource and several wind energy technologies are assessed from an exergy perspective.

System considered

In order to evaluate and assess wind energy potential, a database is considered of hourly wind speed and direction measurements taken between May 2001 and May 2002 at seven stations in the northern part of Istanbul (40.97°E longitude, 29.08°N latitude). For this research, values from only one station are considered. This area comes under the influence of the mild Mediterranean climate during summer, and consequently experiences dry and hot spells for about 4 to 5 months, with comparatively little rainfall. During winter, this region comes under the influence of high-pressure systems from Siberia and the Balkan Peninsula and low-pressure systems from Iceland. Hence, northeasterly or westerly winds influence the study area, which also has high rainfall in addition to snow every year in winter. Air masses originating over the Black Sea also reach the study area (Sahin, 2002).

Results and discussion

In this section, measured generated power data from a group in Denmark are used to obtain a power curve. Pedersen et al. (1992) recommend wind turbine power curve measurements be used to determine the wind turbine required in relation to technical requirements and for approval and certification of wind turbines in Denmark. Here, output electrical power data for a 100 kW wind turbine with a rotor diameter at 18 m and hub height 30 m are given. The data power curve of this wind turbine is shown in Fig. 10.26a. The power curve exhibits two main types of behavior, depending on wind speed. At low wind speeds, power increases with wind speed until the rated power wind speed is reached. A second degree polynomial curve fit can be obtained using a least squares minimization technique. A curve is fitted between the cut-in and rated power wind speeds and its coefficient of determination (R^2) is estimated as 0.99. At high wind speeds (above 16 m/s), the power generation levels off and then tends to decrease from the rated power with increasing wind speed. The cut-out wind speed of this turbine is 20.3 m/s. In the rated wind speed region, a third degree polynomial curve is fitted and its R^2 value is calculated as 0.78. The fitted curves for electrical power generation, based on measured data, are illustrated in Fig. 10.26b.

The exergy analysis of wind energy shows that there are significant differences between energy and exergy analysis results. According to one classical wind energy efficiency analysis technique, which examines capacity factor, the resultant wind energy efficiency is overestimated. The capacity factor normally refers to the percentage of nominal power that the wind turbine generates. The given test turbine capacity factor is also compared with modeled desired area calculations. It is seen that, as for the power curves in Fig. 10.26, there is a close relation between capacity factors. The differences between exergy and energy efficiencies are shown in Fig. 10.27. Below the cut-in wind speed (3.8 m/s)

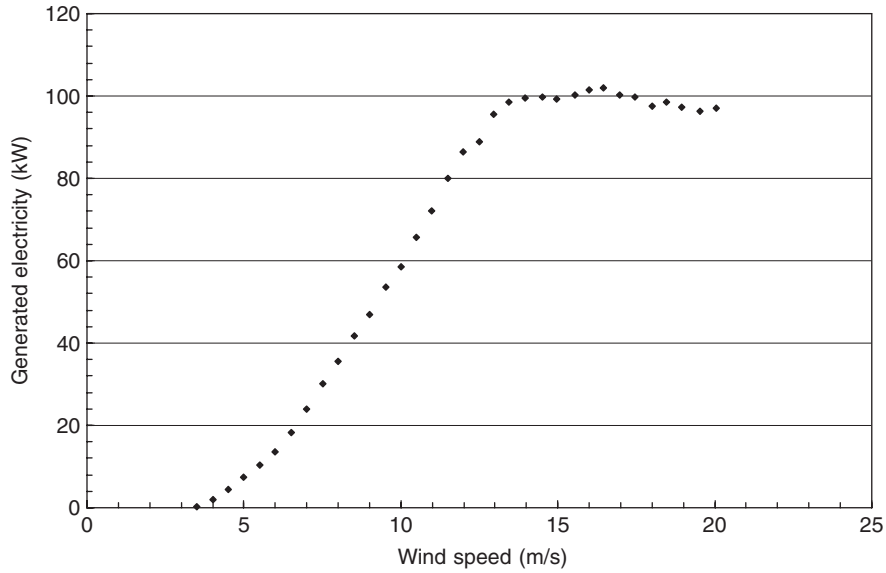

Fig. 10.26a. Test wind turbine power curve, showing electricity generated as a function of wind speed.

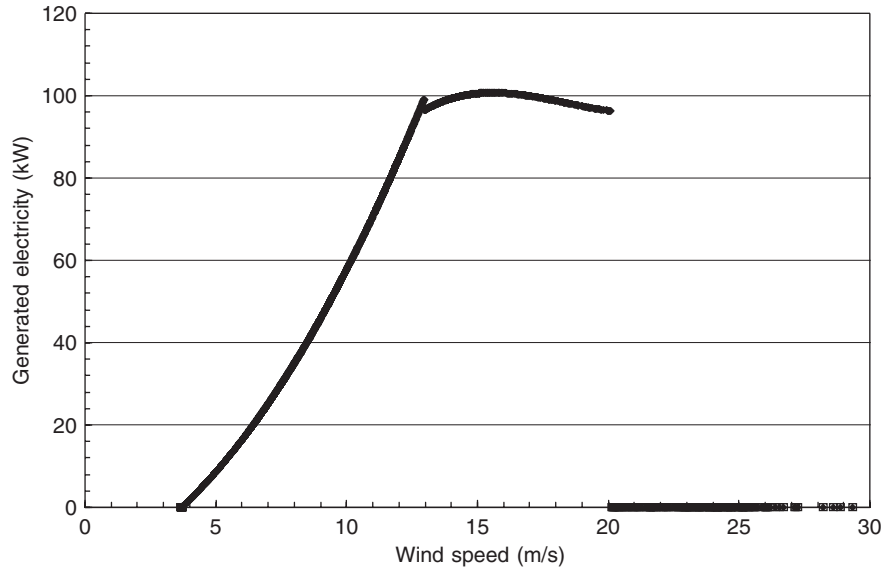

Fig. 10.26b. Test wind turbine power curve, showing regression curves for electricity generated as a function of wind speed.

and over the cut-out wind speed (20.3 m/s) electricity generation is zero, so energy and exergy efficiencies also are zero in those ranges. Since wind speed exhibits high variability during the day, with greater fluctuations than all other meteorological parameters, the fluctuations in energy and exergy efficiency values are high.

All exergy efficiencies are calculated for a selected point, and given in Fig. 10.28 as 24 hour moving average values. In this figure, the moving average values are used to show that the daily changes depend on seasonal variability and to see the periodicity of the exergy efficiencies. Moving average is a statistical method for smoothing highly fluctuating variables. In this study, 24 hour moving average is considered to illustrate daily variability. The data show that during spring and summer an approximately constant variability is observed, but in winter the fluctuations increase. In other

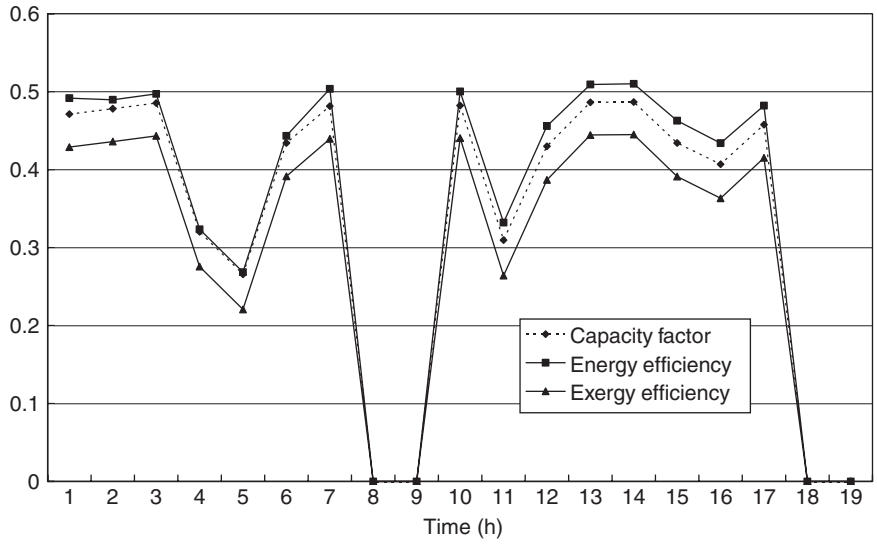

Fig. 10.27. Variation of capacity factor and energy and exergy efficiencies, using a sample set of wind data during the day.

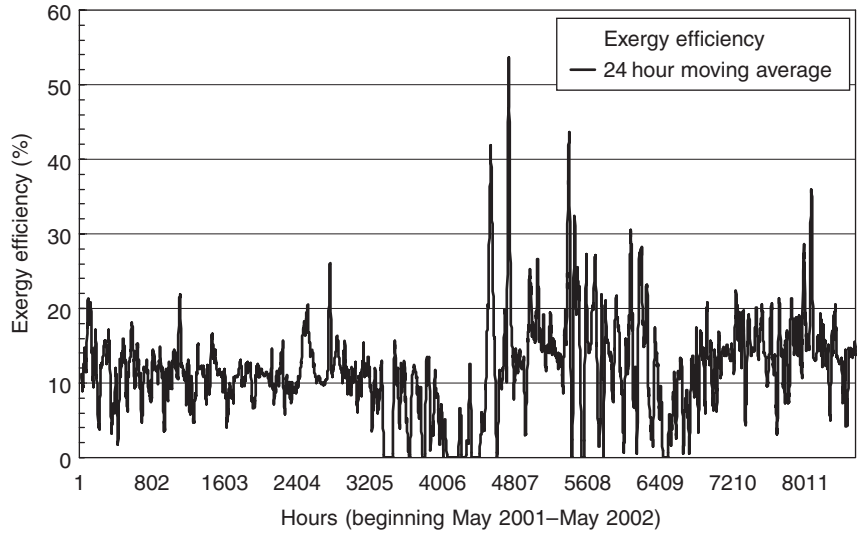

Fig. 10.28. Mean daily exergy efficiencies.

words, during high wind speeds and cold weather the efficiencies are more variable. In addition, exergy efficiencies of wind energy are low in autumn. After autumn, high wind speeds occur since the region comes under the influence of high pressure from Siberia and the Balkan Peninsula and low pressure from Iceland.

Figures 10.27 and 10.28 show the variations and large fluctuations of the efficiencies. These figures are more useful for meteorological interpretation than engineering application. For power generation application, electricity generation, which depends on the power curves, is estimated. Then, the enthalpy and entropy parts of Eq. (10.79) are calculated, and the energy and exergy efficiencies are evaluated. For each efficiency calculation, 8637 data values are employed. Then, regression analysis is applied to wind speeds between the cut-in and cut-out levels, and energy and exergy efficiencies are calculated (Fig. 10.29). The lowest efficiencies are observed at the cut-in and cut-out wind speeds. As seen in Fig. 10.30, energy and exergy efficiencies exhibit important differences at every wind speed. We suggest that exergy efficiencies

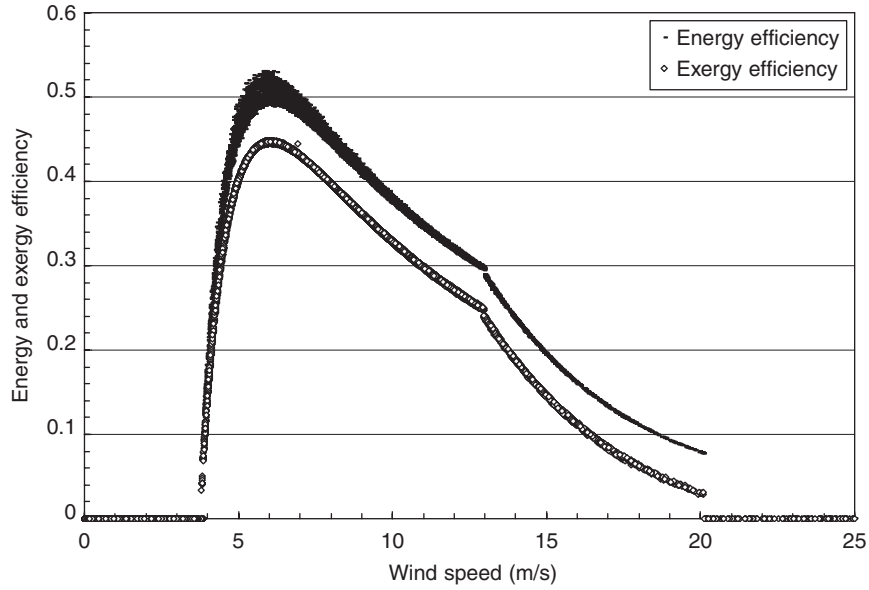

Fig. 10.29. Variation of energy and exergy efficiencies as a function of wind speed.

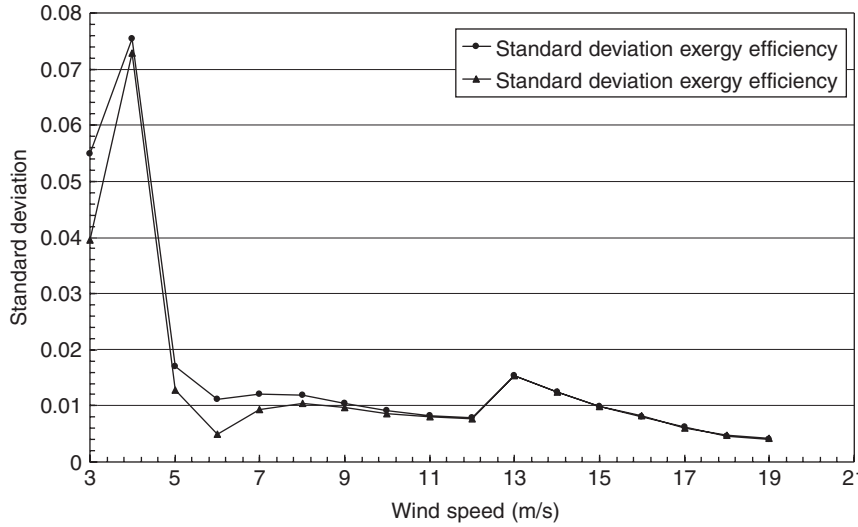

Fig. 10.30. Standard deviation of exergy and energy efficiencies with wind speed.

be used in assessments instead of energy efficiencies. Such an approach yields more realistic results and provides more information about wind energy systems.

In Fig. 10.29, it is seen that the exergy efficiency curve is smoother than the energy efficiency curve. In other words, deviations for energy efficiencies are higher than for exergy efficiencies. To illustrate these variations, mean standard deviations of these efficiencies are calculated for each wind speed interval (Fig. 10.30). It is observed that at lower wind speeds standard deviations for energy efficiencies are higher than those for exergy efficiencies. Above wind speeds of 9 m/s, the same standard deviations are observed.

In Fig. 10.31, mean energy and exergy efficiencies are presented as a function of wind speed. This figure emphasizes the differences between the efficiencies, and shows the over-estimation provided by energy efficiencies. The relative differences between energy and exergy efficiencies, where exergy efficiency is taken as the base value, are given in the same figure. There, it is seen that the relative difference is lowest at a wind speed of about 7 m/s, and increases at lower

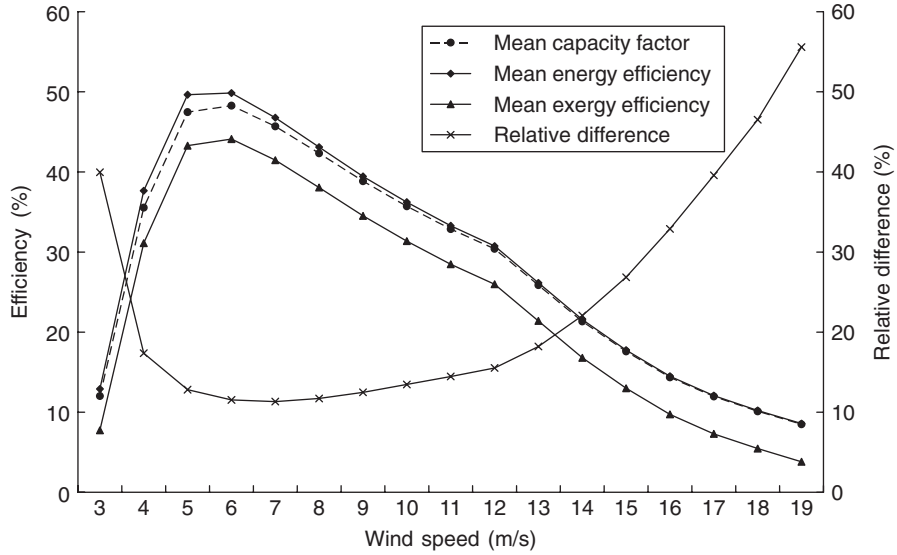

Fig. 10.31. Mean exergy and energy efficiencies, and percent differences between these values, as a function of wind speed. Mean capacity factor is also shown.

and higher wind speeds. These relative differences imply that exergy methods should be applied to wind energy systems for better understanding.

10.3.4. Spatio-temporal wind exergy maps

Most variations in atmospheric characteristics and properties depend on location. Hence, spatial modeling of wind is an important subject in wind engineering studies. Generally, spatial and temporal variations are studied separately. Spatial modeling of wind is achieved by mapping and using objective analysis methods, as reported in the meteorology and wind engineering literature. Various methods exist for data interpolation from measurement stations to any desired point (Cressman, 1959; Barnes, 1964; Schlatter, 1988).

Other estimation methods for wind properties at any desired point, where spatial correlation structure determines the weights applicable to each observation, are the optimal interpolation method of Gandin (1963); the cumulative semivariogram method of Sen (1989) and the approaches of Sen and Sahin (1998). In addition, Sahin (2002) has suggested a spatio-temporal approach based on trigonometric point cumulative semivariogram.

Geostatistics, originally proposed by Krige (1951) and developed by Matheron (1963), is now widely applied in earth sciences as a special branch of applied statistics (Davis, 1986). One of the most common mapping techniques in wind power meteorology is the European wind atlas methodology, which is based on the calculation methods of roughness change class effects and speed-up models for flow passes. It is equally important to construct a model for the effect of sheltering obstacles on the terrain, such as houses and shelter belts, through the so-called shelter model. Topography and wind climatology are essential in distinguishing landscapes. Surface wind speed time-series distribution functions are calculated by fitting the Weibull distribution with the scale, c, and the shape, k, parameters plotted at five heights, four roughness classes and eight direction sectors. The roughness change model is initially expanded to multiple roughness changes, and subsequently developed into a more general model capable of handling roughness areas extracted directly from topographical maps (Troen and Peterson, 1989).

This section describes a spatio-temporal map approach to wind exergy analysis, based on the data from an irregular set of stations scattered over an area. Other exergy analyses of wind energy generating systems do not provide exergy maps showing spatial and temporal parameters. Energy and exergy efficiency models for wind generating systems are used to produce exergy monthly maps based on Krige's method (Krige, 1951). With these maps for a specific system, exergy efficiencies at any location in the considered area can be estimated using interpolation. A case study is presented that applies these models to 21 climatic stations in Ontario, Canada to show how exergy efficiencies change and how these maps compare with energy efficiency maps.

Table 10.3. Topographical characteristics of selected meteorological stations in Ontario.

Station	Latitude (°N)	Longitude (°W)	Altitude (m)
Atikokan	48.45	91.37	395
Big Trout Lake	53.50	89.52	220
Dryden Airport	49.50	92.45	413
Kapuskasing	49.25	82.28	227
Kenora	49.47	94.22	407
Kingston	44.13	76.36	93
London	43.02	81.09	278
Moosonee	51.16	80.39	10
North Bay	46.21	79.26	358
Ottawa	45.19	75.40	116
Red Lake	51.04	93.48	375
Simcoe	46.29	84.30	187
Sault Ste Marie	42.51	80.16	241
Sioux Lookout	50.07	91.54	398
Sudbury	46.37	80.48	348
Thunder Bay	48.22	89.19	199
Timmins	48.34	81.22	295
Toronto Pearson Airport	43.40	79.38	173
Trenton	44.07	77.32	85
Wiarton	44.45	81.06	222
Windsor	42.16	82.58	190

Source: Ontario Weather Data (2004).

Generating wind energy maps

Energy and exergy efficiencies are estimated using measured generated power data from a Denmark group, as noted earlier. It is seen that capacity factors of this wind turbine system are very high even without considering enthalpy values. The capacity factor is approximately 45% for wind speeds of 8–11 m/s. Maps of estimated efficiencies for 21 stations in Ontario are subsequently developed. In this illustration, 30-year average wind speed, temperature and pressure data that were taken from Ontario Weather Data (2004) are used for these stations (Table 10.3). Wind speed values are interpolated from 10 to 30 m. The 100 kW wind turbine with a 30 m hub height is especially selected to minimize wind speed interpolation errors. This region is a lake area so interactions between water and land surfaces are very high. As a result of these topographical properties, continuous high wind speeds occur. Another important feature of this region is low temperatures with high wind speeds, leading to high wind chill temperatures.

Seasonal wind energy maps

January, April, July and October geostatistical spatio-temporal maps are developed and discussed here. These maps are intended to show the differences between energy and exergy efficiencies of a specific wind turbine system at the

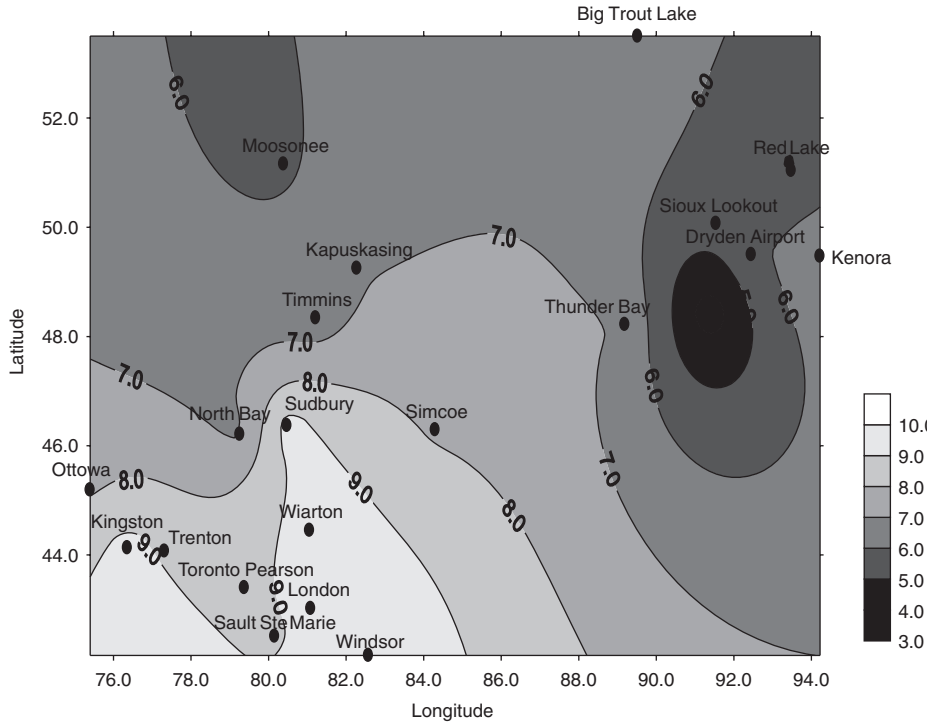

Fig. 10.32a. Map of wind speed (in units of m/s) at a height of 30 m for January for Ontario.

same conditions through exergy analysis. This analysis also gives more information and describes how efficiently wind energy is used, how much losses occur, and the locations of these losses and inefficiencies. Each month is taken to be representative of one season. The 21 stations considered are scattered throughout the map in Fig. 10.32a, where the scale of the map is given at right side. The bottom right of this map shows Lake Ontario, where climatological data are not measured, so this area is not discussed. Low wind speeds are observed in the east and north parts of Ontario in January. The monthly minimum average value observed in Atikokan in this month is below the typical wind-turbine cut-in wind speed and as a result there is no electricity generation. The monthly maximum average wind speed observed in southwestern Ontario is 9–10 m/s (Fig. 10.32a).

The estimated energy efficiencies and a corresponding map is developed for January. At low wind speeds, efficiencies are high, but this does not mean that at these values the wind turbine is more efficient than rated for that wind speed. Rather, it means that the generated electricity is low and also the potential of wind energy is low at these wind speeds. As a result, the ratio between generated electricity and potential energy is high (Fig. 10.32b). The same observations apply for exergy and, in addition, the contours for exergy efficiency are seen to be lower than those for energy efficiency for all regions. The average exergy efficiency value is 40%. This exergy map allows interpolation to be used to estimate parameter values in regions for which there are no measured data. Hence, this kind of map can be used for practical engineering applications (Fig. 10.32c).

For meaningful comparisons of energy and exergy efficiencies, the wind speed maps should be considered together. Here, differences between energy and exergy efficiencies are multiplied by 100 and divided by the highest value. Relative differences between energy and exergy efficiencies are shown in Fig. 10.32d. Large relative differences in energy efficiency values are observed, especially at low wind speeds. Contrary to this, the relative differences between energy and exergy efficiencies at high wind speeds are smaller. But these values are higher than 10% at all stations. These differences are large and should not be neglected in energy planning and management (Fig. 10.32d).

Wind speed values are clustered in three main groups. The lowest wind speed is higher than the wind speed cut-in. The highest wind speed is 10 m/s. In April, electricity can be generated at all stations. Like for the January map, the highest wind speed values in April are observed in southwestern parts of Ontario (Fig. 10.33a). In the energy efficiency map for April, the efficiencies successively increase from south to north. Because of the low wind speeds, energy efficiencies in the northern parts of this region are approximately 50%. There are also three clusters in this efficiency map (Fig. 10.33b).

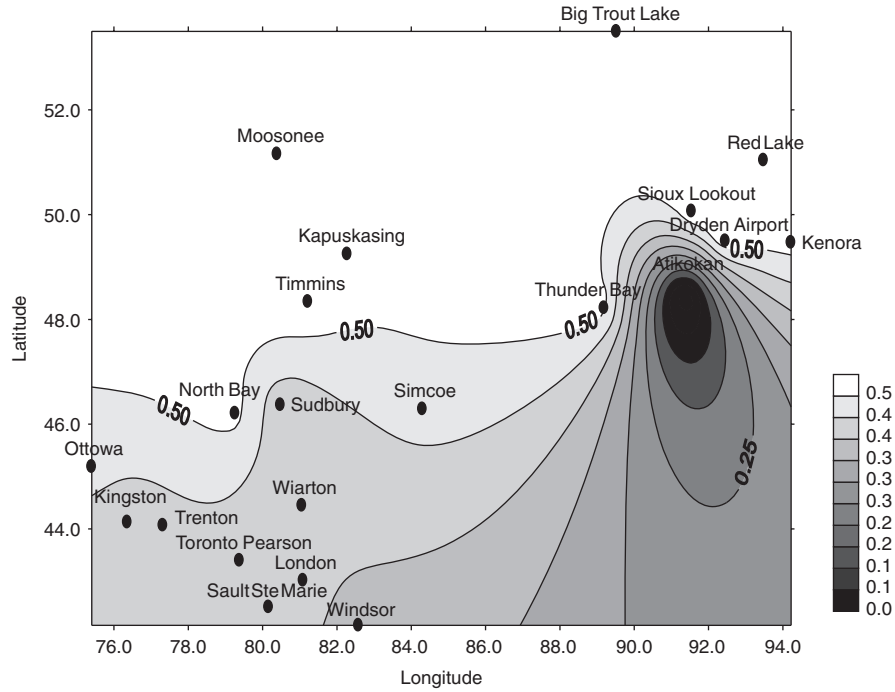

Fig. 10.32b. Energy efficiency map for Ontario for January.

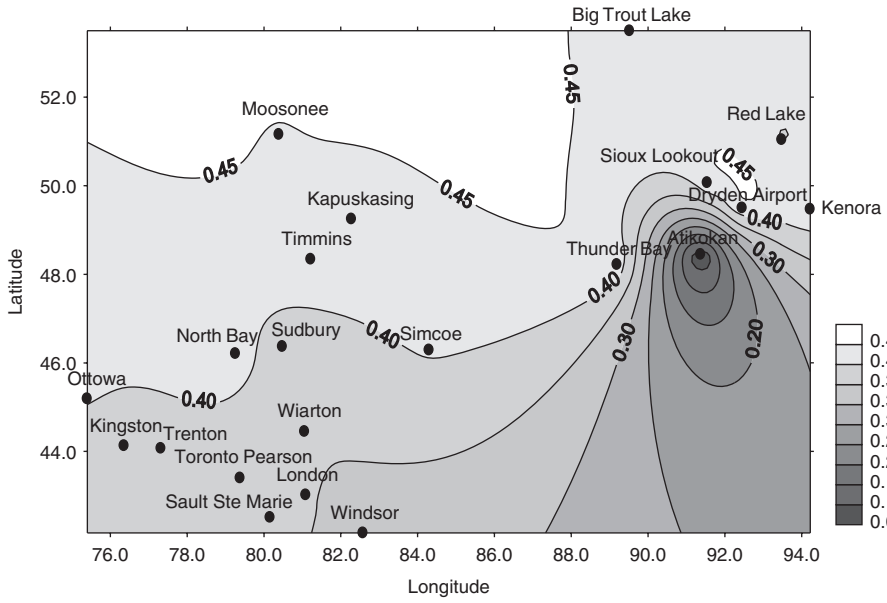

Fig. 10.32c. Exergy efficiency map for Ontario for January.

Using alternate exergy efficiency definitions, efficiencies of wind energy are decreased and two main clusters are seen in April (Fig. 10.33c). In April, the energy and exergy efficiency contours tend to align parallel to lines of constant latitude. In contrast, the relative differences between the two efficiencies are approximately aligned parallel to lines of constant longitude. The relative differences vary between 14% and 22%. In Atikokan, where the lowest wind speeds are observed, the relative difference between the two efficiencies is 22% (Fig. 10.33d).

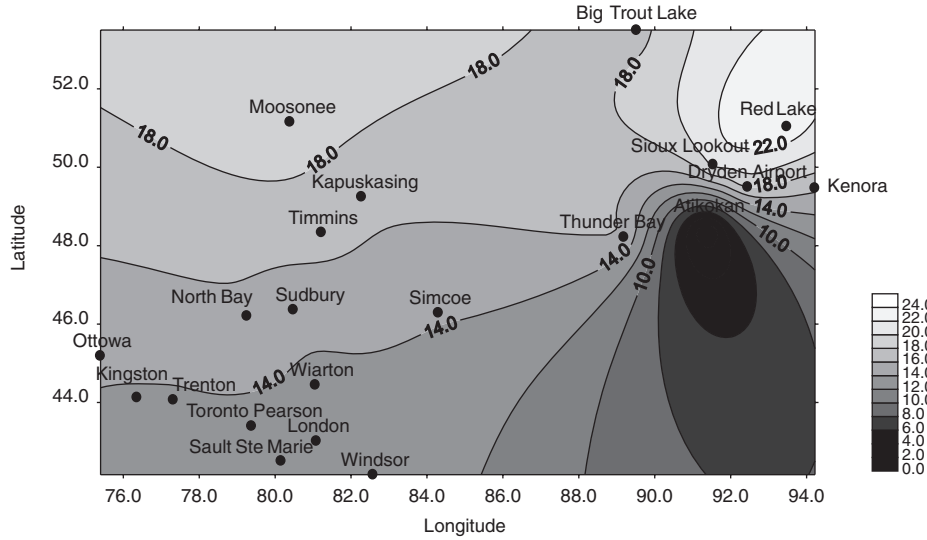

Fig. 10.32d. Map of relative differences (in %) between energy and exergy efficiencies for Ontario for January.

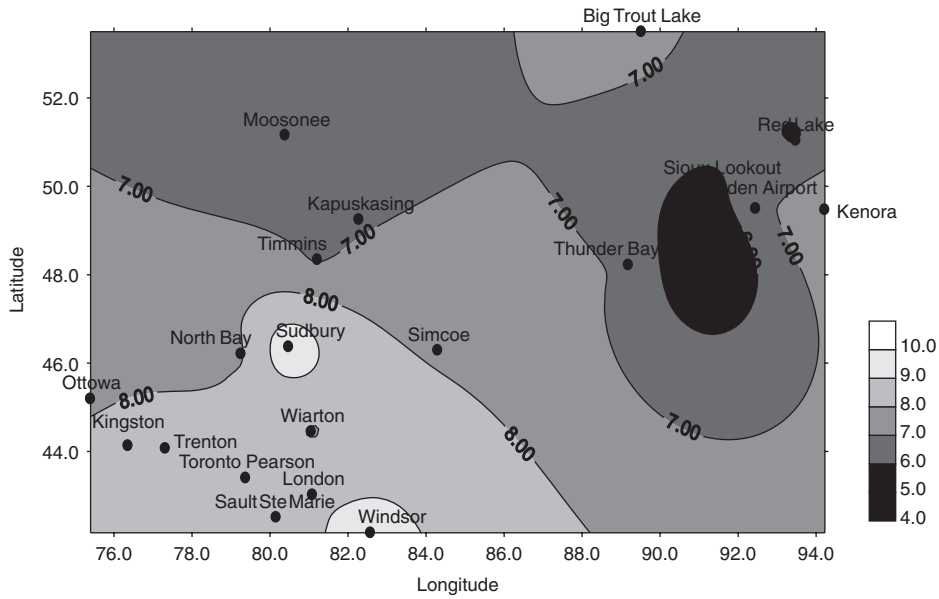

Fig. 10.33a. April wind speed map for 30 m for Ontario.

Wind speeds for July exhibit different clusters as a result of topographical effects in summer. The high heating during this month creates unstable surface conditions. The average wind speed at one station is lower than the cut-in value and as a result the energy and exergy efficiencies are zero. The highest wind speed for this month is the lowest of values for the maximums of the other months (Fig. 10.34a). The spatial distributions for energy efficiencies exhibit three clusters and the general contour values are 40–50% (Fig. 10.34b). There is an area of high energy efficiency in northwest Ontario but exergy efficiencies are lowest in this area. The dominant efficiency in July is seen to be approximately 40%, except for the eastern regions of Ontario (Fig. 10.34c). In July energy and exergy efficiencies are similar and the relative differences between these efficiencies are relatively low (Fig. 10.34d). In July, wind chill is not appreciable.

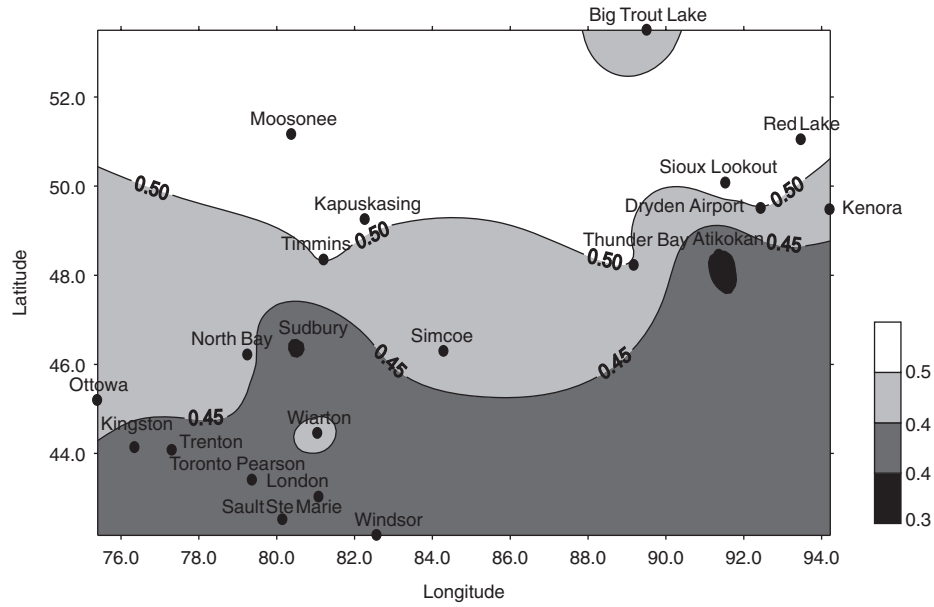

Fig. 10.33b. April energy efficiency map for Ontario.

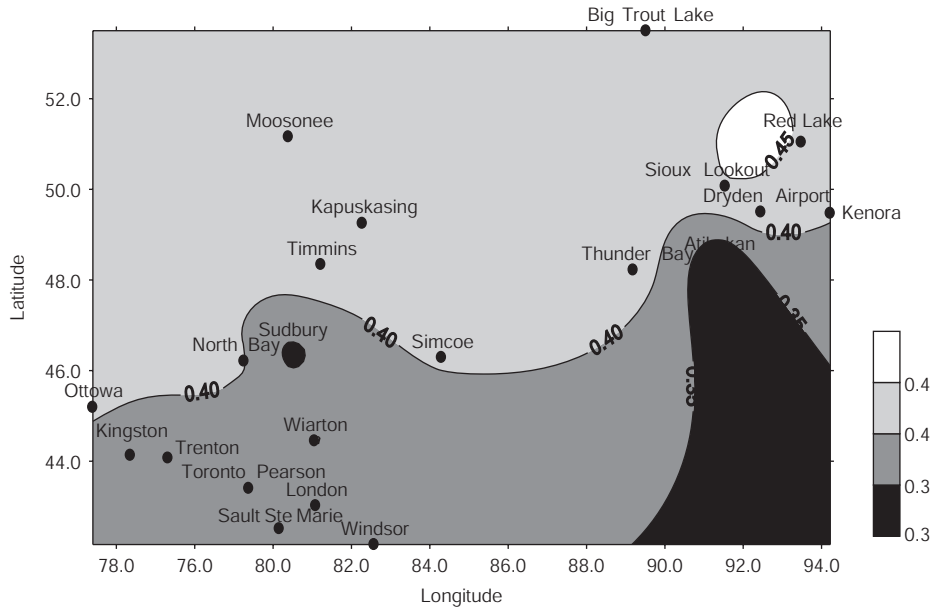

Fig. 10.33c. April exergy efficiency map for Ontario.

For October, three wind speed clusters are observed and wind power systems generate electricity in all stations (Fig. 10.35a). Energy efficiencies are grouped into two main clusters. Topographical conditions cause some localized effects at these stations in October (Fig. 10.35b). Exergy efficiencies are lower than energy efficiencies during this month. It is seen that one of the highest energy efficiency areas, which is observed in western Ontario, is less significant based on exergy (Fig. 10.35c). Without summer topographical heating, the relative differences between these efficiencies are low during October in most parts of Ontario. But wind chill becomes more appreciable during this month (Fig. 10.35d).

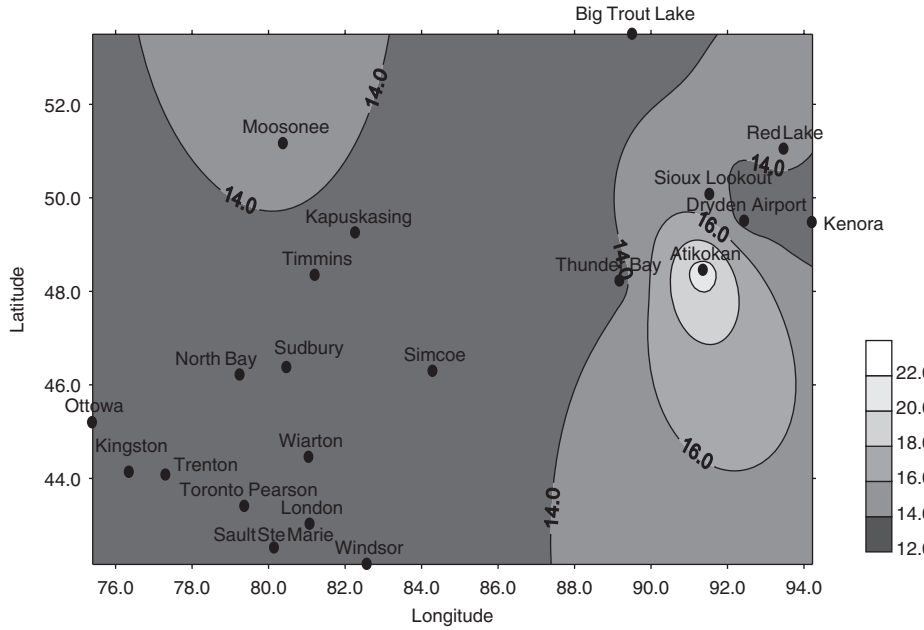

Fig. 10.33d. April energy–exergy relative errors (%) map for Ontario.

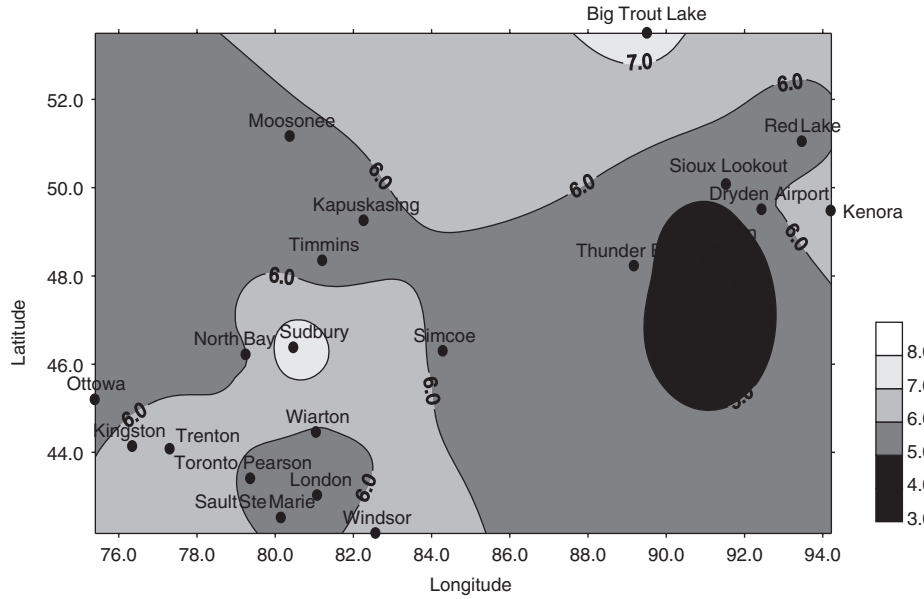

Fig. 10.34a. July wind speed map for 30 m for Ontario.

General comments

The spatio-temporal exergy maps presented here describe energetic and exergetic aspects of wind energy. Seasonal exergy and energy efficiencies are presented in the form of geostatistical maps. The application of exergy analysis for each system, and the ensuing point-by-point map analysis, adds perspective to wind power sources. Thus, exergy maps provide meaningful and useful information regarding efficiency, losses and performance for wind turbines. In addition, the approach reduces the complexity of analyses and facilitates practical analyses and applications.

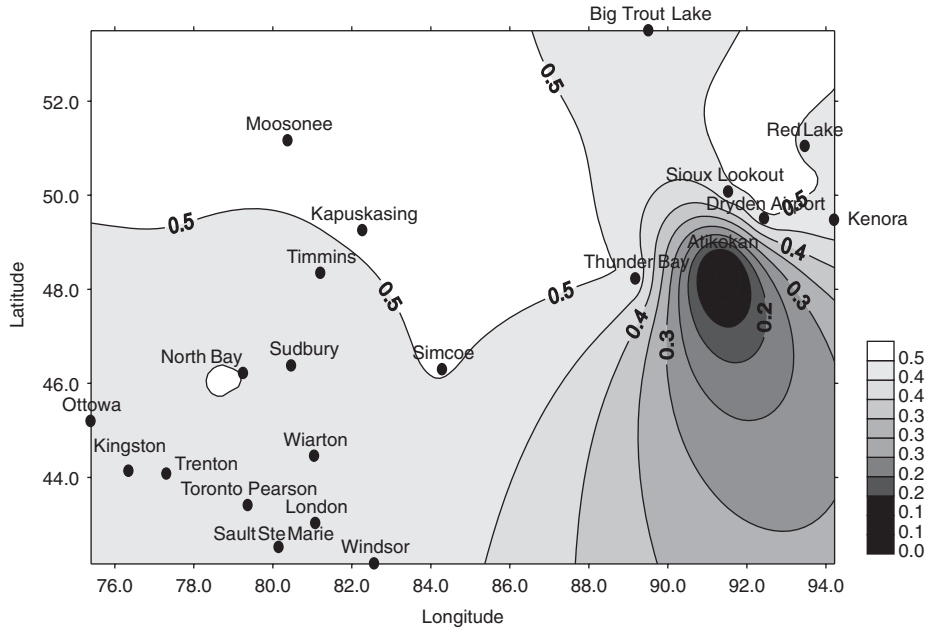

Fig. 10.34b. July energy efficiency map for Ontario.

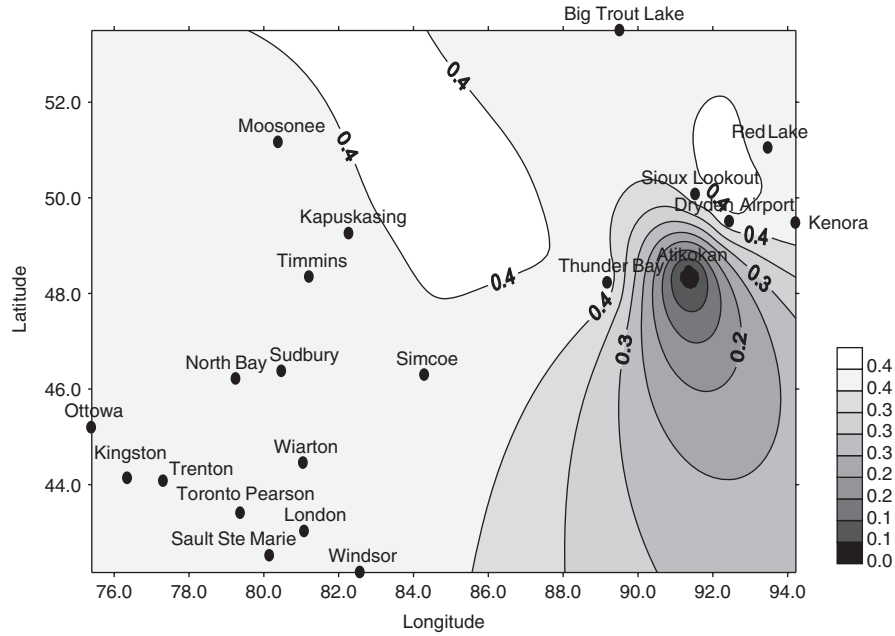

Fig. 10.34c. July exergy efficiency map for Ontario.

Some important observations can be drawn. First, the relative differences between energy and exergy efficiencies are highest in winter and lowest in summer. Second, exergy efficiencies are lower than energy efficiencies for each station for every month considered. More generally, the exergy approach provides useful results for wind energy systems, and the tools for approximating wind energy efficiencies presented here are widely applicable. Such tools can help increase the application of wind systems and optimize designs, and identify appropriate applications and optimal system arrangements.

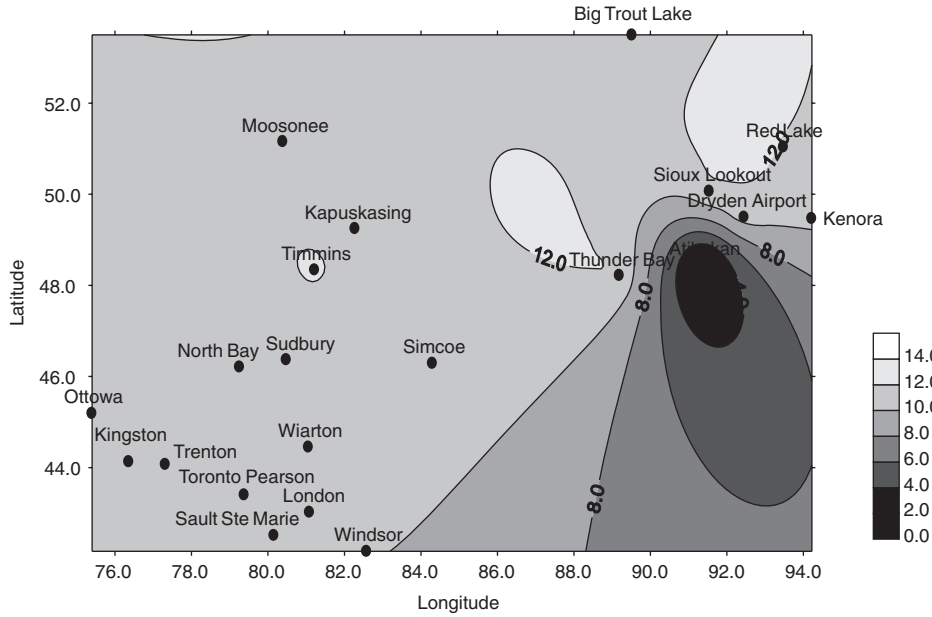

Fig. 10.34d. July energy-exergy relative errors (%) map for Ontario.

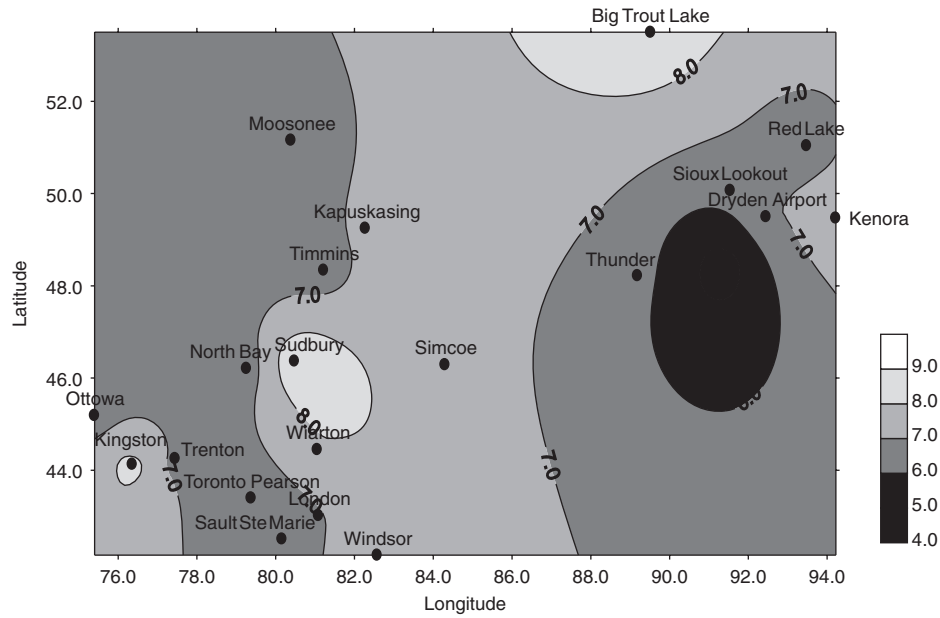

Fig. 10.35a. October wind speed map for 30 m for Ontario.

10.3.5. Closure

Exergy formulations for wind energy are developed and described that are more realistic than energy formulations. Differences are illustrated between energy and exergy efficiencies as a function of wind speed, and can be significant. Exergy analysis should be used for wind energy evaluations and assessments, so as to allow for more realistic modeling, evaluation and planning for wind energy systems. Spatio-temporal wind exergy maps provide a useful tool for assessing wind energy systems.

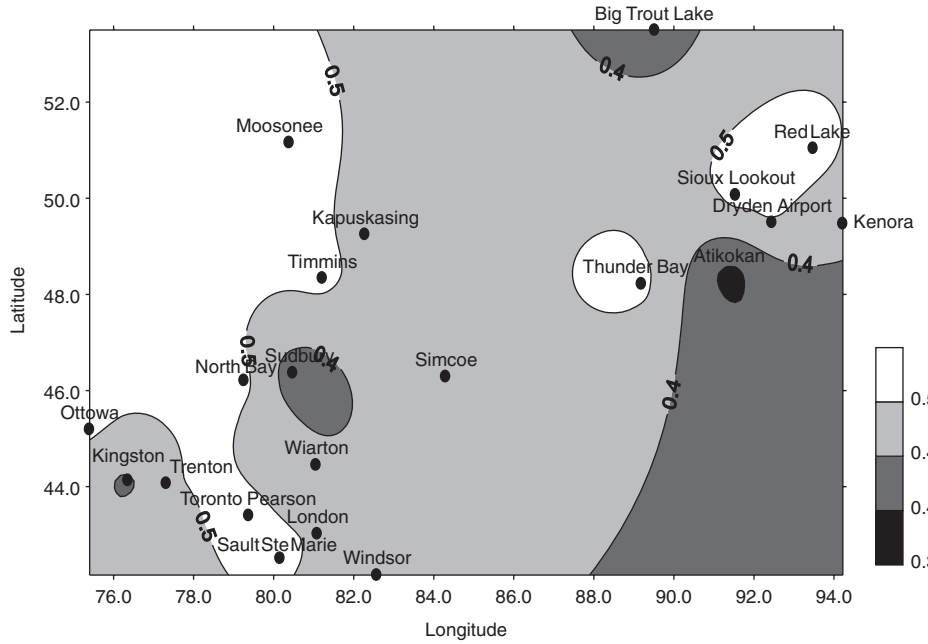

Fig. 10.35b. October energy efficiency map for Ontario.

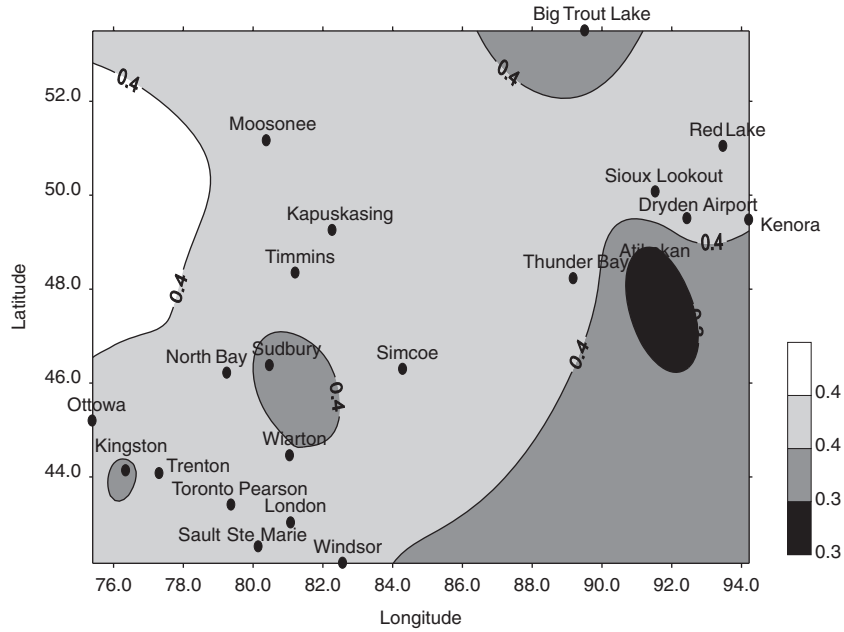

Fig. 10.35c. October exergy efficiency map for Ontario.

10.4. Exergy analysis of geothermal energy systems

The word 'geothermal' derives from the Greek words geo (earth) and therme (heat), and means earth heat. Geothermal energy is the thermal energy within the Earth's crust, i.e., the warm rock and fluid (steam or water containing large amounts of dissolved solids) that fills the pores and fractures within the rock, and flows within sand and gravel. Calculations show that the earth, originating from a completely molten state, would have cooled and become completely solid many

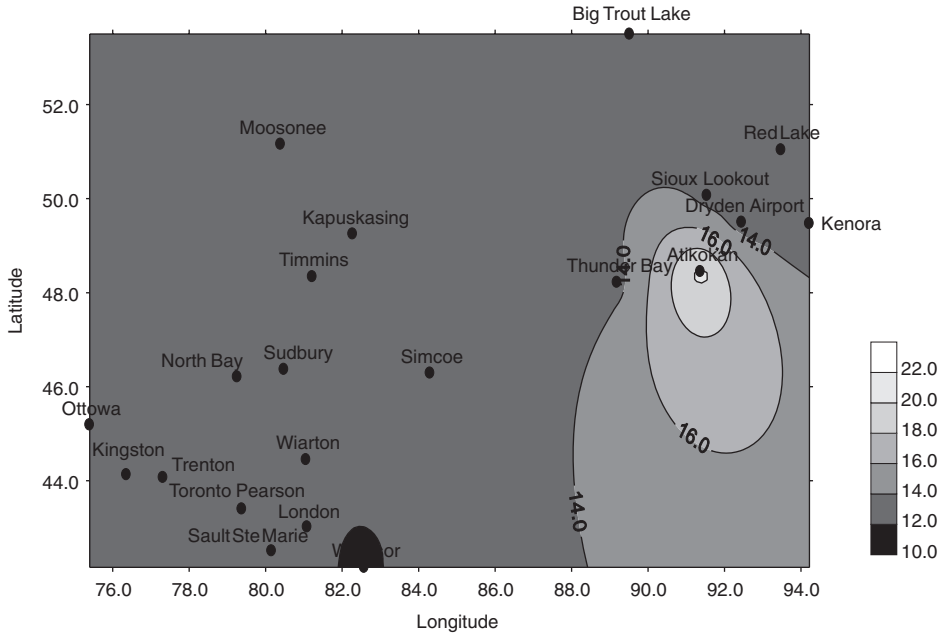

Fig. 10.35d. October energy–exergy relative errors (%) map for Ontario.

thousands of years ago without an energy input in addition to that of the sun. It is believed that the ultimate source of geothermal energy is radioactive decay within the Earth. The origin of this heat is linked with the internal structure of the planet and the physical processes occurring within it.

Geothermal energy is clean and sustainable. Geothermal energy resources are located over a wide range of depths, from shallow ground to hot water and hot rock found several kilometers beneath the Earth's surface, and down even deeper to the extremely high temperatures of molten rock called magma. Geothermal energy is to some extent renewable since a geothermal resource usually has a life of 30–50 years. The life may be prolonged by reinjection processes, which can compensate for at least part of the fluid extracted during geothermal energy use.

Geothermal energy has been used commercially for over 80 years and for four decades on the scale of hundreds of megawatts for electricity generation and direct use. The utilization of geothermal energy has increased rapidly during the last three decades. In 2000, geothermal resources had been identified in over 80 countries and utilized in 58 countries (Fridleifsson, 2001).

Most of the world's geothermal power plants were built in the 1970s and 1980s following the 1973 oil crisis. The urgency to generate electricity from alternative energy sources and the fact that geothermal energy was essentially free led to non-optimal plant designs for using geothermal resources (Kanoglu, 2002a). That era had important consequences for energy and environmental polices. Since then energy policy has been a key tool for sustainable development, given the significant role of energy in economic growth and environmental effects.

There are three general types of geothermal fields: hot water, wet steam and dry steam. Hot water fields contain reservoirs of water with temperatures between 60°C and 100°C, and are most suitable for space heating and agricultural applications. For hot water fields to be commercially viable, they must contain a large amount of water with a temperature of at least 60°C and lie within 2000 m of the surface. Wet steam fields contain water under pressure and are at 100°C. These are the most common commercially exploitable fields. When the water is brought to the surface, some of it flashes into steam, and the steam may drive turbines that produce electrical power. Dry steam fields are geologically similar to wet steam fields, except that superheated steam is extracted from the ground or an aquifer. Dry steam fields are relatively uncommon. Because superheated water explosively transforms to steam when exposed to the atmosphere, it is safer and generally more economic to use geothermal energy to generate electricity, which is more easily transported. Because of the relatively low temperature of the steam/water, geothermal energy is usually converted to electricity with an energy efficiency of 10–15%, as opposed to the 20–40% values typical of coal- or oil-fired electricity generation.

To be commercially viable, geothermal electrical generation plants must be located near a large source of easily accessible geothermal energy. A further complication in the practical utilization of geothermal energy derives from the

corrosive properties of most groundwater and geothermal steam. Prior to 1950, metallurgy was not advanced enough to enable the manufacture of steam turbine blades sufficiently resistant to corrosion for geothermal uses. Geothermal energy sources for space heating and agriculture have been used extensively in Iceland, and to some degree Japan, New Zealand and the former Soviet Union. Other applications include paper manufacturing and water desalination.

Although geothermal energy is generally considered as a non-polluting energy source, water from geothermal fields often contains some amounts of hydrogen sulfide and dissolved metals, making its disposal difficult. Consequently, careful fluid treatment is required, depending on the geothermal characteristics of the location.

Global installed geothermal electrical capacity in the year 2000 was 7974 MW, and overall geothermal electrical generation was 49.3 billion kWh that year. Geothermal energy use for space heating has grown since 1995 by 12%. About 75% of global thermal use of energy production for geothermal sources is for district heating and the reminder for individual space heating (Barbier, 2002). Although the majority of district heating systems are in Europe, particularly in France and Iceland, the U.S. has the highest rate of geothermal energy use for individual home heating systems (e.g., in Klamath Falls, Oregon and Reno, Nevada). Such other countries as China, Japan and Turkey are also using geothermal district heating.

Although such systems are normally assessed with energy, a more perceptive basis of comparison is needed if the true usefulness of a geothermal energy system is to be assessed and a rational basis for the optimization of its economic value established. Energy efficiency ignores energy quality (i.e., exergy) of the working fluid and so cannot provide a measure of ideal performance. Exergy efficiencies provide comprehensive and useful efficiency measures for practical geothermal district heating systems and facilitate rational comparisons of different systems and operating conditions.

In this section, two case studies are provided: (1) energy and exergy analyses of a geothermal district heating system and (2) exergy analysis of a dual-level binary geothermal power plant.

10.4.1. Case study 1: energy and exergy analyses of a geothermal district heating system

In this case study, adapted from Oktay et al. (2007), energy and exergy analyses are carried out of the Bigadic geothermal district heating system (GDHS), including the determination of energy and exergy efficiencies.

The Bigadic geothermal field is located 38 km south of the city of Balikesir which is in the west of Turkey. The Bigadic geothermal field covers a total area of about 1 km^2. The reservoir temperature is at 110°C. As of the end of 2006, there are two wells, HK-2 and HK-3, having depths of 429 and 307 m, respectively. The well head temperature is 98°C. There are five pumps in the geothermal field, three for pumping fluids from the wells and two for pumping fluid to the mechanical room. Wells 1 and 2 are basically artesian wells through which water is forced upward under pressure. Pumps 1 and 2 were in use on the days data were taken, but Pump 3, which is designed to pump automatically when the mass flow rate requirements achieve 100 kg/s, was not in use because the mass flow rate requirements were low. The mass flow rates were 53 and 63.8 kg/s according to actual data for November and December 2006, respectively. Pump 3 generally is not used because the elevation difference between the geothermal source and the mechanical room of 200 m usually provides enough pressure to convey the fluid.

Description of the GDHS

The GDHS consists of three main parts (Fig. 10.36). In the first part, the geothermal fluid is pumped into the 'mud and gas separator unit' to separate harmful particles, and then flows to the first heat exchanger. An 18 km pipeline connects the geothermal source and the mechanical room. Over this distance, the geothermal fluid temperature decreases by 3°C to 4°C.

In the second part of the system, the geothermal fluid is cooled to approximately 44°C in the first and second heat exchangers, which are located in the mechanical room. After heat transfer occurs in the first and second heat exchangers, the geothermal fluid is sent to the first and second center pipelines. A second fluid (clean water) enters the first and second heat exchangers with a temperature of 47°C and is heated to 68°C (based on data from December 6, 2006).

In the third part, clean hot water is pumped into the heat exchangers, which are located under each building. The system is designed to have one or two heat exchangers for each building, one for space heating, and the other for hot water requirements. Presently, each building has one or two heat exchangers. Ten percent of the total residences in Bigadic have an extra heat exchanger for hot water requirements. There are three pipelines for conveying the hot water along different paths. The second and third center pipelines are in use, while the first is not yet in operation.

The second and third center pipelines are designed to transport 15,253 kW of heat to the 2200 individual residences. The indoor and outdoor design temperatures equal 20°C and −6°C, respectively. The second and third center pipelines

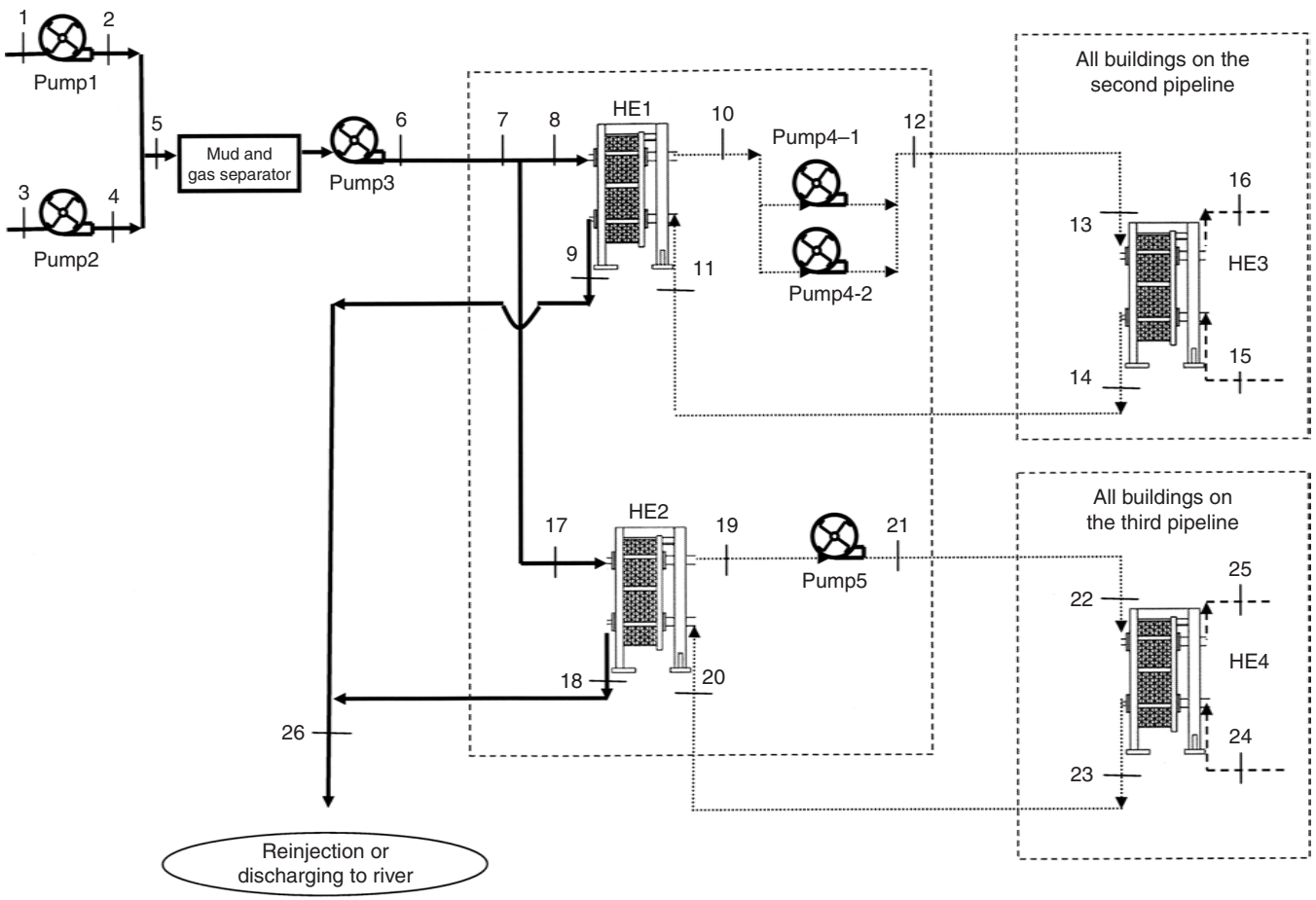

Fig. 10.36. Schematic of the Bigadic GDHS.

supply the heat requirements of the dwellings, one post office, one dormitory, eight colleges, one state hospital, two police stations and ten government buildings.

In the study, the heat exchangers for all residences are modeled as one heat exchanger. All heat from the heat exchangers on the second center pipeline is collected in one heat exchanger, called the 'Third heat exchanger'. Similarly, all heat from the heat exchangers on the third center pipeline is collected in one heat exchanger (the 'Fourth heat exchanger'). The heat is then transferred to the highest elevation and furthest points. The state hospital has both the highest elevation and the longest pipeline distance from the mechanical room and thus is a key point for calculations. Plate-type heat exchangers are used in the system. Inlet and outlet heat exchanger liquid temperatures are investigated for the state hospital.

Analysis

Mass, energy and exergy balances are written for the system and its components, following the treatments of earlier researchers (e.g., Kanoglu, 2002a; Ozgener et al., 2004; Oktay et al., 2007). The system is considered to undergo steady-state and steady-flow processes.

A mass balance for the overall geothermal system can be written as

$$\dot{m}_{\mathrm{T,in}} = \dot{m}_{\mathrm{T,out}} \tag{10.72}$$

where $\dot{m}_{\mathrm{T}}$ denotes the total mass flow rate.

The energy and exergy of the geothermal water are calculated as

$$\dot{E}_{\mathrm{T,in}} = \dot{m}_{\mathrm{tw}} h_{\mathrm{tw}} \cong \dot{m}_{\mathrm{tw},2} h_2 + \dot{m}_{\mathrm{tw},3} h_3 \tag{10.73}$$

$$\dot{E}x_{\mathrm{T,in}} = \dot{m}_{\mathrm{tw},2}[(h_{\mathrm{tw},2} - h_0) - T_0(s_{\mathrm{tw},2} - s_0)] + \dot{m}_{\mathrm{tw},3}[(h_{\mathrm{tw},3} - h_0) - T_0(s_{\mathrm{tw},3} - s_0)] \tag{10.74}$$

where the subscript tw denotes geothermal water and the subscripts 2 and 3 denote the working wells. Similar expressions can be written for the outlet flows of the geothermal water.

The exergy destructions in the heat exchanger, pump, pipeline and overall system are evalulated as follows:

$$\dot{E}x_{\mathrm{d,he}} = \dot{E}x_{\mathrm{in}} - \dot{E}x_{\mathrm{out}} \quad \text{for heat exchangers} \tag{10.75}$$

$$\dot{E}x_{\mathrm{d,pu}} = \dot{W}_{\mathrm{pu}} - (\dot{E}x_{\mathrm{out}} - \dot{E}x_{\mathrm{in}}) \quad \text{for pumps} \tag{10.76}$$

$$\dot{E}x_{\mathrm{d,pi}} = \dot{E}x_{\mathrm{in}} - \dot{E}x_{\mathrm{out}} - \dot{E}x^{\mathrm{Q}} \quad \text{for pipes/pipelines} \tag{10.77}$$

$$\dot{E}x_{\mathrm{T,d}} = \dot{E}x_{\mathrm{T,d,he}} + \dot{E}x_{\mathrm{T,d,pu}} + \dot{E}x_{\mathrm{T,d,pi}} \tag{10.78}$$

The energy efficiency of the system is determined as

$$\eta_{sys} = \frac{\dot{E}_{\mathrm{T,out}}}{\dot{E}_{\mathrm{T,in}}} \tag{10.79}$$

where $\dot{E}_{\mathrm{T,out}}$ is the total product energy output (useful heat) and $\dot{E}_{\mathrm{T,in}}$ is the total energy input.

The exergy efficiency of a heat exchanger is defined as the ratio of the exergy output (i.e., increase in the exergy rate of the cold stream) to the exergy input (i.e., decrease in the exergy rate of the hot stream) as follows:

$$\psi_{\mathrm{he}} = \frac{\dot{m}_{\mathrm{cold}}(ex_{\mathrm{cold,out}} - ex_{\mathrm{cold,in}})}{\dot{m}_{\mathrm{hot}}(ex_{\mathrm{hot,in}} - ex_{\mathrm{hot,out}})} \tag{10.80}$$

where ex is the specific exergy, expressible as

$$ex = (h - h_0) - T_0(s - s_0) \tag{10.81}$$

The exergy efficiency of the system is determined as

$$\psi_{sys} = \frac{\dot{E}x_{\mathrm{T,out}}}{\dot{E}x_{\mathrm{T,in}}} = 1 - \frac{\dot{E}x_{\mathrm{d,sys}} + \dot{E}x_{\mathrm{nd}}}{\dot{E}x_{\mathrm{T,in}}} \tag{10.82}$$

where the subscript nd denotes natural direct discharge.

In addition, we examine the seasonal average total residential heat demand and how it is satisfied. In the 'summer' or warmer season (i.e., when there is no need to heat dwellings), which on average has 165 days, only sanitary hot water is supplied to the residences. The total sanitary hot water load over the summer season is given by

$$\dot{E}_{\mathrm{smr}} = N_{\mathrm{dw}} N_{\mathrm{per}} S \Delta T_{\mathrm{w}}\ c_{\mathrm{f}} \tag{10.83}$$

where N_{dw} is the average number of dwellings, N_{per} is the average number of people in each dwelling (assumed to be 4), S is the average daily usage of sanitary hot water (taken to be 50 L/person-day or 50 kg/person-day), and ΔT_{w} is the temperature difference between the sanitary hot water (60°C) and the tap water from the city distribution network (10°C). Thus,

$$\dot{E}_{\mathrm{smr}} = (2200\ \times 4 \times 50)\,\mathrm{kg/day}(50^{\circ}\mathrm{C})(4.18\,\mathrm{kJ/kg^{\circ}C}) = 1064\ \mathrm{kW}$$

The total 'winter' heat demand (sanitary hot water plus space heating) can be expressed as

$$\dot{E}_{\mathrm{design.}} = \dot{E}_{\mathrm{dw}} N_{\mathrm{dw}} \tag{10.84}$$

where $\dot{E}_{\mathrm{dw}}$ is the heat load for an average (or equivalent) dwelling. Assuming there are 2200 residences, each with a maximum load of 6.9 kW, the overall winter heat load is 15.25 MW.

Equation 10.84 can also be written as

$$\dot{E}_{\mathrm{design}} = \dot{m} c_{\mathrm{f}} \Delta T_{\mathrm{design}} N_{\mathrm{dw}} \tag{10.85}$$

where $\Delta T_{\mathrm{design}} = (T_{\mathrm{indoor}} - T_{\mathrm{outdoor}})_{\mathrm{design}}$ is the difference between the indoor and outdoor temperatures (i.e., $20^{\circ}\mathrm{C} - (-6^{\circ}\mathrm{C}) = 26^{\circ}\mathrm{C}$).

We account for the variation of outdoor temperature through $\Delta T_{\mathrm{average}} = (T_{\mathrm{indoor}} - T_{\mathrm{outdoor}})_{\mathrm{average}}$ using average outdoor temperatures while the indoor temperature is kept constant. We now introduce the temperature ratio

$$T_{\mathrm{R}} = \frac{\Delta T_{\mathrm{average}}}{\Delta T_{\mathrm{design}}} \tag{10.86}$$

in order to determine the average heat loads, as shown below:

$$\dot{E}_{\mathrm{average}} = T_{\mathrm{R}} \dot{E}_{\mathrm{design}} \tag{10.87}$$

The mass flow rate can be determined from above equation as

$$\dot{m} = \frac{\dot{E}_{\mathrm{average}}}{c_{\mathrm{f}} \Delta T} \tag{10.88}$$

Table 10.4 lists the heat demand breakdown for the each month according to the average outdoor temperatures.

Results and discussion

Effect of salts and other components in the geothermal fluid on thermodynamic properties are neglected in this study. The thermodynamic properties of the geothermal fluid are taken to be those of water, properties of which are available from thermodynamic tables and software. Kanoglu (2002a) also employs this assumption in an exergy analysis of geothermal power plants.

Table 10.4. Bigadic GDHS monthly energy requirements.

Month	Average outdoor temperature (°C)	Temperature ratio, T_R	Total average energy demand (kW) (from Eqs. 10.83 and 10.87)
Winter months (from Eq. 10.87)			
October	15.1	0.188	2874.60
November	9.7	0.396	6042.53
December	6.7	0.512	7802.50
January	4.7	0.588	8975.80
February	5.4	0.562	8565.15
March	8.2	0.454	6922.52
April	13.4	0.254	3871.92
Summer months (from Eq. 10.83)			
May	17.7	–	1064.00
June	22.4	–	1064.00
July	24.5	–	1064.00
August	23.6	–	1064.00
September	19.9	–	1064.00

A parametric study of the Bigadic GDHS is presented here using data recorded in November and December 2006. Energy and exergy efficiencies and exergy destructions are determined. For each state of the geothermal fluid and hot water, the temperature, the pressure, the mass flow rate and energy and exergy rates are calculated using Engineering Equation Solver (EES). In Table 10.5 sample results are given based on data for December 2006. State 0 represents the dead state for both the geothermal fluid and hot water. The dead state conditions are taken to be 11°C and 101.3 kPa for the day considered.

An energy flow diagram for the system is illustrated in Fig. 10.37a. The thermal natural direct discharge accounts for 45.62% of the total energy input, while pump and pipeline losses account for 24.15% of the total energy input.

A detailed exergy flow diagram is given in Fig. 10.37b, and shows that 51% (corresponding to about 1468 kW) of the total exergy entering the system is lost, while the remaining 49% is utilized. The highest exergy loss (accounting for 37% of the total exergy entering) occurs from the system pipes. The second largest exergy loss is with the thermal natural direct discharge and amounts to 34% (or about 498.3 kW) of the total exergy input. This is followed by the total exergy destructions associated with the heat exchangers and pumps, which account respectively for 405.5 and 25.81 kW, or 26.3% and 1.7%, of the total exergy input to the system.

The respective energy and exergy efficiencies are found to be 30% and 36% in November and 40% and 49% in December. The reference-environment temperatures are 15.6°C in November and 11°C in December. Some may intuitively feel that having exergy efficiencies greater than energy efficiencies is not correct. In geothermal systems, however, this is common, in part due to the fact that there is a reinjection process which allows recovery of some heat, making the process/system more exergetically efficient. With Fig. 10.37b, this situation can be explained by noting that, although the input energy for the system exceeds the input exergy, the energy losses in the system are greater than the exergy losses. For November and December respectively, the percentage of energy losses are calculated as 70% and 60%, and the percentages of exergy destruction as 64% and 51%.

The energy demand remains constant during the summer months because only hot water for sanitary utilities is used. The energy demand varies during the winter months depending on outlet temperature. In Fig. 10.38a, the energy and exergy demand rates, based on data in Table 10.5, are illustrated and seen to depend on the monthly average outlet (reference) temperature.

Table 10.5. Properties of system fluids and energy and exergy rates at various locations in the Bigadic geothermal district heating system.

State no.	Fluid type	Temperature, T (°C)	Pressure, P (kPa)	Specific enthalpy, h (kJ/kg)	Specific entropy, s (kJ/kg K)	Mass flow rate, $\dot{m}$ (kg/s)	Energy rate, $\dot{E}$ (kW)	Specific exergy, ex (kJ/kg)	Exergy rate, $\dot{E}x$ (kW)
0	TW	11	101.32	46.29	0.166	–	–	–	–
1	TW	97	101.32	406.4	1.273	35	14224.00	45.66	1598.28
2	TW	97.05	404	406.8	1.274	35	14238.00	45.78	1602.34
3	TW	96	101.32	402.2	1.261	28.8	11583.36	44.87	1292.35
4	TW	96.05	404	402.6	1.262	28.8	11594.88	44.99	1295.69
5	TW	96.64	390	405.1	1.268	63.8	25845.38	45.79	2921.10
6	TW	94.5	380	396.1	1.244	63.8	25271.18	43.60	2781.76
7	TW	90	505	377.2	1.192	63.8	24065.36	39.47	2518.13
8	TW	90	505	377.2	1.192	27.15	10240.98	39.47	1071.59
9	TW	47	450	197.2	0.665	27.15	5353.98	9.25	251.16
10	Water	68	152	284.7	0.930	55.55	15815.09	21.29	1182.77
11	Water	47	203	196.9	0.665	55.55	10937.80	8.92	495.64
12	Water	68.06	600	285.3	0.931	55.55	15848.42	21.78	1209.79
13	Water	67.1	253	281	0.919	55.55	15609.55	20.74	1152.35
14	Water	48	152	201.1	0.678	55.55	11171.11	9.43	523.86
15	Water	50	203	209.5	0.704	106.2	22248.90	10.47	1112.42
16	Water	60	182	251.2	0.831	106.2	26677.44	15.99	1698.48
17	TW	90	505	377.2	1.192	36.65	13824.38	39.47	1446.55
18	TW	47	450	197.2	0.665	36.65	7227.38	9.25	339.04
19	Water	68	152	284.7	0.930	75	21352.50	21.29	1596.90
20	Water	47	203	196.9	0.665	75	14767.50	8.92	669.18
21	Water	68.06	600	285.3	0.931	75	21397.50	21.79	1633.38
22	Water	67.1	253	281	0.919	75	21075.00	20.74	1555.83
23	Water	48	152	201.1	0.678	75	15082.50	9.43	707.28
24	Water	50	203	209.5	0.704	143.4	30042.30	10.47	1502.09
25	Water	60	182	251.2	0.831	143.4	36022.08	15.99	2293.42
26	TW	44	400	184.4	0.625	63.8	11764.72	7.58	483.83

Notes: State numbers are shown in Fig. 10.36. State zero represent the reference state. TW denotes thermal water.

Energy and exergy demands are dependent on the reference-environment temperature (e.g., the surroundings temperature). Figure 10.38a is based on average values, when the energy and exergy demands change with outlet temperature. Using this figure, a curve fitting is performed to predict the demands for varied outlet temperatures and the following correlations are obtained:

$$\dot{E} = -1.8543T^4 + 67.761T^3 - 739.89T^2 + 1787.9T + 7679.9$$
$$\dot{E}x = -12.857T^2 - 85.102T + 1609.8$$

where T_0 is the surrounding temperature (in K), which is taken to be the reference-environment temperature. The correlations are plotted with temperatures in Celsius for convenience in practical applications.

We now link the exergy efficiency and average air temperature through the following correlation obtained by curve fitting (Fig. 10.38b):

$$\psi_c = -0.0256T^2 + 0.4038T + 50.372$$

The two cases in Fig. 10.38b are for two actual days in November and December, respectively. Note that the Bigadic GDHS does not have a reinjection section yet, so the geothermal water flows from the mechanical room to the river at 45°C. The exergy of the geothermal water entering the river is 498 kW. The exergy efficiency of the system can be increased by the addition of heat pumps and through recovery and use of the geothermal water that is flowing into the river.

The system is designed to supply the heat loads required for residences at a constant temperature with variable mass flow rates. Figure 10.39 shows both experimental (actual) and calculated exergy destructions within the system components (i.e., pumps, heat exchangers, pipelines and discharge lines), for November and December. It can be observed that: (i) both actual and calculated irreversibilities are reasonably in agreement, except for heat exchangers 1 and 2, and pipelines and (ii) the highest exergy destructions (irreversibilities) occur in pipelines and discharge lines. In those devices, there is a large room for improvement.

Furthermore we can summarize some important facts regarding the environmental benefits of the Bigadic GDHS:

- The maximum heating demand for 2200 dwellings is 15.25 MW and the energy savings achieved with the GDHS in this case amounts to 3876.24 tons of oil equivalent (TOE) per year.
- Emissions of SO_2 and CO_2 are reduced drastically. If such other fuels as coal, natural gas, fuel oil and electricity are used, the respective annual emissions of CO_2 would be 29,996, 10,236, 11,206 and 136,313 tons. Similarly, the respective annual emissions of SO_2 would be 355.49, 53.65 and 3097 tons if coal, fuel oil and electricity are used.

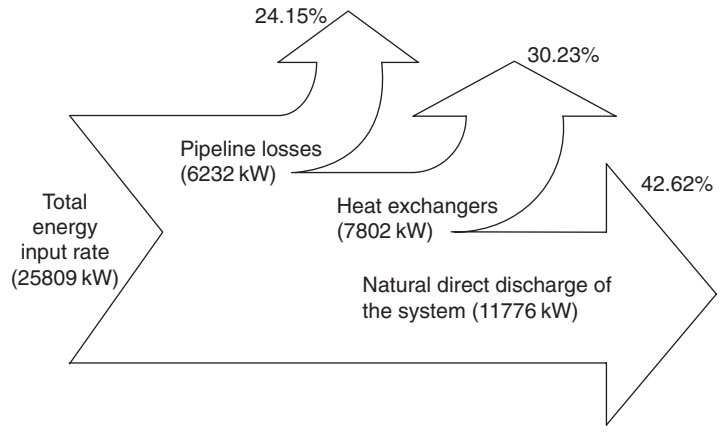

(a)

Fig. 10.37. (a) Energy flow diagram and (b) comprehensive exergy flow diagram of the Bigadic GDHS system. (HE: heat exchanger, BHK: name of well).

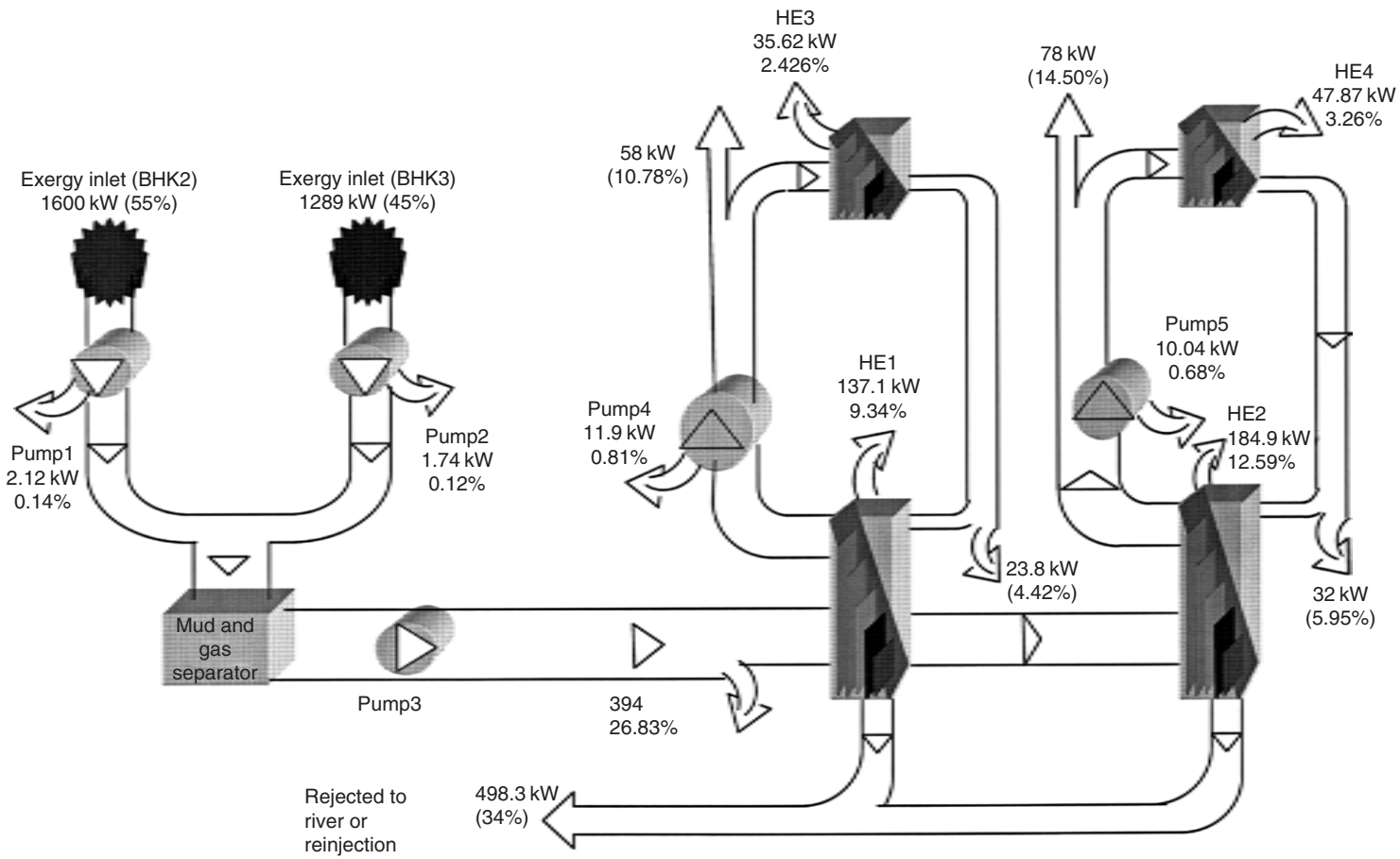

(b)

Fig. 10.37. (Continued)

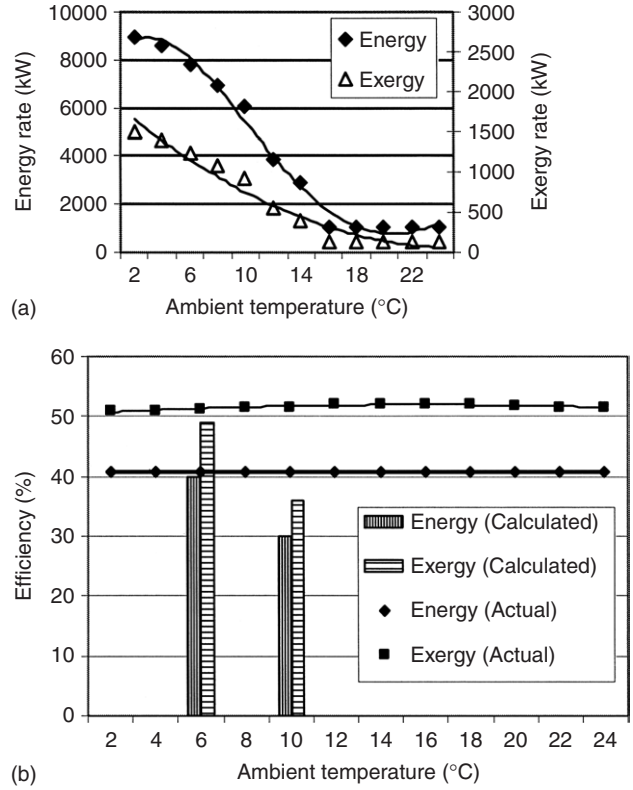

Fig. 10.38. (a) Profiles of energy and exergy rates as a function of ambient temperature, and correlation data. (b) Variation of energy and exergy efficiencies with ambient temperature. (Note: mass flow rates are controlled).

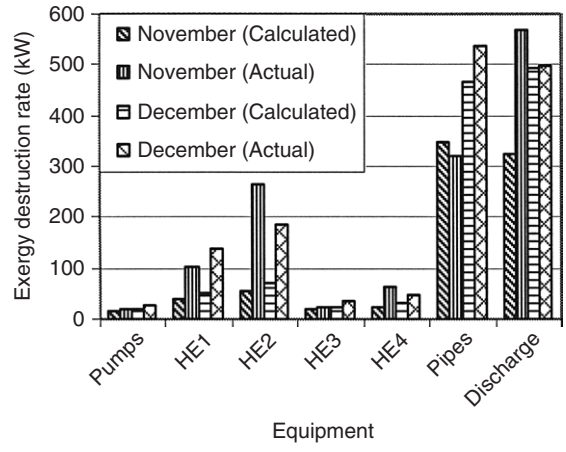

Fig. 10.39. Comparison of the exergy destructions for various components of the system.

Table 10.6 summarizes these results. Note that the emissions values in Table 10.6 are slightly different from those in the previous paragraph. This is because the values in the previous paragraph are the differences between the values listed in table for a given energy form and the geothermal energy values in the table. Using electricity clearly causes the greatest environmental problems and emissions, due to the fact that for each kilowatt of electricity generated the power plants emit about 1 kg of CO_2 and 7 g of SO_2.

Table 10.6. Summary of fuel used for heating and fuel characteristics, and corresponding emissions if the fuel is used.

Heating fuel or energy source	Fuel or energy requirement	Fuel components (%)			Emissions (ton)	
		C	S	Ash	CO_2	SO_2
Domestic coal	12,678,643 kg	67	1.5	9.8	31,090.57	380.36
Natural gas	4,177,738.6 m^3	74.1	–	–	11,330.28	–
Fuel oil	3,926,182.7 kg	85.6	1	0.1	12,300.57	78.52
Electricity for resistance heating	36,422,285 kWh	Assuming a 65% efficient power plant			137,407.27	3121.91
Electricity for a ground-source heat pump	213,331.62 kWh	Assuming a heat pump with COP = 3.8			804.82	18.29
Geothermal energy	290,131 kWh/yr of electricity for pumps				1094.55	24.87

Considering system performance, only 15,253 kW (or 47.92%) of the total capacity of 31,830 kW of the current Bigadic GDHS is used. If the system worked at full capacity, the number of equivalent dwelling served would increase from 2200 to 4593. Then, 8092.54 TOE/year would be saved and, for coal, fuel oil and electric resistance heating, respectively, annual CO_2 emissions would be reduced by 62,631.64, 23,398.13 and 284,621.54 tons, while annual SO_2 emissions would be reduced by 742.26, 112.02 and 6466.54 tons.

Closing comments

The comprehensive case study presented in this section of the GDHS in Balikesir, Turkey leads to the following concluding remarks:

- Using actual thermal data from the Technical Department of the GDHS, the exergy destructions in each component and the overall energy and exergy efficiencies of the system, are evaluated for two reference temperatures (15.6°C for November, case 1, and 11°C for December, case 2).
- Energy and exergy flow diagrams clearly illustrate how much loss occurs as well as inputs and outputs. Average energy and exergy efficiencies are found to be 30% and 36% for case 1, and 40% and 49% for case 2, respectively. The key reason why the exergy efficiencies are higher is that heat recovery is used through the reinjection processes which make use of waste heat.
- The parametric study conducted shows how energy and exergy flows vary with the reference-environment temperature and that the increase in system exergy efficiency is due to the increase in the exergy input potential.

Geothermal district heating appear to be a potential environmentally benign option that can contribute to a country by providing more economic and efficient heating of residences and decreased emission rates.

10.4.2. Case study 2: exergy analysis of a dual-level binary geothermal power plant

An exergy analysis of a stillwater binary design geothermal power plant located in Northern Nevada in the US is performed using plant data taken from (Kanoglu, 2002a). The plant has a unique heat exchange design between the geothermal fluid and the working fluid as explained in the next section. A straightforward procedure for exergy analysis for binary geothermal power plants is described and used to assess plant performance by pinpointing sites of primary exergy destruction and identifying possible improvements.

Plant operation

The geothermal power plant analyzed is a binary design plant with a net electrical generation of 12.4 MW from seven identical paired units. Full power production started in April 1989. The plant operates in a closed loop with no environmental discharge and complete reinjection of the geothermal fluid. The modular power plant operates on a predominantly liquid resource at 163°C. Dry air condensers are utilized to condense the working fluid, so no fresh water is consumed. The geothermal field includes four production wells and three reinjection wells. The working (binary) fluid, isopentane, undergoes a closed cycle based on the Rankine cycle.

The plant is designed to operate with seven paired units of Level I and II energy converters. A plant schematic is given in Fig. 10.40 where only one representative unit is shown. The heat source for the plant is the flow of geothermal water (brine) entering the plant at 163°C with a total mass flow rate of 338.94 kg/s. The geothermal fluid, which remains a liquid throughout the plant, is fed equally to the seven vaporizers of Level I. Therefore, each unit receives 48.42 kg/s of geothermal fluid. The brine exits the Level I vaporizers at approximately 131°C and is fed directly to the paired Level II vaporizers where it is cooled to 100°C. The brine is then divided equally and flows in parallel to the Level I and II preheaters. These preheaters extract heat from the brine, lowering its temperature to 68°C and 65°C, respectively. The brine exiting the preheaters is directed to the reinjection wells where it is reinjected back to the ground.

In Level I, 19.89 kg/s of working fluid circulates through the cycle. The working fluid enters the preheater at 32°C and leaves at about 98°C. It then enters the vaporizer where it is evaporated at 133°C and superheated to 136°C. The working fluid then passes through the turbine and exhausts at about 85°C to an air-cooled condenser where it condenses at a temperature of 31°C. Approximately 530 kg/s of air at an ambient temperature of 13°C is required to absorb the heat

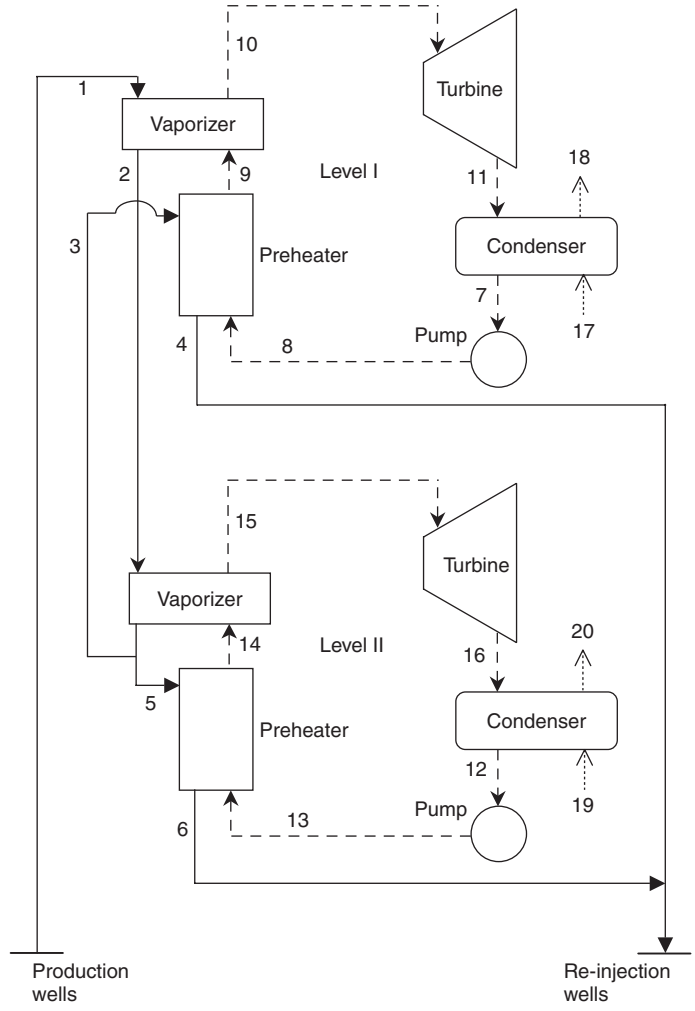

Fig. 10.40. Schematic of the binary geothermal power plant (1 of 7 units).

given up by the working fluid, raising the air temperature to 29°C. The working fluid is pumped to the preheater pressure to complete the Rankine cycle. The Level I isopentane cycle is shown on a T–s diagram in Fig. 10.41.

In Level II, 21.92 kg/s of working fluid cycles through the loop. The working fluid enters the preheater at 27°C and exits at 94°C. It then enters the vaporizer where it is evaporated at 98°C and slightly superheated to 99°C. The working fluid passes through the turbine, and then exhausts to the condenser at about 65°C where it condenses at a temperature of 27°C. Approximately 666 kg/s of air enters the condenser at 13°C and leaves at 26°C. The Level II isopentane cycle is shown on a T–s diagram in Fig. 10.42.

The saturated vapor line of isopentane is seen in Figs. 10.41 and 10.42 to have a positive slope, ensuring a superheated vapor state at the turbine outlet. Thus, no moisture is involved in the turbine operation. This is one reason isopentane is suitable as a working fluid in binary geothermal power plants. Isopentane has other advantageous thermophysical properties such as a relatively low boiling temperature that matches well with the brine in the heat exchange system and a relatively high heat capacity. Isopentane is also safe to handle, non-corrosive and non-poisonous.

The heat exchange process between the geothermal brine and isopentane is shown on a T–s diagram in Figs. 10.43 and 10.44 for Levels I and II, respectively. An energy balance can be written for part of the heat exchange taking place in the vaporizer of Level I using state points shown in Fig. 10.43 as

$$\dot{m}_1(h_{pp} - h_2) = \dot{m}_9(h_f - h_9) \tag{10.89}$$

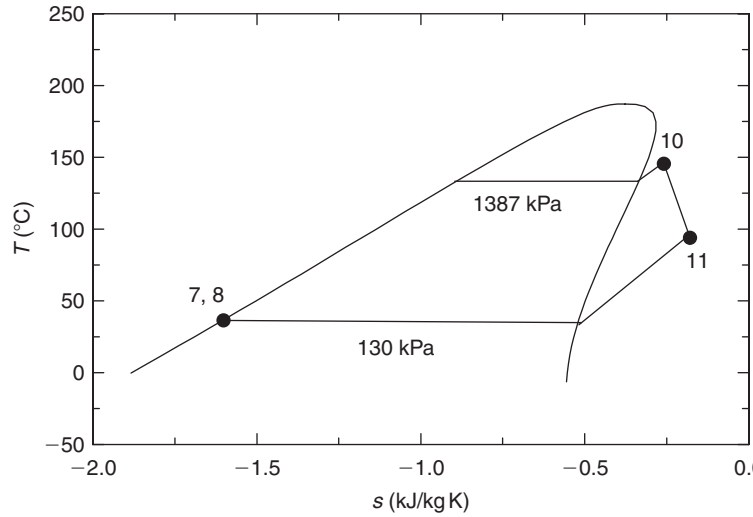

Fig. 10.41. Temperature–entropy (T–s) diagram of Level I isopentane cycle.

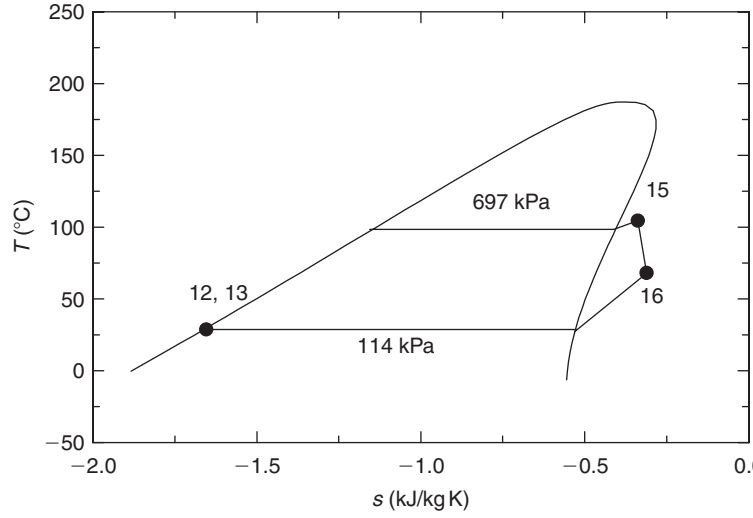

Fig. 10.42. Temperature–entropy (T–s) diagram of Level II isopentane cycle.

where h_f is the saturated liquid enthalpy of isopentane at the saturation (i.e. vaporization) temperature, 133.1°C, and the h_{pp} is the enthalpy of brine at the pinch-point temperature of the brine. Solving this equation for h_{pp}, we determine the corresponding brine pinch-point temperature T_{pp} to be 140.5°C. The pinch-point temperature difference ΔT_{pp} is the difference between the brine pinch-point temperature and the vaporization temperature of isopentane. Here, $\Delta T_{pp} = 7.4$°C. A similar energy balance for the vaporizer of Level II can be written using state points shown in Fig. 10.44 as

$$\dot{m}_2(h_{pp} - h_3) = \dot{m}_{14}(h_f - h_{14}) \tag{10.90}$$

Here, the brine pinch-point temperature is 101.3°C, the vaporization temperature in Level II is 98.4°C and the pinch-point temperature difference ΔT_{pp} is 2.9°C.

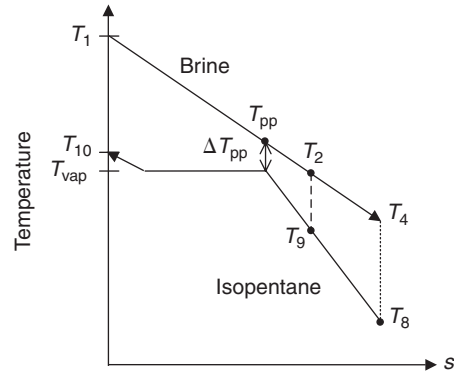

Fig. 10.43. Heat exchange process between the geothermal brine and the isopentane working fluid in Level I.

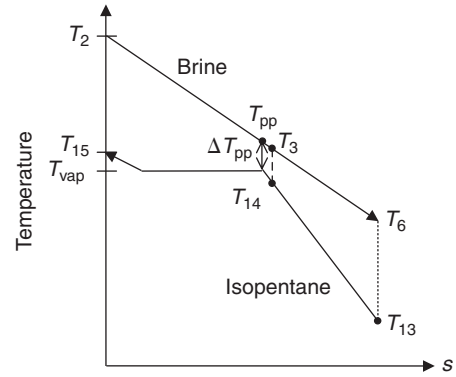

Fig. 10.44. Heat exchange process between the geothermal brine and the isopentane working fluid in Level II.

The turbine power outputs are 1271 kW in Level I and 965 kW in Level II, while the power requirements for the circulation pumps of Level I and II are 52 and 25 kWe, respectively. The net power outputs from Level I and II Rankine cycles are thus 1219 and 940 kW, respectively, giving a net power output of the combined Level I and II cycles of 2159 kW. It is estimated by plant management that approximately 200 and 190 kW power are consumed by parasitic uses in the units in Level I and II, respectively. These parasitic uses correspond to 18.1% of the net power generated in the cycle, and include fan power for the condenser and auxiliaries. There are six fans in Level I and nine in Level II. Subtracting the parasitic power from the net power generated in the cycle yields a net power output from one unit 1769 kW. Since the plant has seven identical units, the total net power output for this plant is 12,383 kW. The various power terms discussed in this section are listed in Table 10.7.

Exergy analysis

Neglecting kinetic and potential energy changes, the specific flow exergy of the geothermal fluid at any state (plant location) can be calculated from

$$ex = h - h_0 - T_0(s - s_0) \tag{10.91}$$

where h and s are the specific enthalpy and entropy of the geothermal fluid at the specified state, and h_0 and s_0 are the corresponding properties at the restricted dead state. For a mass flow rate $\dot{m}$, the exergy flow rate of the geothermal fluid

Table 10.7. Exergy rates and other properties at various plant locations for a representative unit.

State no.	Fluid	Phase	Temperature, T (°C)	Pressure, P (bar abs)	Specific enthalpy, h (kJ/kg)	Specific entropy, s (kJ/kg °C)	Mass flow rate, $\dot{m}$ (kg/s)	Specific exergy, ex (kJ/kg)	Exergy rate, $\dot{E}x$ (kW)
0	Brine	Dead state	12.8	0.84	53.79	0.192	–	0	–
0′	Isopentane	Dead state	12.8	0.84	−377.30	−1.783	–	0	–
1	Brine	Liquid	162.8	–	687.84	1.971	48.42	125.43	6073
2	Brine	Liquid	130.7	–	549.40	1.642	48.42	81.01	3923
3	Brine	Liquid	99.9	–	418.64	1.306	24.21	46.42	1124
4	Brine	Liquid	67.8	–	283.80	0.928	24.21	19.59	474
5	Brine	Liquid	99.9	–	418.64	1.306	24.21	46.42	1124
6	Brine	Liquid	64.5	–	269.98	0.887	24.21	17.41	422
7	Isopentane	Liquid	31.0	1.30	−336.35	−1.645	19.89	1.33	27
8	Isopentane	Liquid	31.7	13.87	−333.73	−1.643	19.89	3.43	68
9	Isopentane	Liquid	97.6	13.87	−169.69	−1.157	19.89	28.55	568
10	Isopentane	Superheated vapor	136.0	13.87	167.50	−0.316	19.89	125.13	2489
11	Isopentane	Superheated vapor	85.2	1.30	103.50	−0.241	19.89	39.75	791
12	Isopentane	Liquid	26.9	1.14	−345.72	−1.676	21.92	0.80	18
13	Isopentane	Liquid	27.2	6.97	−344.56	−1.675	21.92	1.77	39
14	Isopentane	Liquid	93.7	6.97	−180.35	−1.183	21.92	25.15	551
15	Isopentane	Superheated vapor	98.7	6.97	108.48	−0.405	21.92	91.64	2009
16	Isopentane	Superheated vapor	64.6	1.14	64.50	−0.338	21.92	28.60	627
17	Air	Gas	12.8	0.84	286.29	5.703	529.87	0	0
18	Air	Gas	29.2	0.84	302.80	5.759	529.87	0.46	242
19	Air	Gas	12.8	0.84	286.29	5.703	666.53	0	0
20	Air	Gas	26.2	0.84	299.78	5.749	666.53	0.31	167

can be written as

$$\dot{E}x = \dot{m}(ex) \tag{10.92}$$

Data for the geothermal fluid, the working fluid and air, including temperature, pressure, mass flow rate, specific exergy and exergy rate, are given In Table 10.7 following the state numbers specified in Fig. 10.40. States 0 and 0′ refer to the restricted dead states for the geothermal and working fluids, respectively. They correspond to an environment temperature of 12.8°C and an atmospheric pressure of 84 kPa, which are the values when the plant data were obtained. Properties of water are used for the geothermal fluid, so the effects of salts and non-condensable gases that might present in the geothermal brine are neglected. This simplification does not introduce significant errors in calculations since the fractions of salts and non-condensable gases are estimated by the plant managers to be small. Properties for the working fluid, isopentane, are obtained from thermodynamic property evaluation software (Friend, 1992).

The preheaters, vaporizers and condensers in the plant are essentially heat exchangers designed to perform different tasks. The exergy efficiency of a heat exchanger may be measured as the exergy increase of the cold stream divided by the exergy decrease of the hot stream (Wark, 1995). Applying this definition to the Level I vaporizer, we obtain

$$\psi_{\text{vap I}} = \frac{\dot{E}x_{10} - \dot{E}x_9}{\dot{E}x_1 - \dot{E}x_2} \tag{10.93}$$

where the exergy rates are given in Table 10.7. The difference between the numerator and denominator in Eq. (10.93) is the exergy destruction rate in the heat exchanger. That is,

$$\dot{I}_{\text{vap I}} = (\dot{E}x_1 - \dot{E}x_2) - (\dot{E}x_{10} - \dot{E}x_9) \tag{10.94}$$

Because of the complicated nature of the entire heat exchange system, the exergy efficiency and exergy destruction for the Level I vaporizer–preheater system are considered:

$$\psi_{\text{vap–pre I}} = \frac{\dot{E}x_{10} - \dot{E}x_8}{(\dot{E}x_1 - \dot{E}x_2) + (\dot{E}x_3 - \dot{E}x_4)} \tag{10.95}$$

$$\dot{I}_{\text{vap–pre I}} = (\dot{E}x_1 + \dot{E}x_3 + \dot{E}x_8) - (\dot{E}x_2 + \dot{E}x_4 + \dot{E}x_{10}) \tag{10.96}$$

The exergy efficiency of the condenser is calculated similarly. However, the exergy destruction in the condenser is approximated as the exergy decrease in exergy of isopentane across the condenser. That is, the exergy increase of the air, which is small, is neglected.

The exergy efficiency of a turbine measures of how efficiently the flow exergy of the fluid passing through it is converted to work, and can be expressed for the Level I turbine as

$$\psi_{\text{turb I}} = \frac{\dot{W}_{\text{turb I}}}{\dot{E}x_{10} - \dot{E}x_{11}} \tag{10.97}$$

The difference between the numerator and denominator in Eq. (10.97) is the exergy destruction rate in the turbine:

$$\dot{I}_{\text{turb I}} = (\dot{E}x_{10} - \dot{E}x_{11}) - \dot{W}_{\text{turb I}} \tag{10.98}$$

Analogously, the exergy efficiency and exergy destruction rate for the Level I pump can be written as

$$\psi_{\text{pump I}} = \frac{\dot{E}x_8 - \dot{E}x_7}{\dot{W}_{\text{pump I}}} \tag{10.99}$$

$$\dot{I}_{\text{pump I}} = \dot{W}_{\text{pump I}} - (\dot{E}x_8 - \dot{E}x_7) \tag{10.100}$$

Data on heat and pressure losses in pipes and valves are not available and are therefore neglected, but their effects are minor.

The exergy efficiency of the Level I isopentane cycle can be determined as

$$\psi_{\text{level I}} = \frac{\dot{W}_{\text{net I}}}{(\dot{E}x_1 - \dot{E}x_2) + (\dot{E}x_3 - \dot{E}x_4)} \tag{10.101}$$

where the denominator represents the decrease in brine exergy flow rate across the Level I vaporizer–preheater (i.e., exergy input rate to Level I). The net power of Level I is the difference between the turbine power output and the pump power input. The total exergy loss rate for the Level I cycle is approximately the exergy destruction rate, expressible as:

$$\dot{I}_{\text{level I}} = \dot{I}_{\text{pump I}} + \dot{I}_{\text{vap I}} + \dot{I}_{\text{pre I}} + \dot{I}_{\text{turb I}} + \dot{I}_{\text{cond I}} \tag{10.102}$$

The exergy efficiency of the binary geothermal power plant based on the total brine exergy flow rate decreases across the vaporizer–preheater systems of the Level I and II cycles (i.e., total exergy input rates to the Level I and II cycles) can be expressed as

$$\psi_{\text{plant,a}} = \frac{\dot{W}_{\text{net plant}}}{[(\dot{E}x_1 - \dot{E}x_2) + (\dot{E}x_3 - \dot{E}x_4)] + [(\dot{E}x_2 - \dot{E}x_3 - \dot{E}x_5) + (\dot{E}x_5 - \dot{E}x_6)]} \tag{10.103}$$

where the numerator represents the net power output from the plant, obtained by subtracting the total parasitic power, 390 kW, from the total net power output from the Level I and II cycles, 2159 kW.

The exergy efficiency of the plant can alternatively be calculated based on the brine exergy input rate to the plant (i.e. exergy rate of the brine at the Level I vaporizer inlet). That is,

$$\psi_{\text{plant,b}} = \frac{\dot{W}_{\text{net plant}}}{\dot{E}x_1} \tag{10.104}$$

When using Eq. (10.104), the exergy input rate to the plant is sometimes taken as the exergy of the geothermal fluid in the reservoir. Those who prefer this approach argue that realistic and meaningful comparisons between geothermal power plants require that the methods of harvesting the geothermal fluid be considered. Others argue that taking the reservoir as the input is not proper for geothermal power plants since conventional power plants are evaluated on the basis of the exergy of the fuel burned at the plant site (DiPippo and Marcille, 1984).

The total exergy destruction rate in the plant can be written as the difference between the brine exergy flow rate at the vaporizer inlet and the net power outputs from the Level I and Level II cycles:

$$\dot{I}_{\text{plant}} = \dot{E}x_1 - (\dot{W}_{\text{net I}} + \dot{W}_{\text{net II}}) \tag{10.105}$$

This expression accounts for the exergy losses in plant components and the exergy of the brine exiting the Level I and Level II preheaters. Here, the used brine is considered lost since it is reinjected back into the ground without attempting to use it. Some argue that the exergy of used brine is 'recovered' by returning it to the reservoir and so should not be counted as part of the exergy loss.

The exergy efficiencies and exergy destruction rates of the major plant components and the overall plant are listed in Table 10.8 for one representative unit. To pinpoint the main sites of exergy destruction and better compare the losses, an exergy flow diagram is given in Fig. 10.45.

Energy analysis

For comparison, selected energy data are provided in Table 10.8, including heat-transfer rates for vaporizers, preheaters and condensers and work rates for turbines, pumps, the Level I and II cycles, and the overall plant. Also, isentropic

Table 10.8. Selected exergy and energy data for a representative unit of the plant.[a]

Component	Exergy destruction rate (kW)	Exergy efficiency (%)	Heat transfer or work rate (kW)	Isentropic or energy efficiency (%)[b]
Vaporizer I	229.5	89.3	6703	–
Preheater I	149.9	76.9	3264	–
Vaporizer II	217.6	87.0	6331	–
Preheater II	189.5	73.0	3599	–
Preheater–vaporizer I	379.4	86.5	9967	–
Preheater–vaporizer II	407.2	82.9	9930	–
Condenser I	764	31.6	8748	–
Condenser II	610	27.4	8992	–
Turbine I	427.2	74.9	1271	70.8
Turbine II	416.9	69.8	965	66.6
Pump I	10.3	80.2	52	80.0
Pump II	4.4	82.9	25	80.0
Level I cycle	1339	43.5	1219	12.2
Level II cycle	1271	39.5	940	9.5
Level I–II cycle	2610	41.7	2159	10.9
Overall plant[c]	2610	34.2	1769	8.9
Overall plant[d]	2610	29.1	1769	5.8

[a] I and II denote that the component belongs to Level I or II, respectively.
[b] Values for turbines and pumps are isentropic efficiencies and for the Level I and II cycles and the overall plant are energy efficiencies.
[c] Based on the exergy (or energy) input to isopentane cycles.
[d] Based on the exergy (or energy) input to the plant.

efficiencies of the turbines and pumps and energy efficiencies of the Level I and II cycles and the overall plant are given. The energy efficiency of the Level I cycle is calculated as the ratio of the net power output from the Level I cycle to the heat input rate to the Level I cycle (i.e., the total heat-transfer rate in the Level I vaporizer–preheater). The energy efficiency of the plant based on the energy input rate to the plant is expressed here as

$$\eta_{\text{plant,a}} = \frac{\dot{W}_{\text{net plant}}}{\dot{m}_1(h_1 - h_2) + \dot{m}_3(h_3 - h_4) + \dot{m}_2(h_2 - h_5) + \dot{m}_5(h_5 - h_6)} \tag{10.106}$$

where the terms in the denominator represent the heat-transfer rates in vaporizer I, preheater I, vaporizer II and preheater II, respectively. An alternative plant energy efficiency is

$$\eta_{\text{plant,b}} = \frac{\dot{W}_{\text{net plant}}}{\dot{m}_1(h_1 - h_0)} \tag{10.107}$$

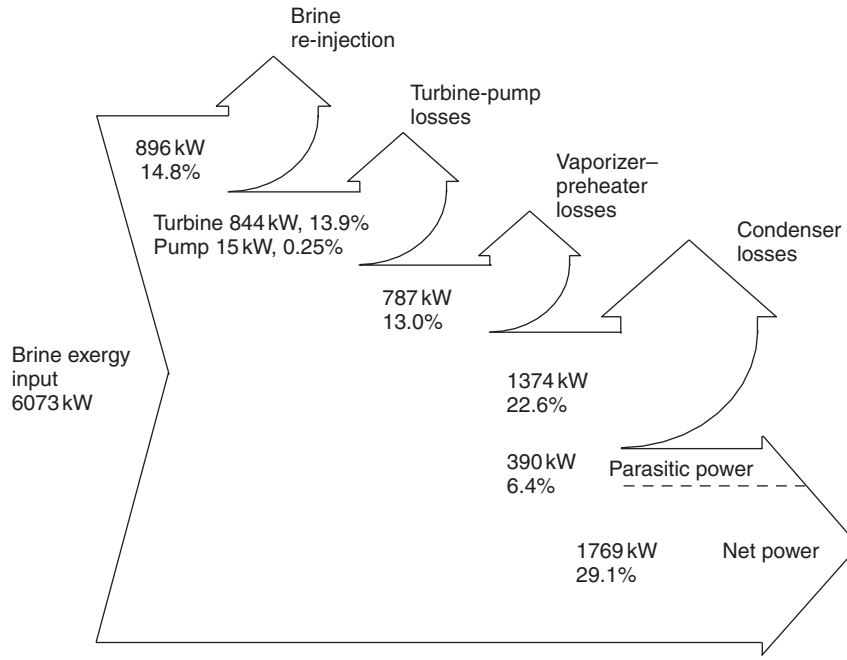

Fig. 10.45. Exergy flow diagram for the binary geothermal power plant. Percentages are based on brine exergy input.

where h_0 is the dead state specific enthalpy of the brine specified in Table 10.7. Here, the denominator represents the energy rate of the brine at the Level I vaporizer inlet.

An energy flow diagram is given in Fig. 10.46 to provide a comparison to the exergy flow diagram.

Discussion

The exergy flow diagram given in Fig. 10.45 shows that 64.5% of the exergy entering the plant is lost. The remaining 35.5% is converted to power, 18.1% of which is used for parasitic loads in the plant. The exergy efficiency of the plant is 34.2% based on the exergy input to the isopentane Rankine cycles (i.e., the exergy decreases in the brine in the vaporizer and preheater) and 29.1% based on the exergy input to the plant (i.e., the brine exergy at the Level I vaporizer inlet) (Table 10.8).

Bodvarsson and Eggers (1972) report exergy efficiencies of single- and double-flash cycles to be 38.7% and 49.0%, respectively, based on a 250°C resource water temperature and a 40°C sink temperature. Both values are significantly greater than the exergy efficiency calculated for the binary plant analyzed here. This is expected since additional exergy destruction occurs during heat exchange between the geothermal and working fluids in binary plants. DiPippo and Marcille (1984) calculate the exergy efficiency of an actual binary power plant using a 140°C resource and a 10°C sink to be 20% and 33.5% based on the exergy input to the plant and to the Rankine cycle, respectively. Kanoglu and Cengel (1999) report exergy efficiencies of 22.6% and 34.8% based on the exergy input to the plant and to the Rankine cycle, respectively, for a binary geothermal power plant with a 158°C resource and 3°C sink.

Because they use low-temperature resources, geothermal power plants generally have low energy efficiencies. Here, the plant energy efficiency is 5.8% based on the energy input to the plant and 8.9% based on energy input to the isopentane Rankine cycles. This means that more than 90% of the energy of the brine is discarded as waste.

The results suggest that geothermal resources are best used for direct heating applications instead of power generation when economically feasible. For power generation systems where used brine is reinjected back to the ground at a relatively high temperature, cogeneration in conjunction with district heating may be advantageous. The energy flow diagram in Fig. 10.46 shows that 35.2% of the brine energy is reinjected, 57.8% is rejected in the condenser, and the remainder

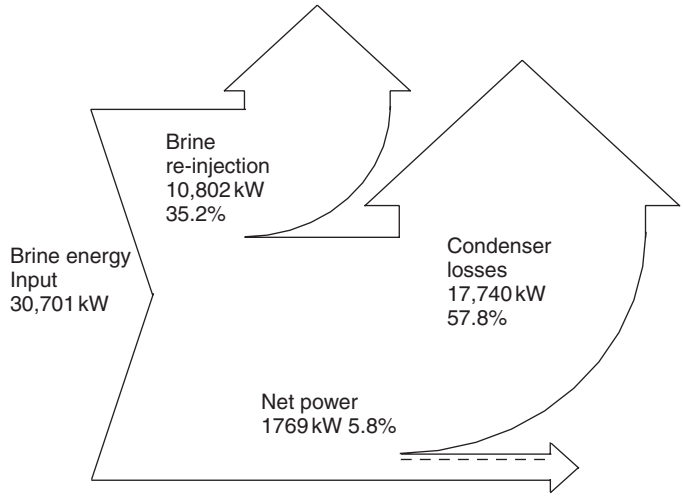

Fig. 10.46. Energy flow diagram for the binary geothermal power plant. Percentages are based on brine energy input.

is converted to power. These data provide little information on how the performance can be improved, highlighting the value of exergy analysis.

The primary exergy losses in the plant are associated with vaporizer–preheater losses, turbine-pump losses, brine reinjection and condenser losses, which represent 13.0%, 13.9%, 14.8% and 22.6% of the brine exergy input, respectively (Fig. 10.45). The exergy efficiencies of the Level I and II vaporizer–preheaters are 87% and 83%, respectively. These values are high, indicating efficient heat exchange operations. In binary geothermal power plants, heat exchangers are important components and their individual performances affect considerably overall plant performance. The exergy efficiency of the vaporizer is significantly greater than that of the preheater, mainly because the average temperature difference between the brine and the working fluid is smaller in the vaporizer than in the preheater.

The exergy efficiencies of the turbines in Levels I and II are 75% and 70%, respectively. These efficiencies indicate that the performance of the turbines can be somewhat improved. This observation is confirmed by the relatively low turbine isentropic efficiencies (in the range of 65–70%) listed in Table 10.8. That a reasonable margin for improvement exists can be seen by considering a recently built binary geothermal power plant, which has a turbine with an exergy efficiency of over 80% (Kanoglu et al., 1998). The pumps seem to be performing efficiently.

The exergy efficiencies of the condensers are in the range of 30%, making them the least efficient components in the plant. This is primarily due to the high average temperature difference between the isopentane and the cooling air. The brine is reinjected back to the ground at about 65°C. In at least one binary plant using a resource at about 160°C, the brine is reinjected at temperatures above 90°C (Kanoglu et al., 1998). Compared to this, the percent exergy loss associated with the brine reinjection is low in this plant. It is noted that condenser efficiencies are often difficult to define and interpret since the objective of a condenser is to reject heat rather than create a product.

For binary geothermal power plants using air as the cooling medium, the condenser temperature varies with the ambient air temperature, which fluctuates throughout the year and even through the day. As a result, power output decreases by up to 50% from winter to summer (Kanoglu and Cengel, 1999). Consequently, the exergy destruction rates and percentages vary temporally as well as spatially, this effect being most noticeable in the condenser.

10.5. Closing remarks

Exergy analysis is usually used to determine exergy efficiencies and identify and quantify exergy destructions so that directions for improved efficiency can be determined. These aims have been illustrated by the exergy analyses in this chapter of renewable energy systems including solar PV systems, solar ponds, wind turbines and geothermal district heating systems and power plants.

Problems

10.1 How are the energy and exergy efficiencies of solar photovoltaic systems defined?
10.2 Identify the sources of exergy loss in solar photovoltaic systems and propose methods for reducing or minimizing them.
10.3 Explain why solar photovoltaic systems are costly even though they use solar energy, which is free.
10.4 Why are the exergy efficiencies lower than the energy efficiencies for solar photovoltaic systems? Explain.
10.5 Obtain a published article on exergy analysis of solar photovoltaic systems. Using the operating data provided in the article, perform a detailed exergy analysis of the system and compare your results to those in the original article. Also, investigate the effect of varying important operating parameters on the system exergetic performance.
10.6 What is the difference between an ordinary pond or lake and a solar pond? Are solar ponds thermal energy storage systems?
10.7 How are the energy and exergy efficiencies of solar ponds defined?
10.8 Identify the operating parameters that have the greatest effects on the exergy performance of a solar pond.
10.9 Obtain a published article on exergy analysis of solar ponds. Using the operating data provided in the article, perform a detailed exergy analysis of the system and compare your results to those in the original article. Also, investigate the effect of varying important operating parameters on the system exergetic performance.
10.10 Why are exergy efficiencies lower than energy efficiencies for solar ponds?
10.11 Investigate the development of wind turbines in the last three decades. Compare the costs and efficiencies of wind turbines that existed 20 years ago to those currently being installed.
10.12 Do you agree with the statement 'the energy and exergy efficiencies of wind turbines are identical'? Explain.
10.13 What is the value of exergy analysis in assessing and designing wind turbines? What additional information can be obtained using an exergy analysis compared to an energy analysis? How can you use exergy results to improve the efficiency of wind turbines?
10.14 What is the effect of wind-chill temperature on the power generation and efficiency of a wind turbine?
10.15 How are the energy and exergy efficiencies of wind turbines defined? What is the difference between them? Which one do you expect to be greater?
10.16 What is the difference between energy-based and exergy-based spatio-temporal wind maps?
10.17 Which use of a geothermal resource at 150°C is better from an energetic and exergetic point of view: (a) district heating or (b) power generation? Explain. What would your answer be if the geothermal resource is at 90°C?
10.18 How can a geothermal resource at 150°C be used for a cooling application? How can you express the exergy efficiency of such a cooling system?
10.19 How are the energy and exergy efficiencies of geothermal district heating systems defined? Which definition is more valuable to you if you are a customer of geothermal district heat? Which definition is more valuable to you if you are an engineer trying to improve the performance of the district system?
10.20 Identify the main causes of exergy destruction in a geothermal district heating system and propose methods for reducing or minimizing them.
10.21 Geothermal resources can be classified based on the resource temperature or the resource exergy. Which classification is more suitable if geothermal energy is to be used for (a) district heating, (b) cooling and (c) power generation? Explain.
10.22 How do you explain the difference between the energy and exergy efficiencies of the geothermal district heating system considered in this chapter?
10.23 What thermodynamic cycles are used for geothermal power generation? Discuss the suitability of each cycle based on the characteristics of the geothermal resource.
10.24 Define the energy and exergy efficiencies for various geothermal power cycles. How can you express the energy and exergy of a reservoir?
10.25 Compare the energy and exergy efficiencies of a geothermal power plant. Which one is greater?
10.26 Do you support using geothermal resources below 150°C for power generation? If such an application is to occur, what is the most appropriate cycle? Explain.
10.27 Identify the main causes of exergy destruction in geothermal power plants and propose methods for reducing or minimizing them.
10.28 In a geothermal power plant using a 160°C resource, geothermal water is reinjected into the ground at about 90°C. What is the ratio of the exergy of the brine reinjected to the exergy of brine in the reservoir? How can you utilize this brine further before its reinjection?
10.29 What is the effect of ambient air temperature on the exergetic performance of a binary geothermal power plant?

10.30 Is there an optimum heat exchanger pressure that maximizes the power production in a binary geothermal power plant? Conduct an analysis to determine the optimum pressure, if one exists, for the power plant considered in this chapter.

10.31 Obtain a published article on exergy analysis of a geothermal power plant. Using the operating data provided in the article, perform a detailed exergy analysis of the plant and compare your results to those in the original article. Also, investigate the effect of varying important operating parameters on the system exergetic performance.